Development of a Dielectrophoresis-Based Cancer-Cell Analysis Tool

Temple Anne Douglas

Dissertation submitted to the Faculty of the
Virginia Polytechnic Institute and State University
in partial fulfillment of the requirements for the degree of

Doctor of Philosophy
in
Biomedical Engineering

Rafael V. Davalos, Chair
Daniela Cimini
Eva M. Schmelz
Mark A. Stremler
Scott S. Verbridge

August 28, 2018
Blacksburg, Virginia

Keywords: dielectrophoresis, biophysics, metastasis, evolution, cancer, treatment resistance

Development of a Dielectrophoresis-Based Cancer-Cell Analysis Tool

Temple Anne Douglas

(ABSTRACT)

One significant obstacle in cancer treatment is tumor heterogeneity. Different subpopulations within a tumor can respond differently to chemotherapy, resulting in resistance and recurrence. Addressing these differences while choosing a treatment modality could significantly improve chemotherapy outcomes. This work focuses on the development of a new modular device that leverages the unique advantages of a contactless dielectrophoresis, a method that uses applied electric fields in a microfluidic device to separate cells by biophysical phenotype. By optimizing force balancing between the dielectrophoretic force and the drag force on cells in the device, and by using cell-size pillars to maximize electric field gradients per volt applied while reducing cell-cell interactions,we demonstrate that it is possible to separate mouse ovarian surface epithelial (MOSE) cells at different stages while maintaining high viability. We also show other cell types to be separable with this device and develop an algorithm to rapidly analyze cell response to a variety of frequency/voltage/flow rate combinations. We also propose a microfluidic device downstream of the DEP chip that can be used to provide an integrated system for studying the subpopulations separated using dielectrophoresis by moving them into a culture chamber with hydrogel where they can be grown in 3D and characterized for a variety of parameters such as biophysical structure, metastatic capacity, and chemotherapy resistance.

Development of a Dielectrophoresis-Based Cancer-Cell Analysis Tool

Temple Anne Douglas

(GENERAL AUDIENCE ABSTRACT)

Dielectrophoresis is a method by which cells are polarized in response to an electric field gradient. This work optimizes this technique so that it can be used to separate highly similar subpopulations of cancer cells in a microfluidic device. Computer code is also developed to automate data processing. A technique for analyzing these cell subpopulations is also proposed and some feasibility testing performed.

Dedication

To my family.

Acknowledgments

I would like to thank my advisor Dr. Davalos, my committee, and several of my colleagues who worked with me on DEP: Nikita Balani, Jaka Cemazar,Dan Sweeney, Nastaran Alinezhadbalalami, Philip Graybill, Alejandro Rodriguez Pena. I would also like to thank Don Leber at the Virginia Tech Micro and Nano Fabrication lab, and Bob Geil at the UNC cleanroom. I would also like to that Stanca Ciupe for discussing the mathematical model with me.

This work was supported by NIH 5R21 CA173092-01, Isolation and enrichment of tumor stem cells using contactless dielectrophoresis and CIT MF13-037-LS, Use of Electric Fields for the Isolation of Tumor Initiating Cells and Other Rare Cells. I would also like to acknowledge Virginia Biosciences Health Research Corporation (VBHRC). A big thank you to the NSF IGERT DGE-0966125 MultiSTEPS and to the Virginia Tech New Horizons Graduate Scholars program for funding my graduate education.

Contents

List of Abbreviations

ϵ	Permittivity
ϵ^*	Complex permittivity
η	Fluid viscosity
∇	Gradient
ω	Angular frequency
$\Re$	Real Part
σ	Conductivity
$\vec{E}$	Electric field
$\vec{F}_{DEP}$	DEP Force
$\vec{F}_{drag}$	Drag force
$\vec{v}$	Particle velocity vector
i	$\sqrt{-1}$
$K(\omega)$	Clausius Mossotti factor as a function of angular frequency, ω
r	cell or particle radius
3D	Three-dimensional
AC	Alternating current

BSA Bovine serum albumin

cDEP Contactless dielectrophoresis

COMSOL Finite element modeling software

CTC Circulating tumor cell

DEP Dielectrophoresis

DI Deionized

DMEM Dulbecco's Modified Eagle Medium

DNA Deoxyribonucleic acid

EDTA Ethylenediaminetetraacetic acid

EMCCD Electron-multiplying charge-coupled device

EMT Epithelial-to-mesenchymal transition

FACS Flow-activated cell sorting or flow cytometry

iDEP Insulator-based dielectrophoresis

MACS Magnetic-activated cell sorting

MOSE Mouse Ovarian Surface Epithelial Cells

MOSE-L_{TICv} Highly aggressive mouse ovarian surface epithelial cells

MOSE-L Mid stage mouse ovarian surface epithelial cells

nDEP Negative dielectrophoresis

OBS Open broadcasting software

PBS Phosphate Buffered Saline

pDEP Positive dielectrophoresis

PDMS Polydimethylsiloxane

PTFE Polytetrafluoroethylene

RPMI Roswell Park Memorial Institute Medium

SU-8 Photoresist

VLC video processing software

Chapter 1

Introduction

Cancerous tissue is heterogeneous in nature, often containing several subpopulations of cells with varying degrees of aggressiveness and susceptibility to different types of chemotherapy [1, 2]. Currently, cancer treatment tends to treat the bulk of a tumor, leaving behind treatment-resistant or highly malignant cells that then repopulate the space, leading to treatment-resistance and recurrence [3, 4]. Despite numerous studies, the complexity of determining which treatments will be most effective in different scenarios is still unsolved, with some evidence showing that unoptimized application of chemotherapy can even mutate the surviving cells, which increases heterogeneity and in turn leads to more aggressive and metastatic subpopulation emergence [5, 6, 7]. In particular, attempts to treat metastatic cells often fail, leading to death in many cases [8].

This work demonstrates the use of a contactless dielectrophoresis device for separating and characterizing tumor subpopulations. Contactless dielectrophoresis is a method of separating cells using an electric field applied from fluidic electrodes across an insulative membrane into a region with cells. Small insulative posts within the operating region induce small inhomogeneities in the electric field, which lead to localized dielectric forces and cells trapping on posts. Shown here are a set of experiments demonstrating that it is possible to separate highly similar subpopulations of cells within a tumor using dielectrophoresis (DEP). This is demonstrated using mouse ovarian surface epithelial (MOSE) cells, a cell line that [9, 10]

was developed via repeated injections into a mouse model to gradually advance the tumor stage[11]. This research shows that MOSE cells at different stages of malignancy can be separated with DEP, while also retaining high viability [9, 12].

In order to improve the speed at which cell populations can be analyzed, an ImageJ macro was developed to improve image processing and allow moving vs. trapped cells to be counted from a video, where cells trapping at different voltage and frequency pairings were recorded. As a case study, macrophages and fibroblasts were trapped and processed, using this method following separation.

This work also develops the concept for a cell culturing device that can interface with the contactless dielectrophoresis device. This downstream device is envisioned to improve chemotherapy selection by allowing for morphologically unique cells to be tested separately against an array of chemotherapies. Proposed here is an integrated system for personalized tumor diagnostics, in which each subpopulation in a patient's biopsy is separated by their dielectric signature. These subpopulations will then be characterized in a hydrogel aggressiveness assay and tested against a panel of chemotherapies. In the future, upon receiving a tumor biopsy, cells flow through the dielectrophoretic cell separator, are separated by their subtype, and flow into a culture chamber where they can be cultured in 3D as an indicator of metastatic capacity. This could be followed by testing chemotherapy agents against each cell subtype individually. Using this data (for each subtype, growth rate, malignancy and susceptibility to a panel of chemotherapies or other treatments), this information could be paired to this single-chip diagnostic with a computer algorithm that will model optimum treatment regimens based on output data.

This research will also continue using this chip to gather data on the correlation between specific trapping frequencies and regular phenotypic information. It has been observed that lower trapping frequency within a cancerous cell type tends to correlate with metastatic capacity, which we hypothesize is due to changes in the structure of the cell membrane before migration.Current DEP theory does not account for such structural and morphological changes[13], and with a large database of this information, as well as information on treatment resistance and malignancy, this work can address the problem of identifying which cells correlate with specific bioelectrical phenotypes and frequency-dependent states.

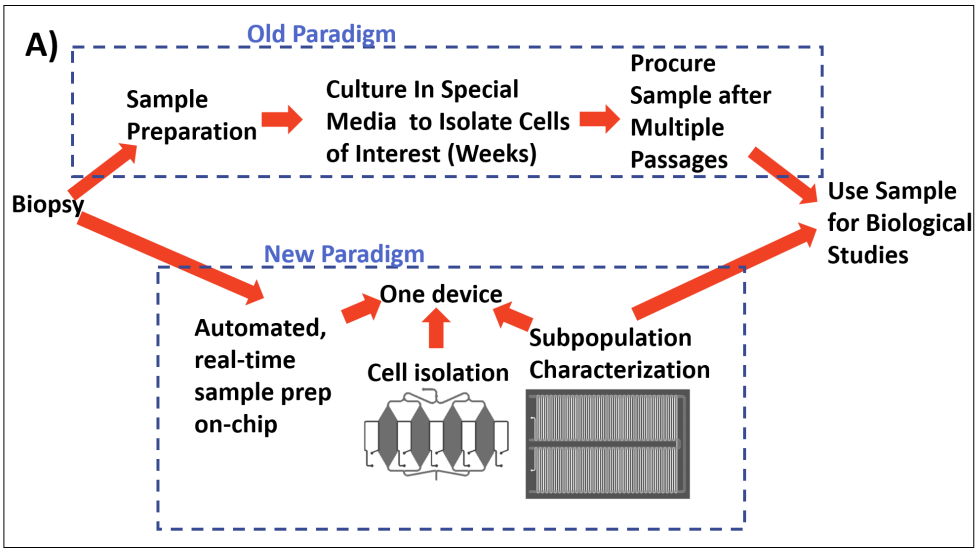

Figure 1.1: Comparing current biopsy analysis processing techniques with an integrated antibody free, single-chip.

Figure 1.1 shows the proposed function of the integrated cDEP device design.

1.0.1 Other Cell Sorting Technologies:FACS and MACS

Several other methods of cell sorting exist, including flow-activated cell sorting (FACS) and magnetic-activated cell sorting (MACS)[14]. FACS uses antibodies to fluorescently tag and

label biomarkers on the cell surface, and then sort based on tag color. This causes irreversible modifications to the cell, and limits diagnostic capacity to known biomarkers, when in fact tumors have a high level of genetic and phenotypic heterogeneity[15]. Although FACS has been used for cancer stem cell study[16], cell viability after FACS falls significantly, with cells experiencing permanent modifications due to antibody tagging, making further live-cell study difficult[15]. MACS works via a similar strategy using antibodies conjugated to magnetic beads [17].

1.1 Hypothesis

We hypothesize that contactless dielectrophoresis could be promising as a clinical device for improving cancer diagnosis and as an intermediate step develop the technology into a device for biological laboratory application. For this, we envision the following platform:
For biological laboratory applications, contactless dielectrophoresis in a microfluidic device can be used for separating a variety of cell populations on-chip. This chip can either stand alone or be coupled with a downstream system for culturing the resultant subpopulations in a 3D matrix for microenvironment study or invasiveness assays. This information can be validated and potentially directed towards a diagnostic device using a system downstream from the contactless dielectrophoresis platform.

Contactless dielectrophoresis produces batches of viable cells[12]. We envision a platform in which these cells run into a chamber where they are removed from their low-conductivity buffer and mixed with a mixture of media and uncured 3D hydrogel. They then run into a chamber where the 3D hydrogel cures. An array of media lines separated from the chip by a small-molecule permeable membrane allows media, a panel of chemotherapies, or any

dissolvable small molecule to be diffused into the chip. Maintaining the cells in hydrogel allows for the chip to be used as a controlled biomimetic environment for studying cell growth in 3D, which allows it to be used as an invasiveness assay[18, 19, 20, 21]. With a panel of overlaid chemotherapy or other treatments, this can be used to create an assay to determine cell aggressiveness and chemotherapy response for a variety of treatments.

Biologically, this assay can also be used for immune studies, microenvironment studies, and a variety of assays based on controlled separate cell populations in a 3D matrix. The use of media and small molecule diffusion across a barrier and into 3D collagen allows cellular response to be studied in a more realistic way, as cells respond differently to stressors when they are in a 3D matrix compared to 2D, and when they are interacting with a gradient of effectors instead of a constant high dosage.

1.2 Dielectrophoresis

Dielectrophoresis (DEP) is the motion of a particle due to its polarization in a non-uniform electric field. Frequently, this technique is used to separate particles in solution. [13, 22, 23, 24]. Microfluidic chips provide an excellent platform for employing dielectrophoresis, as they allow for a controlled flow environment where the DEP force can be finely controlled with respect to other forces on the cell. The small size of the microfluidic device allows for flow to be primarily laminar, allowing for precise control of on-chip mechanisms and force balancing [25]. According to the DEP theory as outlined by Pohl, particles are sorted by their polarizability and electrical properties [13]. In the case of cells, this bioelectrical phenotype can depend on malignancy, size, viability, cell type, nucleus to cytoplasm ratio, organelle structure and distribution, protrusions, proteins, nuclear content and other factors [24, 25, 26, 27, 28, 29, 30, 31].

1.3 Contactless Dielectrophoresis for Cell Separation

A schematic of the chip design is shown in Figure 1.2. Fluidic electrodes on either side of the channel containing 10x phosphate buffered saline (PBS) are used to apply an electric field across the device. Cells flow through the device and are trapped on posts following the applied electric field. Untrapped cells flow out. When the voltage is removed, all the cells trapped on posts flow out of the device, leading to alternating plug flow of trapped and untrapped cell populations.

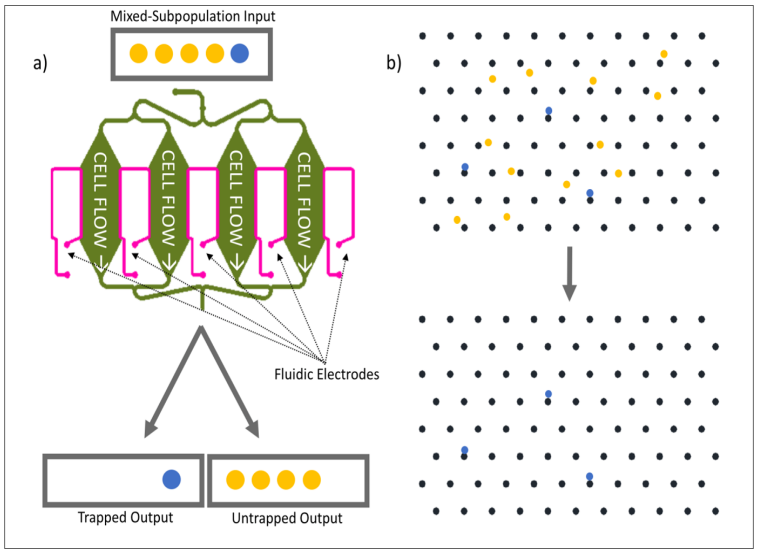

Figure 1.2: Schematic showing chip design.

We showed in an earlier work that by changing from 100μm posts to 20μm posts, it is possible to achieve higher viability of cell populations going through the chip, and better sensitivity to differences between cell populations. Figure 1.3 shows an image of cell trapping in the device form with 20μm posts. Here it is possible to see that on 100 μm posts, cells tend to

clump and chain together. This can be explained by the fact on the top of the post (in the direction of flow), there is a fairly large area where cells can fit. Drag force doesn't really begin to pull the cells off until they round the sides of the posts. This can be remedied by making 20 μm posts, where each post can only hold 1-2 cells. This prevents clumping and ensures each cell is acting with a controlled electric field gradient to minimize variability in the DEP force for a cell a given bioelectric phenotype.

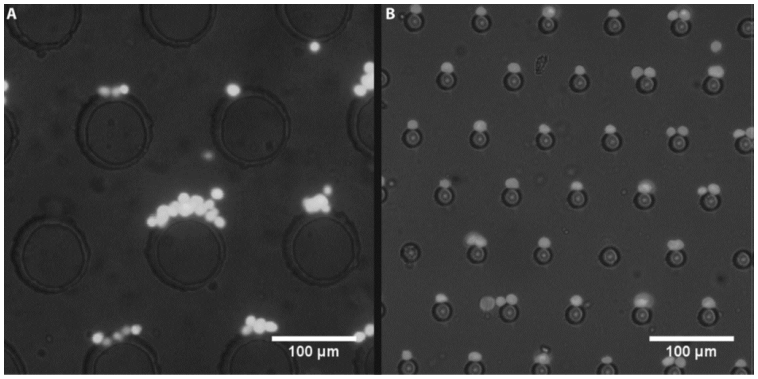

Figure 1.3: A) 100μm posts contribute to cell pearl chaining and clumping, which decreases the sensitivity of trapping by creating large uncontrolled local inhomogeneities in the electric field. B) By using cell-sized posts, drag-DEP force balancing creates a system where 1-2 cell trapping is the norm, and pearl chaining does not occur.

Figure 1.4 shows the viability of mouse ovarian surface epithelial (MOSE) cells going through the 20μm and 100μm post-size devices The initial viability for each cell line (Control in figure) is the viability in the population before sending through the chip. The viability of the untrapped cells going through the chip is always slightly lower than the viability of the trapped cells, even in the 20 μm case. This is because cell that were dead before going through the chip do not respond to the applied electric field, and therefore don't trap. The two columns with 0V represent cell viability after going through the chip with the voltage off, or damage to the cells due to the chip geometry.

From this point, we began work to test the separability of cells with this chip design, which will be discussed in the next chapter. The following chapter showcases the separation of

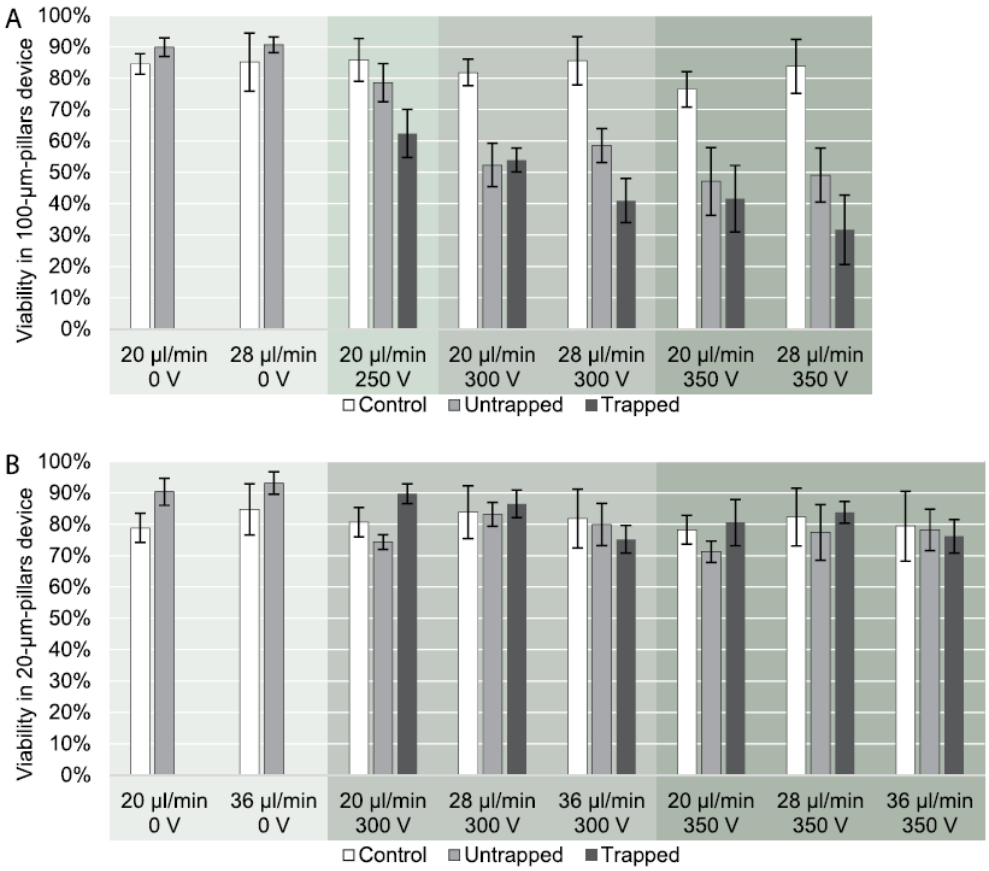

Figure 1.4: A) Viability of cells in the $100\mu m$ pillar chip, and B) Viability of cells in the $20\mu m$ pillar chip.

macrophages and fibroblasts, two cells essential to immune function, and the development of a computer program to automate and speed up analysis of separation, allowing for screening of many different parameter combinations in a single experiment. The chapter after that proposes the development of a novel way of analyzing cell subpopulations downstream from this device, such that each biophysically distinct subpopulation can be evaluated for its growth rate, morphology, and response to small diffusible molecules in vitro downstream from the device. The final chapter discusses next steps for this device.

Chapter 2

Theory and Background: Electrical Methods of Rare Cell Isolation

Temple A. Douglas[a] and Rafael V. Davalos[a]

[a] Virginia Tech - Wake Forest School of Biomedical Engineering and Sciences

Author Contributions The portion of this chapter submitted here was written by TAD with edits from RVD.

This chapter was submitted as a book chapter, for which the citation is:

Wasson E.M., **Douglas T.A.**, Davalos R.V. (2016) *Mechanical and Electrical Principles for Separation of Rare Cells.* In: Lu C., Verbridge S. (eds) Microfluidic Methods for Molecular Biology. Springer.

Dielectrophoresis (DEP) is the motion of a particle due to its polarization in a non-uniform electric field. Using this technique, particles can be separated in solution. Different types of cells in particular, but also DNA, particles and proteins, have been separated via dielectrophoresis based on their intrinsic polarizability [22, 23, 32, 33, 34]. The application of microfluidic chips has been useful in this application, as they have been utilized to design systems with low Reynolds number regimes and high electric field gradients. The high electric field gradients induce a dipole in the cell, dependent on its properties, and can be used to manipulate the cell through a specific balance of fluidic and electric forces [25, 35, 36]. The DEP force that is exerted on a cell depends on certain properties of that cell in an electric field, and can permit users to sort cells and small particles by features such as malignancy, size, viability, cell type and other factors [24, 26, 29, 37, 38]. The application of microfluidic devices for dielectrophoresis allows this technology to be easily and efficiently transferred into low-cost medical devices [24].

2.1 Electrochemical properties of cells

The cellular environment has many different properties that can affect the polarizability of a cell, thus leading to a unique electromechanical behavior that can act as that cell's signature. Cellular properties create an intrinsic polarizability of the cell [22]. When the cell is placed under an electric field, free charges align to create a dipole within the cell[39, 40]. Some properties of the cells that can influence this cellular polarizability are amino acid content, interaction between charged areas of amino acids and the water molecules around the cells, structure and rigidity of the lipid bilayer membrane, as well as other factors [22, 41, 42, 43]. For more information on the biophysics of cells, please see the review by Ronald Pethig and Douglas Kell, "The passive electrical properties of biological systems: their significance in

physiology, biophysics and biotechnology" [41].

2.2 DEP Theory

DEP relies on an important property of cells—-their intrinsic polarizability, which allows them to induce an electric dipole in the presence of an electric field. When this dipole is induced within the cell, a force of attraction or repulsion can form between the cell and another cell, or between the cell and objects in the microfluidic channel. These forces induced by dielectrophoresis have been derived in other publications, such as in the review of dielectrophoretic theory by Ronald Pethig [22]. The dielectrophoretic force is usually written as:

$$\vec{F}_{DEP} = 2\pi\epsilon_m r^3 \Re[K(\omega)](\nabla(\vec{E}\cdot\vec{E})) \tag{2.1}$$

In this equation, ϵ_m is the permittivity of the medium, r is the radius of the particle in the field, K is the Clausius-Mossotti factor and ∇E^2 the gradient of the root mean squared of the electric field. The Clausius-Mossotti factor is a constant throughout the electric field, and is dependent on cell polarizability, medium polarizability, conductivity of the medium and frequency of the electric field. The gradient of the electric field is spatially dependent, and can be determined computationally for complex geometries. The real part of the Clausius-Mossotti factor reduces to [22]:

$$Re[K(\omega)] = Re[(\epsilon_c^* - \epsilon_m^*)/(\epsilon_c^* + 2\epsilon_m^*)] \tag{2.2}$$

In this equation, ϵ_c^* is the complex permittivity of the cell, ϵ_m^* is the complex permittivity of the medium, and the complex permittivity in either case is $\epsilon^* = \epsilon + \sigma/i\omega$, with ω the angular frequency of the electric field being applied, and σ the conductivity of the medium [22].

Different cells with different permittivities will have different values for Clausius-Mossotti factor, leading to a difference in the force each cell feels within the chip at a given frequency and local field gradient. This difference in forces is what permits separation. In a microfluidic chip with laminar flow, the trapping force can either act to attract or repel a cell, or have very little influence on it. If the force on the cell is not great, the cell will not deviate much from its streamline and will continue to flow as if no electric field were applied. In the presence of a dielectric force, the cell may stick to a part of the device or deviate from its normal streamline.

Frequency-dependent curves for the Clausius-Mossotti factor normally have the following shape. The differences between these curves allow for differences in DEP forces felt by cells and variation of the cells pathway as is shown in Figure 8.

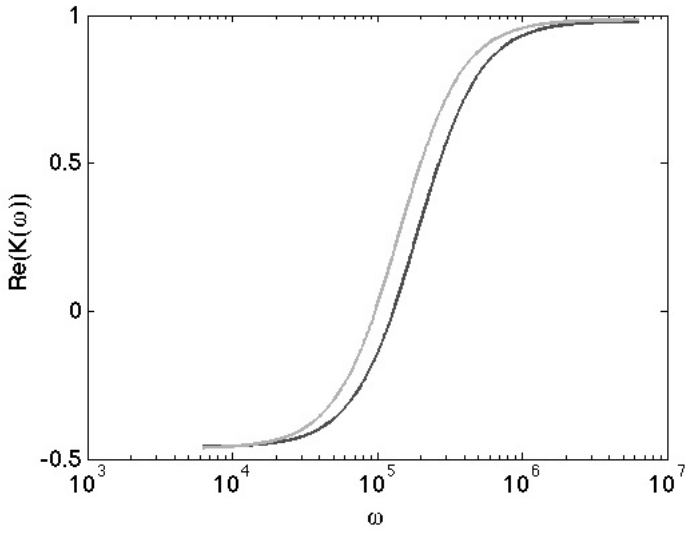

Figure 2.1: Clausius-Mossotti factor plotted for different frequencies using the single-shell model [23].

2.3 Negative vs. positive dielectrophoresis

Depending on the applied frequency and the electrical properties of the cell and the suspending medium, the DEP force can be either negative or positive. Negative dielectrophoresis (nDEP) is when the cell experiences a repelling force from regions of higher electric field gradient. The electrodes within the channel push away any cell with the appropriate polarizability given the frequency and voltage of current applied in the channel. Conversely, positive dielectrophoresis (pDEP) is a system in which the cells are attracted to regions with higher field gradients. While negative dielectrophoresis is good for redirecting flow of cells based on their polarizability, positive dielectrophoresis is good for cell trapping. However, cells can be trapped or redirected with either method, depending on the force balance between the drag on the particle and the dielectrophoresis forces.

In a proof of concept, researchers have designed negative dielectrophoresis traps to immobilize cells on a chip[44]. Another group reported using negative dielectrophoretic design to pattern liver cells on a chip, by repelling cells from certain areas of the chip and causing them to land in designated patterns [45]. Using a quadrupole device, another group was able to determine blood type by localizing the crossover frequency (where negative dielectrophoresis switches from positive dielectrophoresis) for a set of blood cells[46].

The magnitude of the dielectric force is a function of the medium permittivity, the cell permittivity, magnitude of the applied electric field, and the cell radius. The direction of the force exhibited on the cell, however, is a function only of the electric field in the chip and whether positive or negative DEP is being exerted, and thus can be determined independently of cellular properties, creating an effective field of possible cell-chip interactions. An effective

magnitude of force can be developed by normalizing the cell-specific properties, such as the Clausius-Mossotti factor, to the cell-dependent properties. While the magnitude of the force depends on the properties of each individual cell type, the relative magnitude of force in one region versus another is independent of cellular properties. This effective field of DEP forces is very useful in determining chip design and predicting trapping regions. The effective field is:

$$\vec{\Gamma} = \nabla(\vec{E} \cdot \vec{E}) \tag{2.3}$$

For a derivation of this field, please see the paper by MB Sano et al. Multilayer contactless dielectrophoresis: theoretical considerations [47].

2.3.1 Multi-shell model and single-shell model for measuring cell permittivity

For theoretical calculations of cell polarizability, the cell can be approximated as a set of concentric spherical shells as is shown in Figure 9. These shells define the properties of each layer of the cell and the topology of the related regions. For a typical cell, one could estimate the outer membrane as one shell, the cytoplasm as another, and the nuclear envelope as a third. By reducing shells of similar properties into effective shells, it is possible to condense the complex dielectric factor describing the set of concentric rings into its simplified form. Usually the cell can be condensed to a single-shell model, taking an effective permittivity inside of the cell. For more information, see Ronald Pethig's review, Dielectrophoresis: An assessment of its potential to aid the research and practice of drug discovery and delivery [22].

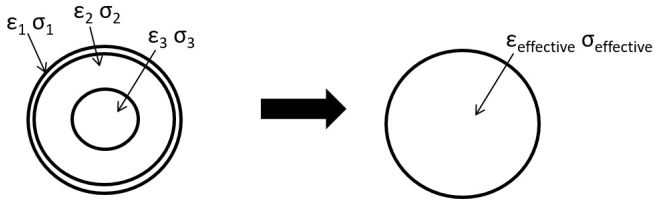

Figure 2.2: Depiction of the multi-shell model.

2.3.2 Derivation of DEP force

The DEP force is derived from the intrinsic polarizability of a cell, which can lead to an induced dipole when it flows through a chip. To derive this DEP force from the properties of a cell, we will first start with a dipole in an electric field as is shown in Figure 10. For more detail and mathematical guidance, please see Chapter 2 of Electromechanics of Particles by Thomas B. Jones, Cambridge University Press[48].

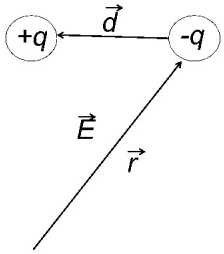

Figure 2.3: Dipole in an electric field, analogous to a cell in an electric field.

The cell is not a perfect dipole, but the induced cellular dipole that forms in the presence of the electric field can be estimated as a dipole with a small distance between the two poles $\vec{d}$. Because the electric field is nonuniform in the chip, due to the presence of obstacles and other cells, we must consider the electric field at each point independently, rather than making an assumption about the form of the field. The force on a dipole is then,

$$\vec{F} = q\vec{E}(\vec{r} + \vec{d}) - q\vec{E}(\vec{r}) \tag{2.4}$$

We will assume that we are measuring from a point $\vec{r}$, far away from the dipole. This allows us say that the distance between the two points in the dipole, $\vec{d}$, is very small in comparison to the distance from which we are measuring. This assumption should be considered valid in a dielectrophoretic chip, as the internal cellular dipole is smaller than the relation between that dipole and other features of the chip. This assumption is made in order to simplify the non-uniform electric field. Otherwise, the electric field would need to be considered separately at $\vec{r}$ and $\vec{d}+\vec{r}$. We can make a Taylor expansion for $\vec{E}(\vec{r}+\vec{d})$. This becomes:

$$\vec{E}(\vec{r}+\vec{d}) = \vec{E}(\vec{r}) + \vec{d}\nabla\vec{E}(\vec{r}) + ... \tag{2.5}$$

Because we assumed that $\vec{d}\vec{r}$ we can neglect higher terms than $\nabla\vec{E(r)}$ as they will be very small. The force on the dipole then can be approximated as:

$$\vec{F_{DEP}} \simeq q\vec{E}(\vec{r}+\vec{d}) - q\vec{E}(\vec{r}) = q\vec{d}\nabla\vec{E}(\vec{r}) \tag{2.6}$$

This is known as the dielectrophoretic approximation. By definition, the dipole moment, $\vec{p}$, is $\vec{p} = q\vec{d}$. Therefore,

$$\vec{F_{DEP}} = \vec{p}\nabla\vec{E}(\vec{r}) \tag{2.7}$$

gives the dielectrophoretic force in a chip [48].

2.4 Derivation of the Clausius-Mossotti factor

This derivation also comes from Electromechanics of Particles by Thomas B. Jones[48]. Please refer to the book for further information. Going back to the model that we have a small dipole in the cell, the potential for these two interacting point charges is given by ϕ:

$$\phi = q/(4\pi\epsilon_1 r_+) - q/(4\pi\epsilon_1 r_-) = q/(4\pi\epsilon_1)(1/r_+ - 1/r_-) \tag{2.8}$$

This considers that the point charges are separated by a distance $2r$. In this case, the permittivity constant, ϵ_1 is the permittivity of the medium, as we are considering these point charges to be in the medium of the device. See Electromechanics of Particles for more details. This equation for electric potential can be rewritten as a Maclaurin expansion:

$$\phi = (qdP_1(cos\theta))/(4]\pi\epsilon_1 r^2) + ... \tag{2.9}$$

In this expansion, $P_1(cos\theta)$ is the first order Legendre polynomial, which is $P_1(cos\theta) = cos\theta$. Taking the first term of the Maclaurin expansion gives the first order approximation for the potential between two point charges (in this case, the cellular dipole).

$$\phi \simeq qdcos\theta/(4\pi\epsilon_1 r^2) \tag{2.10}$$

As before, we know the dipole moment to be p=qd, which gives:

$$\phi \simeq pcos\theta/(4\pi\epsilon_1 r^2) \tag{2.11}$$

Again, here ϵ_1 would be the permittivity of the medium around the two point charges. We will keep this equation until a bit later. Now, we consider an insulating sphere of radius R in a uniform electric field as is shown in Figure 11. This can also be used to describe a particle in a medium, as the cell is not particularly conductive. Because the cell is much smaller than the chip, we make the assumption that the electric field will be mostly uniform when passing through the cell. The permittivity of the medium is taken to be ϵ_1, and the

permittivity of the cytoplasm is ϵ_2.

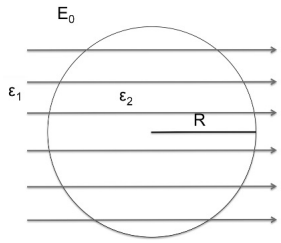

Figure 2.4: Insulating sphere in uniform electric field.

Using Gauss's law, we find the potential inside and outside the sphere. This gives:

$$\phi_1 = -E_0 r cos\theta + (Acos\theta)/r^2 \tag{2.12}$$

outside the sphere.

$$\phi_2 = -Br cos\theta \tag{2.13}$$

inside the sphere.

The electric field is continuous at the boundary. The norm of the displacement flux is also continuous at the boundary. Therefore, we must consider the boundary conditions (at r=R) to be:

$$\phi_1 = \phi_2 \tag{2.14}$$

$$-\epsilon_1 \frac{\partial \phi_1}{\partial r}|_R = -\epsilon_2 \frac{\partial \phi_2}{\partial r}|_R \tag{2.15}$$

Solving for these two equations given the boundary conditions leaves us with a system of equations that can be solved to get A and B. In this case, we find:

$$A = R^3(E_0 - B) = R^3 E_0(\epsilon_2 - \epsilon_1)/(\epsilon_2 + 2\epsilon_1) \tag{2.16}$$

$$B = (3\epsilon_1 E_0)/(\epsilon_2 + 2\epsilon_1) \tag{2.17}$$

If we plug these back into the equations for ϕ_1, ϕ_2, we get:

$$\phi_1 = -E_0 r cos\theta + R^3/r^2 E_0(\epsilon_2 - \epsilon_1)/(\epsilon_2 + 2\epsilon_1)cos\theta \tag{2.18}$$

outside the sphere.

$$\phi_2 = (-3\epsilon_1)/(\epsilon_2 + 2\epsilon_1)E_0 r cos\theta \tag{2.19}$$

inside the sphere.

Outside the sphere, we have ϕ_1, but we also have the equation for two point charges that we derived earlier, $\phi \simeq (pcos\theta)/(4\pi\epsilon_1 r^2)$. We can set the $1/r^2$ terms equal to each other, as the linear term is referring to the uniform electric field rather than the induced dipole. Doing so, we have:

$$(pcos\theta)/(4\pi\epsilon_1 r^2) = R^3/r^2 E_0(\epsilon_2 - \epsilon_1)/(\epsilon_2 + 2\epsilon_1)cos\theta \tag{2.20}$$

We know that for a homogeneous dielectric sphere, $p = 4\pi\epsilon_1 k R^3 E_0$ (see Electromechanics of Particles, Chapter 2 for details) [48]. Plugging this in gives,

$$k = (\epsilon_2 - \epsilon_1)/(\epsilon_2 + 2\epsilon_1) \tag{2.21}$$

This k is the Clausius-Mossotti factor for the dielectric sphere in a medium.

2.5 Design of cell separation devices

There have been many studies to show the use of dielectrophoresis to separate cells in microfluidic channels. Remembering the DEP force, $\vec{F} = 2\pi\epsilon_m R^3 K(\omega)\nabla\vec{E}^2)$, we see that in

order to have any force between the cell and an object in the channel it is necessary to have a gradient of the electric field. Cell separation can be done based on differences in cell radius and differences in Clausius-Mossotti factor between cells. The Clausius-Mossotti factor, $K(\omega) = (\epsilon_c^* - \epsilon_m^*)/(\epsilon_c^* + 2\epsilon_m^*)$, with $\epsilon^* = \epsilon + \sigma/i\omega$, is dependent on the permittivity of the medium, the conductivity of the medium and angular frequency of the electric field, which is the same for all cells in a device, and the permittivity of the cell, which can vary from one cell type to another. For this reason, factors such the strength of the electric field, frequency of applied voltage, permittivity of the medium and conductivity of the medium can all be modified to amplify the ratio of forces between two types of cells in suspension. However, as can be seen in Figure 2.4, whether or not these two particles can be separated is dependent on the permittivity, conductivity and radius of each cell type as well as the sensitivity of the device design.

Normally, a channel containing a design of electrodes and objects is fabricated, and cells are streamed through the channel at a constant rate. Objects in the channels create inhomogeneities in the electric field, which provide regions that can interact with the cells and elicit a force that will cause them to move according to their dielectric properties. Several of these types of dielectrophoretic mechanisms will be discussed here, including contactless dielectrophoresis, insulator based dielectrophoresis, and variations on these. Many different methods have been used to harness the polarizability of cells and other small molecules for separation, and this list is a small set of what has been done in this field.

2.6 Classical vs. contactless dielectrophoresis

Another method of defining dielectrophoresis is by normal or contactless dielectrophoresis (cDEP). Classical dielectrophoresis requires an electrode to be in direct contact with the medium where the cells are, in order to effect the electric field and create a gradient/inhomogeneity for the dielectrophoresis force to be felt. Contactless dielectrophoresis requires the features in the chip to create inhomogeneities in the electric field, allowing the DEP force to be effected far from the electrodes and preventing cell contact with the electrode. This method improves cell viability by preventing direct contact with high voltage sources [26, 47, 49, 50, 51].

2.6.1 Insulator based dielectrophoresis

Insulator based dielectrophoresis (iDEP) has been widely used in a number of applications for cell separation. This method allows cells to be separated, but uses insulating structures within the chip to create inhomogeneities in the electric field needed to drive DEP. This technique has been employed as a method of trapping protein as well as DNA [52], as well as a method of separating membrane protein nanocrystals from solution [29].

2.7 Conclusion

This chapter outlined the theory and practical implementation of methods of rare cell isolation using microfluidic and bioelectrical methodologies. The ability to capture and isolate rare cells is an important step in the process of being able to diagnose and treat cancer based on the presence of circulating tumor cells and other rare cells of interest to provide early and personalized diagnosis. The development of microfluidics and bioelectrical mechanics

in recent years has provided a novel toolbox that can be utilized to improve our ability to obtain study and utilize these cells to improve patient outcomes.

Chapter 3

A Feasibility Study for Enrichment of Highly Aggressive Cancer Subpopulations by their Biophysical Properties via Dielectrophoresis Enhanced with Synergistic Fluid Flow

Temple A. Douglas[a], Jaka Cemazar[a], Nikita Balani[a], Daniel C. Sweeney[a], Eva M. Schmelz[b] and Rafael V. Davalos[a]

[a] Virginia Tech - Wake Forest School of Biomedical Engineering and Sciences [b] Virginia Tech Department of Human Nutrition, Food and Exercise

Author Contributions TAD, JC, NB performed experiments using DEP. DCS provided the nucleus to cytoplasm ratio data. EMS provided cells. The paper was written by TAD with input from JC, NB, DCS, EMS, RVD.

Citation:

T. A. Douglas, J. Cemazar, N. Balani, D. C. Sweeney, E. M. Schmelz and R. V Davalos, Electrophoresis, 2017, 38, 1507–1514.

A common problem with cancer treatment is the development of treatment resistance and tumor recurrence that result from treatments that kill most tumor cells yet leave behind aggressive cells to repopulate. Presented here is a microfluidic device that can be used to isolate tumor subpopulations to optimize treatment selection. Dielectrophoresis (DEP) is a phenomenon where particles are polarized by an electric field and move along the electric field gradient. Different cell subpopulations have different DEP responses depending on their bioelectrical phenotype, which, we hypothesize, correlate with aggressiveness. We have designed a microfluidic device in which a region containing posts locally distorts the electric field created by an AC voltage and forces cells toward the posts through DEP. This force is balanced with a simultaneous drag force from fluid motion that pulls cells away from the posts. We have shown that by adjusting the drag force, cells with aggressive phenotypes are influenced more by the DEP force and trap on posts while others flow through the chip unaffected. Utilizing single-cell trapping via cell-sized posts coupled with a drag-DEP force balance, we show that separation of similar cell subpopulations may be achieved, a result that was previously impossible with DEP alone. Separated sub- populations maintain high viability downstream, and remain in a native state, without fluorescent labeling. These cells can then be cultured to help select a therapy that kills aggressive subpopulations equally or better than the bulk of the tumor, mitigating resistance and recurrence.

3.1 Introduction

Within a tumor, there is a high degree of cellular heterogeneity due to the presence of spatially and temporally variable stressors, such as microenvironmental gradients, nutrient and oxygen concentration, and intrinsic genomic instability of the cancer cells[2, 53, 54, 55, 56]. As conventional cancer treatments are chosen to treat the bulk of the tumor, there exists

a high probability that genetically variant subpopulations of cells will then resist a given treatment, and repopulate the tumor microenvironment following the death of nonresistant cells[55, 57, 58, 59, 60]. This has been shown to correlate with a diminished efficacy of treatment over time and is responsible for a large percentage of instances of chemotherapy failure [57, 61, 62]. We propose a cell separating microfluidic device capable of enriching for cell types based on the intrinsic bioelectrical and biophysical properties of the cells, which we hypothesize can be eventually used to differentiate cancer cell subpopulations based on their metastatic potential. Such a device would be instrumental in developing a rapid, novel assay to provide diagnostics for personalized treatment optimization utilizing a technique called contactless dielectrophoresis (cDEP) for selective concentration for batch separation. Our device utilizes shear flow coupled with cDEP to polarize and then trap cells on a post array for batch separation. We believe that the shear flow changes the polarizability of the cell populations and thereby when optimized, enhances the separability. This device could be used to provide diagnostic information for personalized treatment optimization. Separation of cell subpopulations from a patient tumor and subsequent selection of a chemotherapy treatment based on the composition and the degree of malignancy or metastatic potential could help direct treatment decisions and reduce instances of tumor recurrence and drug resistance, as well as prevent the development of more malignant tumors in response to chemotherapy. One current method of cell separation for this purpose is fluorescence-activated cell sorting (FACS). However, FACS relies on biomarker labeling on the cell surface, which both irreversibly modifies the cell, and limits the detection capacity to known biomarkers [15, 63]. Cells with an aggressive phenotype that lack common markers would not be detected using this method, and further downstream analysis and culture of primary cell populations would not be possible due to permanent modifications from labeling. Using our microfluidic device, cells can be separated based on their bioelectrical phenotype, which may correlate with metastatic potential of the cells. Changes in the physical structure of the outer surface

membrane, the presence of membrane protrusions, nuclear to cytoplasm ratio, DNA content, and other factors may contribute to this separation. Surface labeling of cells is not necessary when using our device due to the design of insulating structures in the device. The electric field gradient is enhanced relative to the net electric field and high cellular viability is maintained [12]. Cell subpopulations can then be cultured downstream and tested against different treatments to ensure that the most aggressive cells will be effectively killed while minimizing the survival of treatment-resistant populations. In the future, clinicians could use this method to help select and optimize treatments on a case-by-case basis.

In DEP, cells become polarized in the presence of an electric field and experience a translational force parallel or anti-parallel to the electric field gradient depending on their intrinsic properties. We hypothesized that biophysical properties such as the fluidity of the membrane, presence of different transmembrane proteins, cell size, and nuclear size all influence the electrical polarizability of a given cell and dynamic response to an electric field [22, 41, 42, 43]. Unlike traditional DEP, cDEP does not require the electrodes to be in direct contact with the cell suspension, but rather uses fluidic electrodes containing an electrolyte solution separated from the main cell-flow channel by a thin membrane. Separating the electrodes from the fluid in the device eliminates electrolysis and improves cell viability by preventing cell-to-electrode contact [64]. Analogous to insulator-based DEP (iDEP), insulating posts within the channel create gradients in the electric field that drive the DEP force [65, 66, 67, 68].

In our case (Fig. 3.1), the cell-scale dimension of the posts allows for only single cells to trap and eliminates pearl chaining and clumping, phenomena that decrease trapping specificity [12, 26, 26]. We have demonstrated that by combining DEP with shear-flow in a microfluidic chip, it is possible to add an additional parameter to tune cell separation, potentially due to

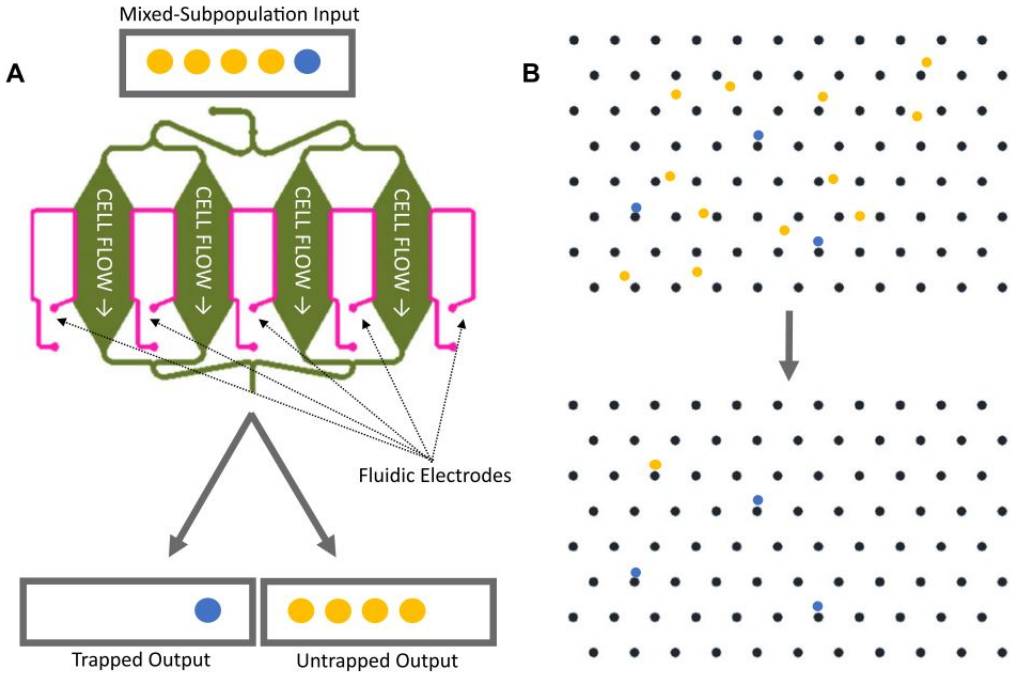

Figure 3.1: Schematic of microfluidic device and cells flowing through device. A mixed population of fluorescently labeled cells flow through the chip. While the voltage is on, some cells trap and others flow through. When the voltage is turned off and cells are released, trapped cells flow through resulting in two subpopulation outputs. (A) Full schematic of chip and function. (B) Post structure inside chip: cells flow through and some cells trap. When DEP buffer is sent through the chip, untrapped cells flow through, leaving only the trapped population.

shear-dependent changes in cellular polarizability. To the best of our knowledge this is the first time anyone has demonstrated that shear flow coupled with DEP can add a layer of sensitivity that had been previously unachievable. This could be exploited in the future and may have potential for other applications. Our polydimethylsiloxane (PDMS) chip consists of a main channel through which cells flow that contains an array of insulative posts, each with a diameter of 20 μm, as shown in Fig. 3.1. Fluidic electrodes on either side of the channel are separated from the cell channel by a 13 μm membrane and are used to apply a voltage across the chip, which causes an electric field to be established in the channel with the cells. Differences in electrical properties between the insulative posts and the buffer

solution create inhomogeneities in the electric field that drive the cells to the posts, provided the applied voltage and frequency create a dielectrophoretic force that overcomes drag on the cells flowing through the device, thus trapping the cells on posts [61]. Untrapped cells continue to flow through the device and are collected at the outlet. Turning off the voltage allows the trapped cells to flow out and be collected in a separate output population.

3.2 Theory

In our cDEP device, drag forces on cells flowing through the microfluidic chip are balanced with the DEP force, $\vec{F}_{DEP}$, in order to accomplish cell sorting [13, 69]. The DEP force is described by:

$$\vec{F_{DEP}} = 2\pi\epsilon_m r^3 Re[K(\omega)]\nabla|\vec{E}\cdot\vec{E}| \tag{3.1}$$

In this equation, ϵ_m is the permittivity of the medium, r is the radius of the cell, $K(\omega)$ is the Clausius–Mossotti factor that depends on the angular frequency of the applied current, ω,and $\vec{E}$ is the electric field. Different subpopulations can have differences both in the radius and in $K(\omega)$, which is defined as:

$$K(\omega) = \frac{\epsilon_c^* - \epsilon_m^*}{\epsilon_c^* + 2\epsilon_m^*} \tag{3.2}$$

The complex permittivities of the cell and of the medium are ϵ_c^* and ϵ_m^*, respectively, where $\epsilon^* = \epsilon + \sigma/i\omega$, where ϵ is the permittivity and σ is the conductivity [13]. $\vec{F_{DEP}}$ is balanced with the drag force on the particle in the fluid. For a spherical particle in a laminar flow regime, the Stokes drag force is:

$$\vec{F_{drag}} = 6\pi\eta r\vec{v} \tag{3.3}$$

In this equation, η is the fluid viscosity, r is the radius of the particle, and $\vec{v}$ is the velocity vector for the particle relative to the fluid.

3.3 Materials and Methods

These experiments aimed to evaluate the cDEP chip design with $20\mu m$ posts for its ability to separate out highly similar tumor cells as a model for a potential diagnostic technique. The mouse ovarian surface epithelial (MOSE) cell line was chosen as a model of a heterogeneous tumor as it is a transitional cell model with different stages of malignancy, making it ideal for subpopulation studies. From the MOSE cell line, two sub-cell lines of high genotypic similarity, $MOSE - L_{TICv}$ (highly malignant, fast developing disease) and MOSE-L (slow developing disease), were used. Each cell line was labeled with red or green calcein in a concentration of 1.7 $\mu g/mL$ and 5 $\mu g/mL$, respectively, and was suspended in low conductivity DEP buffer and the subpopulations were mixed together 1:4 $MOSE - L_{TICv}$: MOSE-L. Optimal frequencies and voltages were found prior to conducting these experiments. Experiments were conducted from 20–40 kHz, with voltages ranging from 300–350 V_{rms} and flow rates from 12–36 $\mu L/min$. Using this data, it was observed that the best separation of cell lines occurred at 350 V_{rms} and 30 kHz [12]. Experiments were then conducted by changing the flow rate of the cells through the device while maintaining the found optimum frequency and voltage. Twenty-seven total trials were run at 20, 24, 28, 32, and 36 $\mu L/min$ to achieve the results shown. In each trial, 50 μl of cell suspension mixture (with less than 1 million cells/mL) was flown through the chip at different flow rates while an optimal frequency and voltage, determined by previous experiments, was applied across the chip [12]. The selected frequency of 30 kHz, close to the crossover frequency of the Clausius–Mossotti factor for each cell type, was chosen as differences between trapping efficiencies were found

to be maximized at this point [9]. A voltage of 350 V_{rms} was chosen to maintain high cell viability in the output population while maximizing trapping. Cells that passed through without trapping were collected in a vial at the output. Fifty microliters of DEP buffer was sent through the chip at the same flow rate as before to wash any untrapped cells out of the device. The voltage was then turned off and trapped cells were released and washed out of the device with 50 μL of low conductivity buffer and collected in another vial, as is shown in Fig. 3.1. Hemocytometry on calcein red and green labeled cells was performed to count the number of MOSE-L_{TICv} and MOSE-L cells in the trapped and untrapped populations.

3.3.1 Chip Preparation

To make the three-layer chip, channel, and electrode layers were fabricated independently using Dow Corning Sylgard 184 PDMS with 10:1 ratio of base to crosslinker. Due to the fine resolution in the channel layer, the mold was fabricated using deep reactive-ion etching (Bob Geil, University of North Carolina) whereas the electrode layer was fabricated using SU-8 photolithography. The thin membrane between the two layers was fabricated using a 5:1 ratio of base to cross-linker that was spun onto a silanized silicon wafer for 15s at 500 rpm and 45s at 4000 rpm. The membrane layer was bound to the channel and electrode layers by plasma exposure for 45s. This set was bound to a glass slide and placed in a vacuum chamber until the time of the experiment. For additional details, refer to Cemazar *et al.*[12].

3.3.2 Cell culture

In this study, we utilized cells derived from normal MOSE cells. Via in vitro passaging, these cells acquired an increasingly aggressive phenotype and genotype and represent a progres-

sive cancer cell line with different stages of the same ovarian tumor [11, 26]. Late-passage (MOSE-L) represent slow growing disease (cause lethal disease in approximately 100 days after intraperitoneal (ip) injection of 1×10^6 cells) [11].

The highly aggressive $MOSE-L_{TICv}$ was generated by injection of MOSE-L cells into syngeneic C57BL6 mice and harvesting of cancer cells from the ascites; these cells represent fast developing disease ($1x10^4$ cells cause lethal disease in 21 days) [70, 71]. We found that between MOSE-L and late stage highly aggressive $MOSE-L_{TICv}$ cells, separability was optimized at a frequency of 30 kHz. A voltage of 350 V_{rms} was applied to create a sufficiently strong electric field gradient to elicit trapping behavior.

3.3.3 Cell Preparation

We added 1.7 $\mu g/mL$ calcein red or 5 $\mu g/mL$ green dye (Life Technologies) to MOSE media (High-glucose DMEM (Gibco) with 3.4 g/L added sodium bicarbonate, 1% penicillin/streptavidin, and 4% fetal bovine serum) and added this to MOSE cells (MOSE-L or $MOSE-L_{TICv}$, was labeled with red and the other with green calcein) in flasks and placed them in the incubator at 37° for 15 min. After dye incubation, we washed the flasks twice with phosphate buffered saline (PBS) and trypsinized cells for 3 minutes. After trypsinization, MOSE media was added to neutralize the trypsin and this suspension was pipetted into 15 mL Falcon tubes. DEP buffer (8.5% sucrose [w/v], 0.3% glucose [w/v], 0.725% RPMI [v/v]) modified with 0.1% of BSA [w/v] and 0.1% of Kolliphor P188 [w/v], and 0.1 mM EDTA was added to the Falcon tubes until a volume of 10 mL was reached. These were centrifuged at 120 g for 5 min to sediment the cells out of the suspension. The DEP buffer and media was removed and 10 mL more DEP buffer was added to the cell pellet. Two

more centrifugations and DEP changes were performed. After all centrifugations, cells were suspended in 1 mL of DEP buffer without BSA/Kolliphor P118/EDTA and were pipetted through a 40 μm cell strainer to remove any cell clumps. Hemocytometry was performed and cells were suspended in more DEP buffer to 10^6 cells/mL. The two cell populations were mixed 1:4 $MOSE - L_{TICv}$ to MOSE-L and the conductivity of the cell mixture was measured. Conductivities between 110 and 120 $\mu S/cm$ were used.

3.3.4 Chip preparation

A chip was removed from under vacuum and ethanol was pumped through the channel layer to prime it and to prevent bubble formation. 10x PBS was put into the electrode layer channels to act as a liquid electrode. 200 μL pipette tips were placed in the electrode channel outlets and filled with 10x PBS as well. A syringe full of DEP buffer was attached to one of the inlet holes via 30-gauge tubing and DEP buffer was run through the chip to remove the ethanol. A syringe full of the cell mixture was attached to the other inlet with 30-gauge tubing. Each of the syringes was placed on a syringe pump to control speed of pumping through the device. Output liquid was sent through 30-gauge tubing and collected in a 0.75 mL microcentrifuge tube.

3.3.5 cDEP setup

A waveform generator (Agilent 33500B Series) was used to send a sinusoidal wave to a high voltage amplifier (Trek Model 2205) where it was amplified to the desired voltage to be sent to the chip. An oscilloscope (Tektronix DPO 2012 Digital Phosphor Oscilloscope) was used to monitor the voltage. Two syringe pumps (Harvard Apparatus Pump 11 Elite and Harvard Apparatus PhD Ultra) were used to pump DEP buffer and medium into the chips.

The Pump 11 Elite pump has a handheld unit that was positioned on a ring stand at an angle above the chip to ensure cells enter the chip uniformly.

3.3.6 cDEP experiments

Before the experiment, 50 μL of the cell mixture was pumped through the device at the target flow rate with no applied voltage and cells were collected at the outlet to be the control population for the experiment. During the cDEP experiment, cells were pumped through the chip at the assigned flow rate, voltage, and frequency up to the target volume of 50 μL. Some cells flowed through the device and into a microcentrifuge tube while others remained in the chip trapped on posts. While leaving the voltage on, 50 μL of the DEP buffer was flown through the chip to wash out any untrapped cells. Then, the microcentrifuge tube at the outlet was changed, the voltage was turned off and 50 μL of DEP buffer was flown through to wash out the trapped cells. After a run was completed, the cells in the syringe were pumped out and reloaded to prevent settling between runs.

3.3.7 Imaging

Per run, two microcentrifuge tubes containing the trapped and untrapped populations were obtained. Ten microliters of each output population was pipetted onto a hemocytometer and imaged with fluorescent microscopy. The number of red calcein and number of green calcein cells in each output population was counted and compared to the original control population.

3.3.8 Analysis

Cells were counted both manually using the ImageJ multi- point tool, and automatically using Analyze Particles.

3.3.9 Normalization

In order to normalize by the initial population to account for experimental error in mixing cells together, the fraction of $MOSE - L_{TICv}$ in the trapped population ($X_{trapped}$) and untrapped populations ($X_{untrapped}$) was divided by the fraction of $MOSE - L_{TICv}$ in the initial population ($X_{initial}$):

$$\tilde{X_{trapped}} = \frac{X_{trapped}}{X_{initial}} \tag{3.4}$$

$$\tilde{X_{untrapped}} = \frac{X_{untrapped}}{X_{initial}} \tag{3.5}$$

In these quantities, a value of $\tilde{X_{trapped}} = 1$ or $\tilde{X_{untrapped}} = 1$ indicates no change in proportion of $MOSE - L_{TICv}$ cells between the sorted and unsorted populations. A value of 2 would indicate that the sorted population had doubled its amount of $MOSE - L_{TICv}$ cells when compared with the initial population. Propagation of error equations were utilized to find the normalized standard deviations ($\tilde{\sigma_X}$):

$$\sigma_{\tilde{Xtrapped}} = \tilde{X_{trapped}} \sqrt{\left(\frac{\sigma_{Xtrapped}}{X_{trapped}}\right)^2 + \left(\frac{\sigma_{Xinitial}}{X_{initial}}\right)^2} \tag{3.6}$$

$$\sigma_{X\tilde{untrapped}} = \tilde{X_{untrapped}} \sqrt{\left(\frac{\sigma_{Xuntrapped}}{X_{untrapped}}\right)^2 + \left(\frac{\sigma_{Xinitial}}{X_{initial}}\right)^2} \tag{3.7}$$

3.3.10 Measurement of nucleus to cytoplasm ratio

Cell and nucleus size measurements were obtained through fluorescence microscopy using MOSE cells stained with Calcein AM to resolve the cytoplasm and NucBlue to resolve the nucleus. Staining was performed using a solution of 1 μL of Calcein AM stock (Life Technologies, Eugene, Oregon, USA) and two drops of NucBlue (Life Technologies) added to the T-25 flasks for every 1 mL of growth medium. Cells were incubated at 37°C and 5% CO_2 for 45 min to allow the vital stains to enter the cells. Following staining, cells were trypsinized, spun at 125 g for 6 min, and resuspended in low-conductivity DEP buffer as described above. Twenty microliters of the cell suspension was then transferred to a glass slide and a cover slip was wet-mounted on top of the cell sample. Brightfield images were obtained through a 63x/0.70 dry objective while fluorescence images were obtained by exciting the labeled the calcein stain and excited at 350 ± 25 nm and read at cells using 470 ± 20 nm and reading at 525 ± 25 nm for 460 ± 25 nm for the NucBlue stain. Imaging was performed using a Leica DMI6000B inverted fluorescence microscope (Leica Microsystems, Bannockburn, IL, USA) equipped with a Hamamatsu C9100-02 EMCCD camera (Hamamatsu Photonics, Shizuoka Pref., Japan). The nucleus and cell radius were measured using a purpose-written ImageJ plugin that identifies high-fluorescence intensity regions of the Calcein AM stained cells in the green channel to identify the cell boundary, then searches the blue channel for a NucBlue- stained region with high-fluorescence intensity contained within the identified cell boundary. This interior boundary was identified as the nucleus. The cell and nuclear radii were determined as the square root of the product of the major and minor radii for each the nucleus and the cell and the nucleus-to-cytoplasm ratio was taken to be the cubed ratio of nuclear radius to the cell radius.

3.4 Results and Discussion

The percentage $MOSE-L_{TICv}$ (highly malignant) cells as a proportion of total cell count for each of the populations is shown in Fig 3.2. Interestingly, we found that as the flow rate was optimized, the trapping ratio between the two subpopulations was increased. This increased sensitivity of the device could allow for separation of highly similar cells by increasing the drag force on the cells to a comparable magnitude to that of the DEP force. At higher flow rates, the magnitude of the drag force in proportion to the DEP force increases, and could contribute to the enhanced force balancing that is seen in the chip. The cellular polarizability could have a shear- dependent component as well. The $MOSE - L_{TICv}$ cells trapped at a higher rate than the MOSE-L cells. At 32 $\mu L/min$, the trapped population contained 41% $MOSE - L_{TICv}$ compared to 23% $MOSE - L_{TICv}$ in the untrapped population. The increase in trapping efficiency leveled between 32 and 36 $\mu L/min$, indicating an optimal flow rate to maximize separability. This indicates that our device is able to detect fine differences between cells based on bioelectrical phenotype. Several factors can contribute to this difference in trapping efficiency at the given frequency, including cell polarizability, radius, trans- membrane proteins, lipid bilayer structure and rigidity and cytoplasm content[72].

Changing the applied frequency is one way to enhance separation between two populations, but frequency-dependent enhancement is not possible beyond a finite optimal frequency range. However, changing the flow rate of the cells and media through the device modifies the drag force on trapped and untrapped cells and can tip the force balance to prevent cells experiencing a weak DEP force from trapping. For cells of radius r at a given point in the microfluidic chip with a defined electric field gradient (for example, in front of a post), the force on that cell is proportional to $Re(K(\omega))$. Comparing a highly polarizable cell with a less polarizable cell of equal radius at a given location and given $\nabla(\vec{E} \cdot \vec{E})$, the force on the

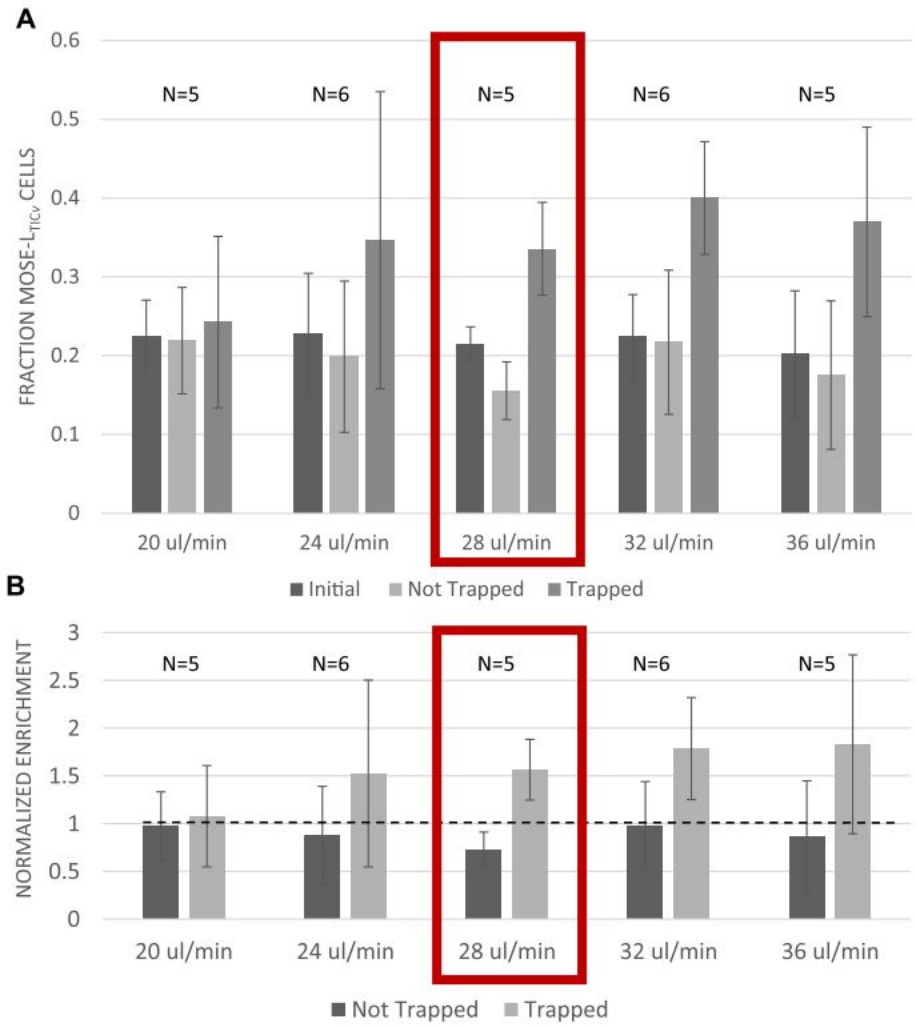

Figure 3.2: (A) Percentage of highly malignant MOSE-L_{TICv} cells in the output populations compared to the initial and untrapped populations at 350 Vrms, 30 kHz applied voltage and different flow rates. N shows the number of trials at each flow rate. (B) Separation data normalized by the initial population, to show percentage enhancement for each population.

highly polarizable cell is greater than the force on the less polarizable cell. If the velocity of the medium relative to the cell is such that the drag force is increased, it is possible to find an optimal flow rate at which the more polarizable cells become trapped while less polarizable cells cannot maintain their location on the posts and fall off. We used fluorescence microscopy to observe static cell suspensions in DEP buffer and found that the $MOSE - L_{TICv}$ cells and MOSE-L cells statistically differ in both their nucleus-to-cytoplasm ratio (NCR) as well as in their radius, as is shown in Fig. 3.3. The cell radius for the $MOSE - L_{TICv}$ cells is larger on average than that for the MOSE-L cells. In addition, the MOSE-L cells appear to have subpopulations within the in vitro culture with smaller radii. The $MOSE - L_{TICv}$ cells appear to have a small subpopulation that has an average radius larger than the rest of the population. These subpopulations within the transitional cell lines could be indicative of further divergent evolutionary pathways due to the in vivo allografted culture environment. Plotting the NCR ratio against cell radius parameter space in Fig. 3.3, we see that the two cell types occupy very different regions that could also indicate varied differences in bioelectrical phenotype, related to the observed differences in trapping. Additional NCR data on earlier stages of this cell line is found in Supporting Information Fig. 3.1. However, differences in nucleus to cytoplasm ratio do not significantly contribute to differences in the Clausius–Mossotti factor, indicating that separation must also be based on differences in bioelectrical phenotype as well as geometry. Some degree of heterogeneity should be expected in any cell population. For highly similar cell populations, 100% separability likely would not occur, as the phenotype distribution of one subpopulation and of the other subpopulation will overlap to some degree. Some cells within the less malignant MOSE-L population will have some probability of becoming more aggressive and similar to $MOSE - L_{TICv}$ due to in vitro adaptation, and some cells within the highly malignant $MOSE - L_{TICv}$ population might have characteristics that more closely match to the MOSE-L population. However, if the chip is able to enrich subpopulations in different proportions from the initial cell population

given that the average malignancy for the MOSE-L and $MOSE - L_{TICv}$ cell cultures differ, then the chip is able to sufficiently distinguish between the cell populations by phenotype even though the possibility of 100% separability may not exist. These subpopulations, once off-chip, can be studied and different treatments can be tested against them, as a differential rate of cell death due to a certain treatment in each of the off-chip populations will correlate with the higher proportion of cells in that off-chip subpopulation.

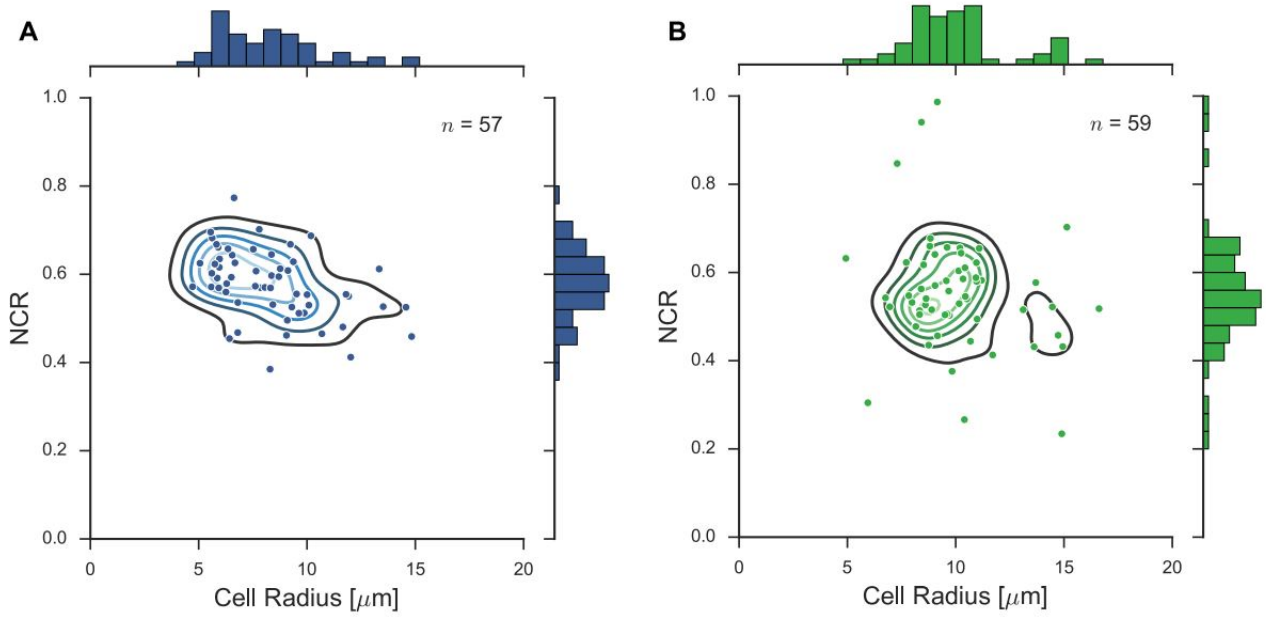

Figure 3.3: (A) Cell radius and nucleus-to-cytoplasm ratio (NCR) for MOSE-L cells. (B) Cell radius and NCR for $MOSE - L_{TICv}$ cells. $MOSE - L_{TICv}$ compared to MOSE-L cells have larger radii on average and a more uniform cell radius for the population compared to MOSE-L cells, which appear to have divergent characteristics around a smaller radius. $MOSE - L_{TICv}$ cells also have a lower nucleus to cytoplasm ratio than MOSE-L cells on average.

In previous studies, we have shown that because the DEP force is dependent on the gradient of the electric field squared rather than its magnitude, using 20 μm posts in the device improves separation specificity by reducing cell clumping and pearl chaining, a process involving a strand of cells forming in response to the DEP force. Cell-size posts also maintain

high viability in the output population by maximizing the ratio $\nabla(\vec{E} \cdot \vec{E})$ while still being large enough to trap cells [12]. By limiting to single or two cell trapping, as shown in Fig. 3.1 and combining this with flow rate dependent sorting, highly similar cells are able to be separated with a high degree of specificity while maintaining very high viability in the output population. This flow-rate DEP separation adds a new technique to the toolbox of DEP researchers.

3.5 Concluding remarks

Using our microfluidic device, we were able to separate highly similar cell lines based on their bioelectrical differences. These cell lines originated from the same cell line source, and therefore provide an in vitro model that can replicate behavior expected during evolution of tumor heterogeneity in vivo. We showed that by optimizing flow rate in the device, force balancing on cells is improved and can lead to higher separability of cells with similar bioelectrical phenotype, a result previously not shown in dielectrophoresis. The use of shear flow add to the armamentarium of DEP researchers for enhanced cell separation for their particular application, by providing another parameter that can be controlled to optimize separation and characterization.

Chapter 4

Separation of Macrophages and Fibroblasts using Contactless Dielectrophoresis and a novel ImageJ macro

Temple A. Douglas[1,3], Nastaran Alinezhadbalalami[1,3], Nikita Balani[1,3], Eva M. Schmelz[2,3], Rafael V. Davalos[1,3]

[1] Virginia Tech - Wake Forest School of Biomedical Engineering and Sciences, Kelly Hall, 325 Stanger St., Blacksburg, VA 24061

[2] Virginia Tech Department of Human Nutrition, Foods and Exercise, 1981 Kraft Drive, Blacksburg, VA 24061

[3] ICTAS Center for Engineered Health, Kelly Hall, 325 Stanger St., Blacksburg, VA 24061

Authorship Confirmation Statement: TAD, NB and NA performed experiments. TAD wrote the ImageJ code and performed the analysis. TAD, RVD, EMS, and NA contributed to the manuscript writing. EMS prepared the macrophage and fibroblast cells.

This article is currently under review at Bioelectricity.

A portion of this article has been posted to the bioRxiv preprint server at https://doi.org/10.1101/292417.

Macrophages and fibroblasts represent distinct cell types that are often found to be associated with tumors. This study presents a label free method of separating these cells. Contactless dielectrophoresis devices were used to separate fibroblasts from macrophages by selectively trapping one population. An ImageJ macro was developed to determine percentage of each population moving or stationary at a given point in time in a video. We observed a large parameter range that could be used to as a separation range. At 350 Vrms, 20kHz and $1.25\mu l/min$, more than 90% of fibroblasts were trapped while less than 20% of macrophages trapped. Contactless dielectrophoresis was used to study macrophage and fibroblast separation as a proof-of-concept study for separating cells in the tumor microenvironment. The associated ImageJ macro could be used in other microfluidic cell separation studies.

4.1 Introduction

Immune cells are actively recruited to the tumor microenvironment[73, 74]. In particular, macrophages and fibroblasts are often found as accessory cells[75, 76]. They have critical functions such as immune suppression[77], angiogenesis support and extracellular matrix remodeling (macrophages)[78] or provide structural and metabolic support (fibroblasts)[79]. Understanding the molecular mechanisms of how the tumor microenvironment modulates the phenotype of resident and how recruited cells contribute to tumorigenesis is critical for the development of treatment strategies that could suppress the development of tumor-supportive phenotype of the tumor-associated cells to suppress tumor growth and progression. For this reason, it is important to be able to separate and characterize specific cell types out of biopsies as a processing step. Here we demonstrate a method known as dielectrophoresis (DEP)

for separating different cell types. DEP is a phenomenon in which particles, in this case cells, exposed to the gradient of an electric field are polarized depending on characteristics of the cells and the medium that surrounds them. This polarization induces movement of the cells along that gradient.[13] This phenomenon can be used to trap cells, or divert them from normal streamlines [30, 47]. Characterization of these cell types using DEP has been previously performed [47] but cell separation has not been achieved before.

We have previously developed a technique called contactless dielectrophoresis in which a microfluidic device has contactless fluidic electrodes filled with conductive fluid that are used to apply an electric field across a chip, as shown in Figure 1. The use of contactless electrodes for dielectrophoresis, cDEP, eliminates problems with electrolysis and improves cell viability in the chip.[9, 12, 47] Small 20 μm insulative posts within the chip create inhomogeneities in the electric field. Cells with different bioelectrical phenotype will begin trapping at different applied electric field frequencies. By modulating the applied frequency, we can selectively trap some cells while allowing others to pass through the device. This selectivity allows separation of highly similar cell types in a label-free manner while maintaining high cellular viability such that they can be cultured or further characterized downstream.

A common difficulty that arises in analyzing microfluidic batch separation is the problem of determining how many objects are moving at each point in time in a video. This is particularly important in applications of dielectrophoresis, where cells are often trapped or immobilized in part of the device, and quantitatively determining the fraction of cells immobilized as a function of applied frequency and voltage becomes critical. This study presents the separation of macrophages from fibroblasts using contactless dielectrophoresis, a label-free microfluidic technique. This is the first time separation of these cells has been

accomplished using DEP.

In this paper, we present a new ImageJ macro that provides a method of obtaining videos during microfluidic dielectrophoresis experiments and extracting in each frame of the video which cells are moving vs stationary, the size of each cell, and what percentage of each cell type is trapped. As an example, we are using a mixture of macrophages and fibroblasts, representing different cell types that are found in the tumor microenvironment and contribute to a permissive microenvironment. Other applications, such as microfluidic chemotaxis assays, devices for fluid dynamics studies using fluorescent beads as flow markers, and circulating tumor cell (CTC) sorting applications could also benefit from this software.[80, 81]

4.2 Theory

The DEP force balanced with the drag force governs the behavior of cells in this device. When an AC electric field is applied, cells are polarized. Depending on the sign of the DEP force, which depends on the sign of the Clausius-Mossotti factor, cells are pushed in the direction of or antiparallel to the electric field gradient. The Clausius-Mossotti factor is written as:

$$K(\omega) = (\epsilon_p^* - \epsilon_m^*)/(\epsilon_p^* + 2\epsilon_m^*) \tag{4.1}$$

In this equation, ϵ_p^* is the complex permittivity of the particle or cell, and ϵ_m^* is the complex permittivity of the medium. The form of this is $\epsilon^* = \epsilon - i\sigma/\omega$. The DEP equation for a dipole is then written as:

$$\vec{F}_{DEP} = 2\pi r^3 \epsilon_m Re(K(\omega))\nabla|\vec{E}_{rms}|^2 \tag{4.2}$$

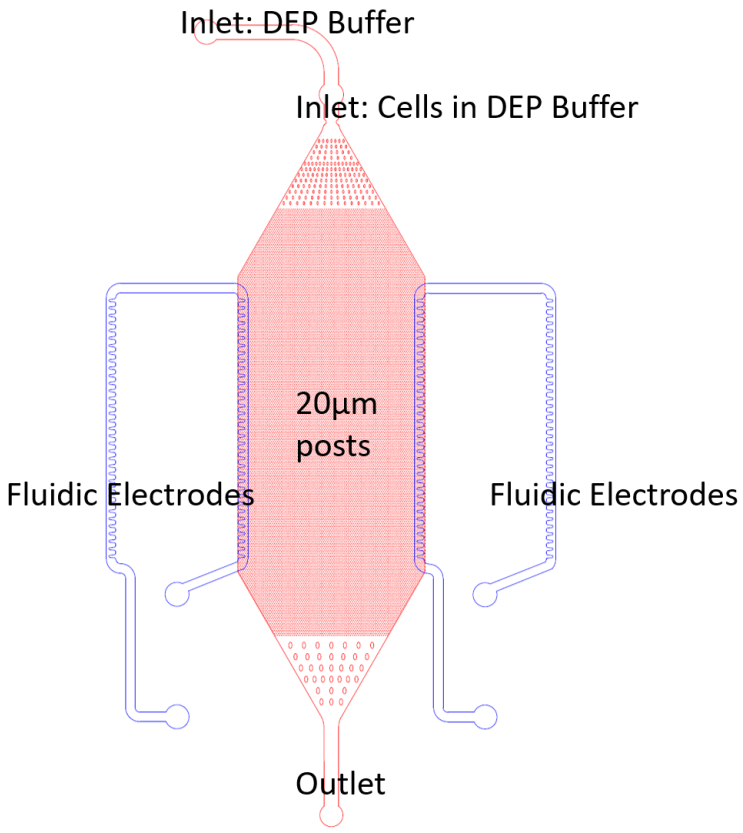

Figure 4.1: Schematic of chip design. Blue lines show fluidic electrodes, which are separated from the channel (red lines) in the z direction by a $14\mu m$ membrane of spun PDMS.

where r is the cell radius, ϵ_m is the conductivity of the medium, $Re(K(\omega))$ is the real part of the Clausius-Mossotti factor as a function of angular frequency (ω), and $\vec{E}_{rms}$ is the root mean squared of the electric field. Conveniently, the DEP equation is separable into distinct components. $\vec{F}_{DEP}$ as a function of only cellular properties and medium properties is proportional to $r^3\epsilon_m Re(K(\omega))$ whereas the DEP equation as a function of the chip geometry is proportional to $\nabla|\vec{E}_{rms}|^2$, simplifying modeling.

4.3 Materials and Methods

4.3.1 DEP Chip and Buffer

As discussed in previous works[9, 12, 26, 47], the DEP chip design consists of three layers, as shown in Figure 3.1. It has one fluidic electrode into which 10x phosphate buffered saline (PBS), a highly conductive solution, is added. Wires are inserted into pipette tips full of 10x PBS, and this is attached to a signal generator (Agilent 33500B Series), amplifier (Trek Model 2205) and oscilloscope for monitoring. The chip also has a channel layer with 20 μm diameter insulating posts. When voltage is applied across the chip, electric field gradients exist around these posts. The channel and electrode layers are separated from each other by a 14um membrane made from polydimethylsiloxane (PDMS) (Dow-Corning) spun at 4000rpm on a silanized silicon wafer (University Wafers) and then plasma bonded to the other layers[9, 12]. For this reason, cells are transferred into a low conductivity DEP buffer containing an isotonic solution of 8.5% sucrose (w/v) (Sigma), 0.3% glucose (w/v), and 0.725% RPMI (v/v) (ATCC). To perform this transfer, cells are centrifuged three times in 10 mL of DEP buffer with an added 0.1% bovine serum albumin (w/v) (Sigma), 0.1% of Kolliphor P188 (w/v) (Sigma) , and 0.1mM EDTA (Boston BioProducts). Following this step, cells were strained through a 40um cell strainer (Corning), conductivity was measured using a handheld conductivity probe (Horiba), and cells were diluted in DEP buffer without additives to a concentration of less than 1 million cells per mL.

4.3.2 Cellular Experiments

As a proof-of-concept study, we conducted first DEP trapping experiments on separate murine fibroblast (OP9, from ATCC) adherent cells and murine peritoneal macrophage

(PMJ2-PC1, from ATCC) suspensions to determine frequency/voltage/flow rate pairings at which these cells would trap. OP9 cells were grown on adherent dishes with in a media of MEM alpha (Sigma Aldrich) with 20% (v/v) FBS (Atlanta Biologicals), 2.2g/L sodium bicarbonate, and 1% (v/v) penicillin-streptavidin. PMJ2-PC1 mouse macrophage cells were grown in suspension in DMEM (Life Technologies) with 5% FBS, 3.7g/L sodium bicarbonate, and 1% penicillin-streptavidin. Cells were transferred to DEP buffer through repeated centrifugation until a conductivity of under 120 $\mu S/cm$ was reached. First, each cell population was run through the deice. For a set of frequencies and voltages, videos were obtained of cells flowing through the device. For each voltage/frequency combination, we recorded whether or not cells were able to trap. A plot of these results is shown in Figure 3. We then performed a separation experiment using a mixture of fibroblasts, stained with calcein green (5 $\mu g/mL$, Life Technologies), and macrophages stained with calcein red (1.7 $\mu g/mL$, Life Technologies) for 15 min. Based on the results from individual population analysis as shown in Figure 3 we chose a flow rate of 1.25 $\mu l/min$, 20 kHz, and 346 Vrms to separate mixed cells in the device. We turned on the voltage, allowing cells to trap, and then turned it off to test if trapping was reversible. Occasionally we sped up the flow rate briefly to wash cells through the device. The software OBS (Open Broadcaster Software) was used to record the live view from the Leica X software, and notes were taken when the voltage was turned on/off, cells were washed, etc. Using VLC media player scene filter, the video was converted to two stacks of images for further analysis. An ImageJ script was written to analyze these video results. Further experimental details on contactless dielectrophoresis have been discussed at length in our previous publications.[9, 12]

4.3.3 ImageJ Script

The basic parameters for the code were developed using the macro record function. "Plug-ins>Macros>Record". A basic outline of the code was developed, following existing ImageJ protocols.[82, 83] The macro uses several packages from ImageJ including the Dialog package for providing a window for user commands. First, the command "getString(text question, text answer)" is applied. This command opens a quick dialog box with a single line of question and input without having to use the full Dialog command. Then, the image sequence of interest is opened. The commands File.getParent(source) and File.getName(source) are used to split the full path into the file name and the path without the filename. This is used in multiple places in the code to query the user. The code can be defined as functioning in eight distinct steps, with example outputs shown in Figure 4.2.

In the first step, the user is asked for the pathname for an image stack to be imported and whether the image is single- or multi-channel. Secondly, the color channels (if more than one) are split into distinct image stacks. The user is given the option to choose a thresholding method from standard ImageJ thresholding methods[84, 85, 86, 87, 88, 89, 90, 91, 92, 93, 94, 95, 96]. The program then automatically thresholds all images into black and white. The program then calls another standard ImageJ procedure, watershed, to separate clumps of cells into distinct entities before further processing[97]. Next, the program asks the user how many images will be used for the median process, and uses this to run a for loop that calls the process Z Project. In this process, for example, if the user inputs 5 images, then the program will compare images 1-5, assigning each pixel as black if that pixel is black in the majority of the first 5 images, and white if the pixel is white in the first five images. This "median processed" image containing pixels that correspond with the majority of the pixels in the original stack, will be exported into a new stack. The program will then do the

same analysis with images 2-6, 3-7, etc. until the end of the stack is reached. At the end, for each image stack, there will be a corresponding median processed stack containing only stationary cells. Next, the program calls the preinstalled ImageJ plugin Analyze Cells. The program asks for 4 parameters: minimum and maximum cell size in pixels, and minimum and maximum cell circularity. Using these parameters, the program calls Analyze Cells to count and measure each cell, produce new image stacks with outlines for each of the cells, and Excel spreadsheets with cell counts and sizes. Finally, the program saves all these files. An example of outputs is shown in Figure 2.

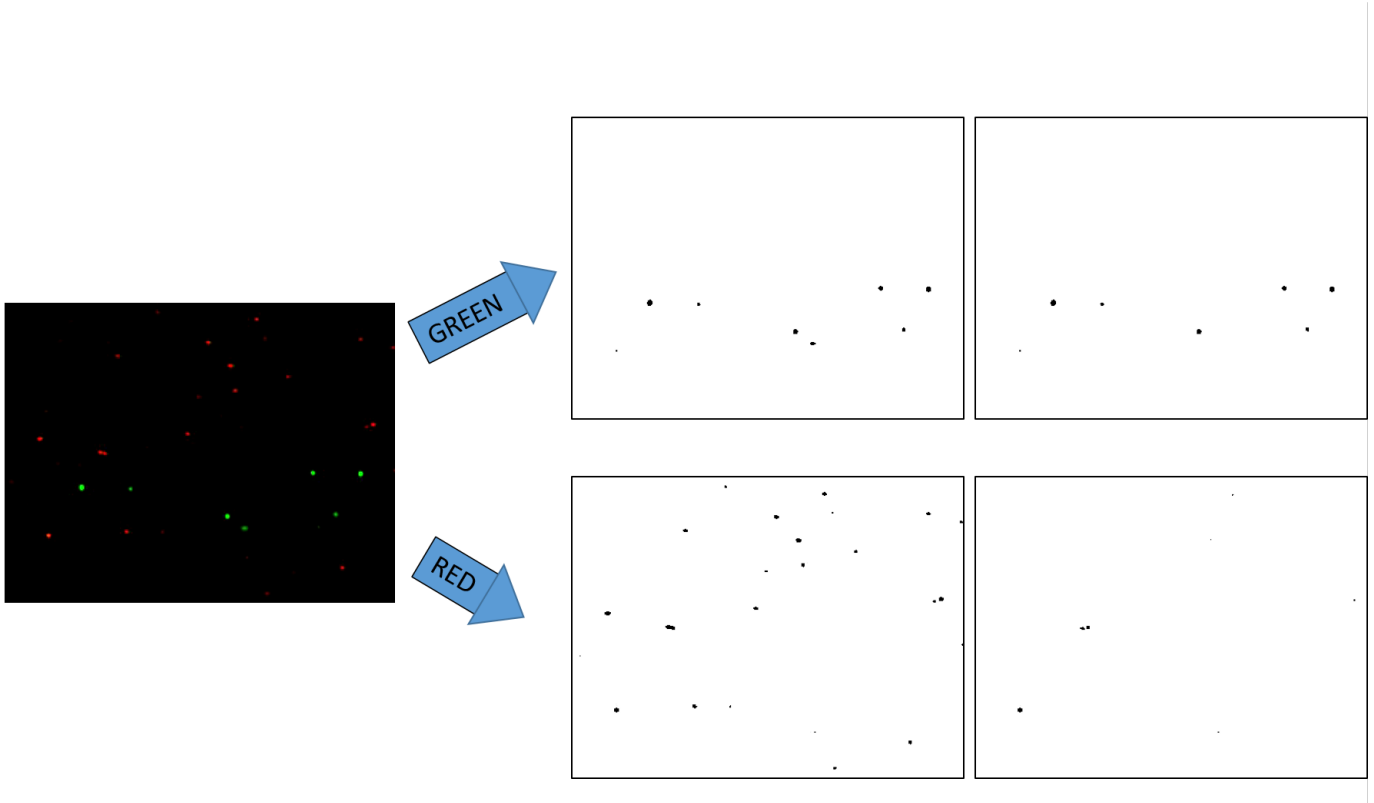

Figure 4.2: Examples from processed image stack. Videos are available in the appendix. The original video slice with fluorescent cells is shown, followed by the split and analyzed images of red and green stationary and total cells for the corresponding median image. Accompanying excel sheets show the cell counts for each slice in the stack.

4.4 Results

Previously we have shown that high flow rate can enhance separation of highly similar cell types[9]. In a second mode at much lower flow rates, bulk separation of more bioelectrically distinct cell populations was possible, and could be used to study a variety of cell combinations. There were a wide range of frequencies and voltages for which the macrophages were not able to trap but the fibroblasts were able to trap, including several frequency/voltage pairings for which the fibroblast population reached complete trapping.

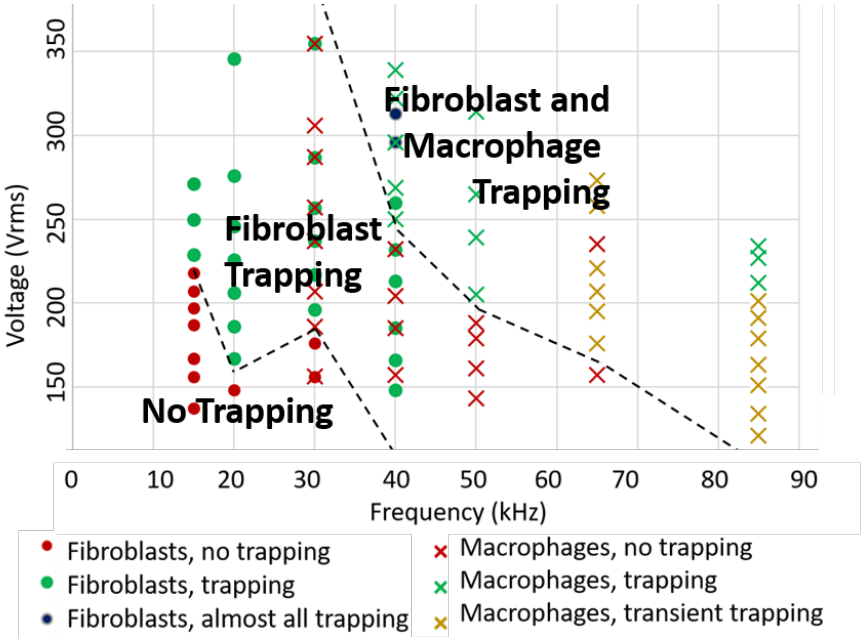

Figure 4.3: Fibroblasts and Macrophage trapping regions at 1.25 $\mu l/min$. Each point corresponds with a voltage-frequency pairing.

It is important to note that in Figure 4.3, the voltage required to trap cells decreased with increasing frequency. There are two reasons for this. First, this slope corresponds with the fact that the DEP force must be higher than the drag force on a cell to trap in the chip, and the DEP force per volt as a function of frequency increases with increasing Clausius-

Mossotti factor. Within this frequency range, the Clausius-Mossotti factor is in the upward slope regime between crossover frequency and plateau [72], leading to a stronger DEP force per volt applied. Secondly, in contactless dielectrophoresis, as the voltage drops across a membrane in the device, the field inside the chip increases per volt applied as a function of frequency. This is shown in Figure 4.4.

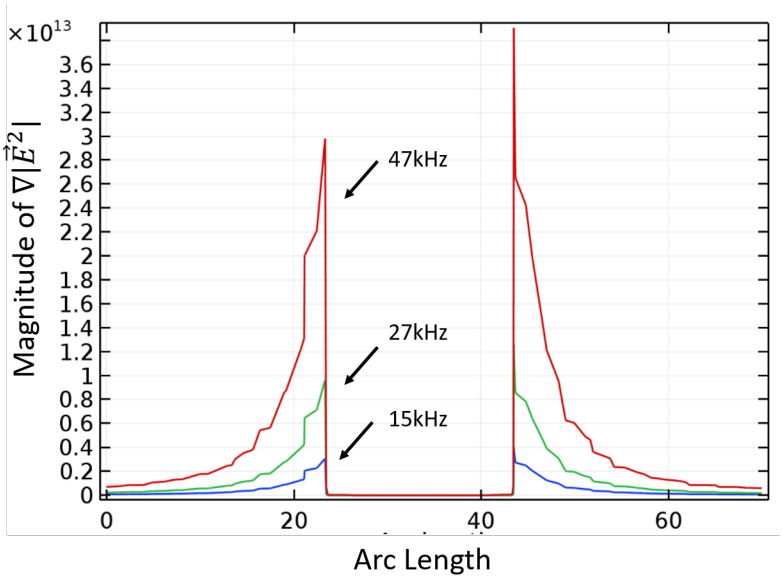

Figure 4.4: Magnitude of the gradient of the electric field squared, across a post in the direction of flow.

Within the region between the two dotted lines, trapping of the fibroblasts but not macrophages was possible. Below the lower dotted line, neither population trapped. And above the higher dotted line, both populations trapped. This gives a broad range of frequencies/voltages that are able to trap these cells, and this corresponds with significantly different bioelectrical phenotype between the two populations.

Based on the results from Figure 4.3, 1.25 $\mu l/min$, 350Vrms and 20kHz were selected to maximize trapping of the fibroblast population while remaining below the onset of trapping

for the macrophage population. The macrophages and fibroblasts were stained, mixed, and separated at 20 kHz, 346Vrms, and 1.25 $\mu l/min$. The cells were then recorded over a period of time with the voltage being turned on and off, and occasional washes. Output videos, excel files, the original data set and the macro code are included in the Supplemental Information, along with a user guide.

Figures 4.5 and 4.6 show the results of the cell separation analysis. The gray boxes represent areas with the voltage on, while white is area with the voltage off. The y-axis represents the fraction of cells trapping at each point in time. When the voltage was on, the majority (>90%) of the fibroblasts trapped while very few (<20%) to no macrophages trapped. In the instances of fibroblasts not trapping, they were a lighter shade of green, indicating leaking calcein and lowered viability. Instances of macrophages trapping were generally doublets. However, this imaging technique only analyzes a small region of the device, so it is possible that cells not able to trap here would eventually trap upon contact with another post off camera. The voltage was turned off periodically to ensure that any trapping was reversible dependent on voltage, an indicator that the trapping was due to DEP and not cell adherence due to other factors. Periodic washes were performed to ensure fresh batches of cells are flowing through the device and being trapped. This method of recording videos of cells moving and analyzing populations, while providing fewer data points than a downstream batch analysis, allows the researcher to rapidly screen parameters, and gives information on the average lag time between turning the voltage on and cells trapping and other important data.

Moments when the brightfield were on changed the signal shown in Figures 5 and 6 as the process is optimized for fluorescent videos. Similarly, when moving the stage or washing at high flow rate, the rate at which cells move with respect to the frame is very high. In order to

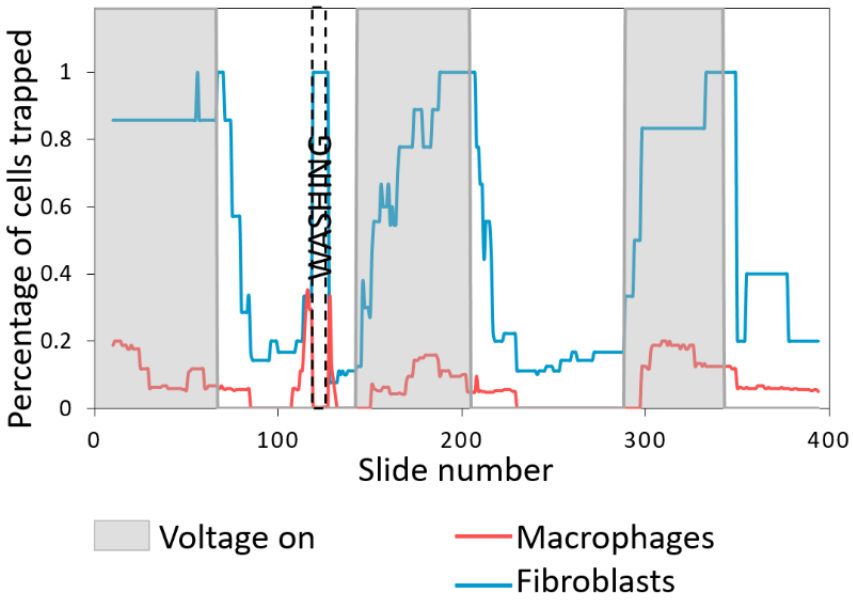

Figure 4.5: Analyzed data for image stack with 6 frames per second, 21 frames per median process, Otsu filtering [92], particle size 10-Infinity pixels, particle circularity 0.1-1. Graph shows percent of each cell type trapping at each point in time. As noted, a wash step was performed.

correctly count moving vs. trapped cells in this case, a much lower number of median frames would need to be used, and significant aliasing would likely be present. In addition, an artifact of the median processing system is that for a given slide, the number of cells counted as trapped can occasionally exceed the total number of cells, as an artifact of the fact that one slide for total counts must be compared to a set of n slides for the processing. However, this should average out over time. Some cells irreversibly trap, such that even when the voltage is removed they remain trapped, as can be seen in the baseline fibroblast trapping percentages.

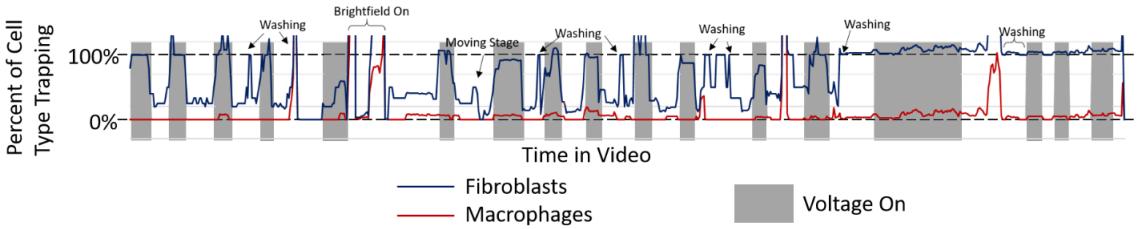

Figure 4.6: Analyzed data for image stack with 1 frame per second, 7 frames per median process, Otsu filtering [92], particle size 10-Infinity pixels, particle circularity 0.1-1. Graph shows percent of each cell type trapping at each point in time. Multiple wash steps were performed, brightfield was turned on, and stage was moved to represent different kinds of noise levels.

4.5 Discussion

We hypothesize that the excellent separation between the two populations relates to their size as well as the structure of the cells, with fibroblasts being highly elongated in culture, and the macrophages being spherical and nonadherent. Changes in the cellular morphology have been shown to correlate with changes in the DEP force and in the strength of multipolar behavior[98, 99, 100, 101]. Even though the cells were trypsinized, they could have retained some degree of cytoskeletal organization reminiscent of their in vitro shape, which could lead to differences in DEP trapping. Cell size also likely contributed to the difference in trapping. We observed that of the macrophages trapping in the fibroblast range, they appeared to be doublets, or two cells stuck together. Similarly, fibroblasts that did not trap appeared to be dying, as they did not contain as much calcein green and appeared less bright in the images. We observed an interesting phenomenon at high frequencies, where cells would redirect from their streamlines to the posts, indicating dielectrophoretic trapping, but would release before the voltage was turned off. In Figure 4.3 we called this phenomenon transient trapping. To our awareness this phenomenon has not been previously observed in other cell types. This phenomenon could be electroporation, although if so, higher voltages at the

same frequencies would not cause DEP trapping. It is also possible some kind of mechanism related to multipolar behavior or electrorotation of the trapped fibroblasts could contribute to this behavior.[13, 72, 98]

One drawback to the ImageJ algorithm for tracking and analyzing cells is the slight blurring of voltage on-off boundaries by using the median method. When determining whether a cell is moving, the program needs to reference a sequential subset of images. For example, if 15 images are used to determine if the cell is moving, the first image in the median processed (moving vs. stationary) plot is made from taking the majority of the pixels from images 1-15. If, for example, the voltage was turned on between images 3-4, then the first median processed image will show that the cells were trapped. This can be somewhat compensated for by correlating the set with an image in the center of that set, for example, assigning the median image set 1-15 with original image 7, 2-16 with original image 8, etc. One way of analyzing, which was performed in Figures 5 and 6, was to divide the number of cells counted in each median processed image (stationary cells) by the total number of cells in the central image from that median set. However, leaving these variables open to user input makes the algorithm flexible for a variety of imaging setups, with different sizes, shapes, and densities of cells.

The development of an ImageJ macro for analyzing videos of moving vs. stationary cells can help to speed and automate the analysis of multiple microfluidic device configurations. It can be very helpful for applications such as ours in the area of dielectrophoresis, where it is necessary to determine percentage of cells trapped by an electric field. In using this macro, it is necessary to optimize the run parameters before analyzing a full data set, to prevent over or undersampling of data. The standard thresholding methods in ImageJ can be used to test

different threshold methods before running the program. To optimize the parameters for the median processing and subsequent cell analysis, it may be useful for the researcher to create a file containing a subset of the total number of images for iterative testing, to speed the optimization process. If the number of images chosen is too large, the averaging mechanism may erase some trapped cells. If the number of images chosen is too small, then slow moving particles will show up as trapped. In this case it is also common to see significant levels of noise, where pieces of particles are visible in one frame of the median processing and absent in the next frame. In the future, this macro could be developed into a full ImageJ plugin or integrated into video processing software so that cell trapping percentages could be analyzed in real time, allowing researchers to obtain data while running experiments. This could help to speed up the optimization of dielectrophoretic setups where optimizing frequency-voltage pairings is necessary to optimize device functionality.

4.6 Conclusions

We have shown separability of macrophages and fibroblasts using our DEP device. In order to rapidly analyze these results, we developed an ImageJ installable macro that can be used to count moving vs. stationary objects. This code can be used in the future to make processing of DEP data much faster and quantitative. The current version is optimized to be used with moving vs. stationary, fluorescently labeled cells or particles. However, it is easily modifiable for novel applications, and also comes with user-friendly dialog boxes for easy programming-free input. The code has the DOI 10.5281/zenodo.1204436 at Zenodo, https://zenodo.org/. The code and user guide are also found in the appendix.

Chapter 5

Dielectrophoresis Downstream Analysis: Microfluidic Culture Chamber for 3D Cell Morphology Study with Chemotherapy Multiplexing

T. A. Douglas[a], E.M. Schmelz[b*], and R. V. Davalos[a*]

a. Virginia Tech - Wake Forest School of Biomedical Engineering and Sciences, Virginia Polytechnic Institute and State University, Blacksburg, VA, USA

b. Department of Human Nutrition, Foods and Exercise, Virginia Polytechnic Institute and State University, Blacksburg, VA, USA

Authorship Confirmation Statement: TAD performed experiments. EMS provided cells. TAD wrote the manuscript.

This article is currently being drafted to be sent for publication.

This work presents a system to integrate the separation of cells by their bioelectrical phenotype using contactless dielectrophoresis (cDEP) with an automatic downstream 3D culture with sterile cell transfer from low-conductivity buffer to media and 3D hydrogel. Ultimately, this will be combined with a small molecule multiplexing chamber for combinatorial subpopulation analysis. cDEP is a technique that utilizes insulator posts in an applied electric field to create local inhomogeneities in the electric field and selectively trap cells based on their biophysical phenotype, which we have shown can be used to separate highly similar tumor cells. These cells once off-chip are label free and highly viable, such that they can be subcultured and analyzed via a variety of live-cell techniques. Here, a cell concentrator concentrates cells as they move off-chip and moves them from low-conductivity buffer to an uncured 3D hydrogel matrix. This could be followed by a second step where cells flow into a hydrogel channel to be cultured in 3D hydrogel while being exposed to different concentrations and gradients of different chemotherapies or other diffusible molecules. This device would act as a screening device to test each subpopulation individually against a chemotherapy. With this information, computational models can be built to understand the effect of dosage and timing of each subpopulation relative to one another in the context of a solid tumor in vivo. This article demonstrates a proof-of–concept for a method of flowing cells into uncured hydrogel so that they can be cured in hydrogel in a microfluidic device.

5.1 Introduction

Cancerous tissue is heterogeneous in nature, often containing several subpopulations of cells with varying degrees of aggressiveness and susceptibility to different types of chemotherapy[1, 59, 102, 103, 104, 105, 106, 107]. Currently, cancer treatment tends to treat the bulk

of a tumor, often leaving behind treatment-resistant cells that can then repopulate the space, during which they evolve in a new microenvironment, leading to treatment resistance and recurrence[3, 55, 75]. Despite numerous studies, the complexity of determining which treatments will be most effective in different scenarios is still unsolved, with some evidence showing that unoptimized application of chemotherapy can mutate the surviving cells, which can increase heterogeneity and in turn lead to the emergence of more aggressive and metastatic subpopulations [5, 6]. In particular, attempts to treat metastatic cells often fail, leading to death in many cases[8]. One particularly worrisome aspect during tumor evolution is the development of metastatic subpopulations. Research has shown that the epithelial-to-mesenchymal transition (EMT), the process by which cells obtain traits that increase their ability to migrate, is crucial in this process and involves single-cell evolutionary processes[107, 108]. We hypothesize that a necessary-and-sufficient aspect of this transition involves changes to the structure of the cell membrane that allow the cell to migrate and to pass through capillary walls to circulate and move to other sites, with this behavior correlating with the EMT.

Contactless dielectrophoresis (cDEP) is a technique that uses an applied AC electric field to induce cellular polarization in a microfluidic device containing an array of cell-sized posts[10, 26, 38]. These posts are insulative: the electric field gradient induced around the posts causes cells to migrate toward the posts and trap if the electric field is on. Cellular polarization in dielectrophoresis is frequency-dependent and is dependent on cellular characteristics. Therefore, only some cells will trap if their bioelectrical phenotype allows polarization at a certain frequency and the force on the cell outweighs the Stokes drag force on the cell[13, 22].

Dielectrophoresis theory suggests that changes to the structure of the cell membrane can change the frequency at which a cellular dipole is induced[72]. By this logic, changes in the structure of the membrane correlating with the EMT should be quantifiable using low-frequency contactless dielectrophoresis. We have shown that using cDEP, mouse ovarian surface epithelial cells at different stages of malignancy can be separated with DEP, while also retaining high viability[9, 11, 12]. This indicates potential for the device to separate tumor subpopulations for further characterization.

We hypothesize that the development of a multistage cDEP device can improve chemotherapy selection by allowing for morphologically unique cells to be separated based on their electrical polarizability and tested separately against an array of chemotherapies. We hypothesize that changes in the structure of the cell membrane correlating with EMT are a major contributor to this difference in cellular trapping. Having a downstream cell culture device would a) allow validation studies on this correlation to be performed in a rapid and reproducible way, and b) provide a method for systematically studying bioelectrically distinct tumor subpopulations for markers in 3D culture: cellular aggressiveness, motility, growth rate and response to chemotherapy, immunomodulatory molecules, or anything else that can be diffused in hydrogel.

In the future, this device is envisioned to be used as follows: upon receiving a tumor biopsy, cells flow through the dielectrophoretic cell separator where they are separated by their subtype, flow through a system that transfers them to uncured hydrogel, and then flow into a culture chamber where they can be cultured in 3D as an indicator of metastatic capacity. This is followed by testing chemotherapy agents against each cell subtype individually. Using these data (for each subtype, growth rate, malignancy and susceptibility to a panel

of chemotherapies or other treatments), we hope to pair this single-chip diagnostic with a computer algorithm that will model optimum treatment regimens based on output data.

This manuscript presents a proof-of-concept study for the concentrator portion of the proposed downstream culture device, shown in Figure 5.1. Theoretical models, computational analysis, and experimental proof-of-concept studies demonstrate feasibility of the concentrator step in the downstream device.

5.2 Theory

Neutrally charged lossy particles and cells exposed to an inhomogeneous electric field experience a dielectrophoretic force:

$$\vec{F}_{DEP} = 2\pi\epsilon_m r^3 ReK(\omega)\nabla|\vec{E}_{rms}|^2 \tag{5.1}$$

Here, r is the radius of the cell, $\vec{E}_{rms}$ is the root mean square of the electric field, ϵ_m is the permittivity of the medium, and $K(\omega)$ is the Clausius–Mossotti factor[13].

The Clausius-Mossotti factor is described by $K(\omega) = (\epsilon_p^* - \epsilon_m^*)/(\epsilon_p^* + 2\epsilon_m^*)$ where $\epsilon^* = \epsilon + i\sigma/\omega$, with ϵ^* the complex permittivity, ϵ the permittivity, σ the conductivity, and $i = \sqrt{-1}$. The subscripts p and m represent the particle and medium, respectively. The dielectrophoretic force can thus be used to separate cells based upon their radii, the dielectric permittivity of the cells, and the frequency of the applied voltage. By tuning the frequency of the applied voltage, the cDEP chip can attract and trap a subpopulation of the cells to the insulated posts while other subpopulations are repelled[10, 13]. In addition to the dielectrophoretic

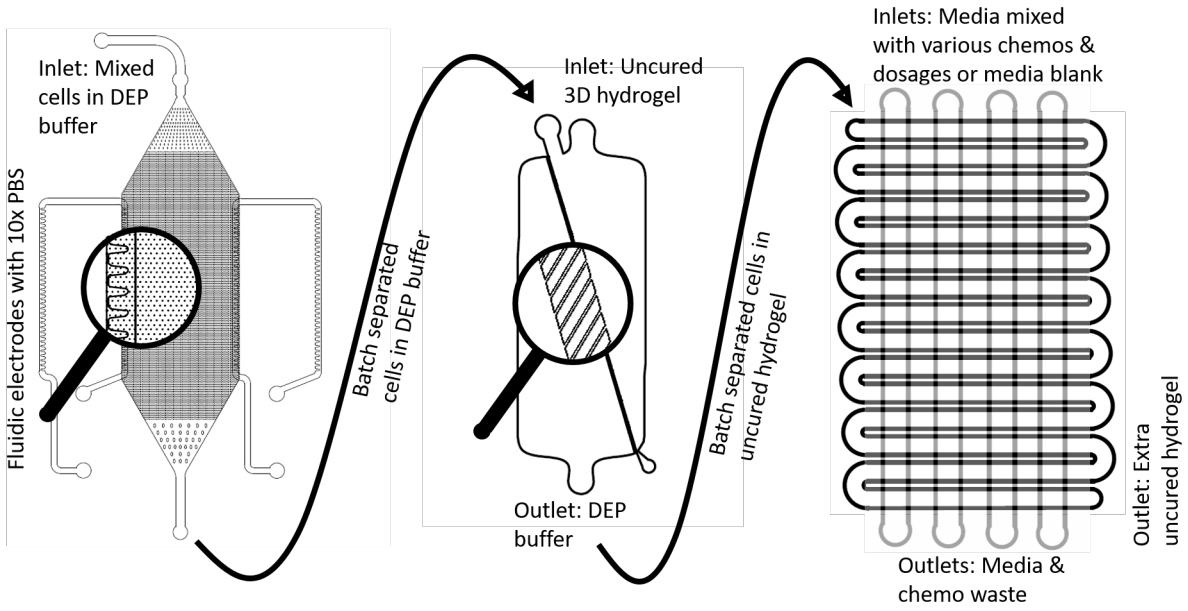

Figure 5.1: Schematic shows separation and culture process. Mixed cell subpopulations first flow into a device with 20 μm diameter posts. Fluidic electrodes filled with highly conductive phosphate buffered saline at ten times physiological concentration are used to apply an electric field across the device. Cells in response to the electric field trap on posts based on their unique electrical phenotype, while untrapped cells are washed out. When voltage is turned off, trapped cells are also washed out, resulting in plugs of different phenotypes of cells downstream. These cells then run into a concentrator, where a wall of 7.5 μm pores siphons off the DEP buffer and pushes cells into uncured 3D hydrogel. This hydrogel and cell mixture, still in batches, runs into a downstream chamber where the hydrogel with cells is then cured in distinct subpopulations. An array of buffers can be diffused into the channel across a membrane with 0.4 μm pores. Information from this device, including cell morphology in hydrogel as an indicator of aggressiveness, growth rate and response to chemotherapy or other small molecules diffused across the pores can be fed into a computer optimization model to determine the effect of combinatorial therapy on a theoretical solid tumor containing these subpopulations.

force, cells in a DEP chip also experience the drag force, which balances with this DEP force to optimize trapping [12].

Downstream of the cDEP chip, the cell concentrator is designed to concentrate the cells in a smaller amount of low conductivity DEP buffer while simultaneously exchanging the low conductivity buffer used in the DEP experiments with uncured hydrogel. This design accomplishes these two tasks using a diagonal wall with small pores that acts as a sieve. The small size of the pores prevents cells from passing through the wall and forces cells to move along the edge of the porous wall into an outlet. Because the wall of pores has a higher net cross-sectional area than a secondary outlet, the low conductivity DEP buffer exits the device while the cells are mixed into the hydrogel before reaching the outlet. This device allows the system to be fully microfluidic, avoiding cumbersome centrifugation steps in order to move the cells from DEP buffer to hydrogel, and potentially compromising sterility. A labeled schematic of this device is shown in Figure 5.2.

5.3 Modeling

COMSOL particle tracing was performed to study the cell concentrator. The laminar flow module was used to model streamlines and pressure in the chip. The inlet flow rates were set to 0.0007 m/s in each inlet. Streamlines, pressure in the device and flow velocity are plotted in Figure 5.3.

The particle tracing for fluid flow module was used to study particle behavior in the chip. 15 μm particles were modeled using the flow profile. The results from this modeling are shown in Figure 5.3.

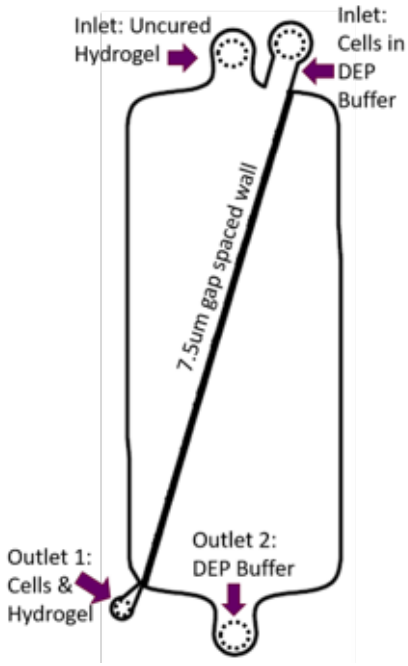

Figure 5.2: Schematic of concentrator design with labeled chip regions.

5.4 Experimental Methods

5.4.1 Chip Fabrication

The mold for the concentrator along with 7 other variations on the pattern were fabricated using deep reactive ion etching (Bob Geil, UNC) on a silicon wafer using a soda-lime mask (Photo-Sciences). The channel height is 95 μm. The wafer was silanized to improve polymer lift-off. To make the chip, Sylgard-184 polydimethylsiloxane (PDMS) was mixed in a ratio of 5:1 w/w base to cross-linker, was degassed and cast molded. The increased ratio of cross linker (compared to 10:1) was used to increased stiffness so that the posts in the chip would not collapse. The chip was cured for 1.5 hours at 150^{o}C. The longer and hotter curing time was chosen to also increase material stiffness. Immediately upon removing the PDMS from the mold, 0.75 mm holes were punched for inlets and outlets and the chip was plasma bonded to glass (Harrick). The chip was not cleaned with tape as this will damage the fragile posts.

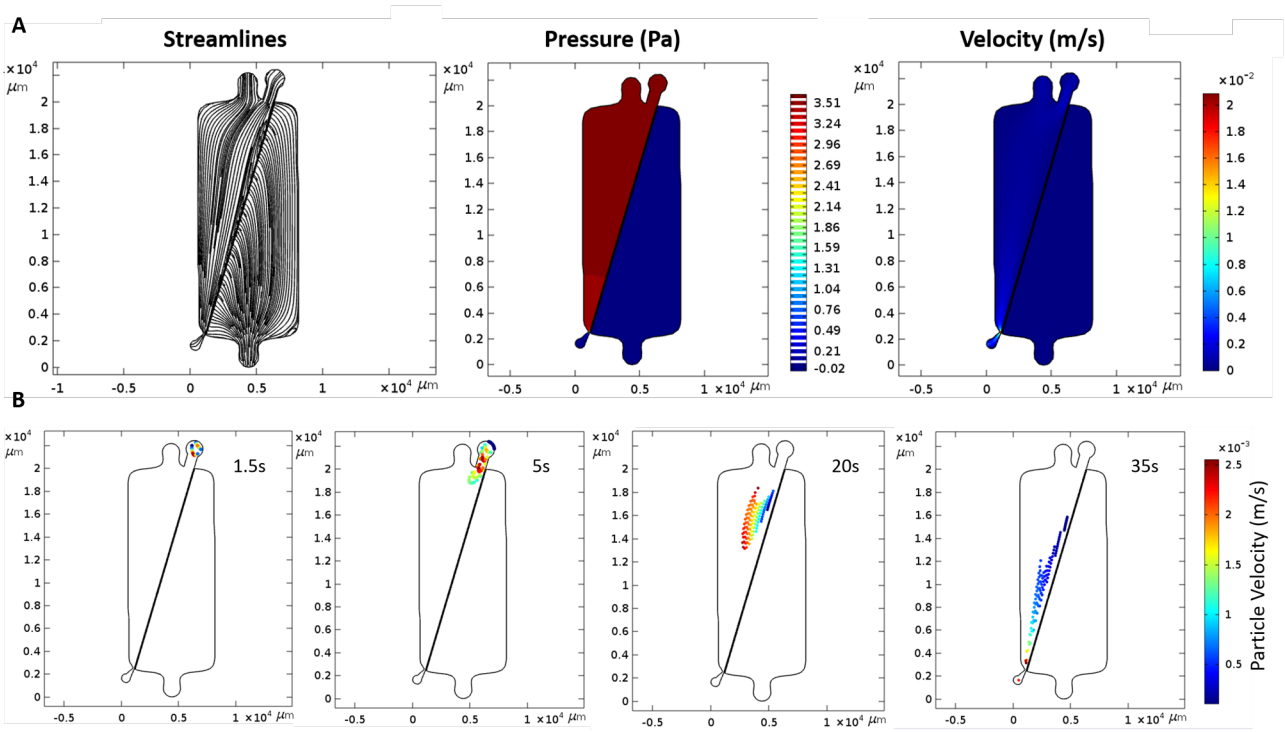

Figure 5.3: a) COMSOL model of streamlines in the concentrator. Note that the porous boundary and constricted left hand outlet creates a pressure driven flow system where some fluid is siphoned off into the second channel. b) Particle tracing for 15 μm particles in the concentrator channel.

The concentrator layer was plasma bonded to a glass slide and placed in a vacuum until use.

5.4.2 Choice of Hydrogel

Several hydrogels were selected and tested during this process. We observed that very high viscosity hydrogels can damage fine microfluidic features and/or fail to load into a chip. In addition, bubble formation in higher viscosity gels is nearly impossible to resolve. Gels that cure rapidly or cure in response to temperature are also not good candidates, as gelation occurs at nucleation sites and does not occur uniformly. This makes loading a microfluidic device nearly impossible. For this reason, Glycosil (ESI-BIO) was chosen as it cures very slowly over a 24 hour period with eventual autocrosslinking [109, 110]. It is a hyaluronic acid hydrogel that when resuspended creates a 1x PBS environment[111], making it a good candidate for mixing with cell media and flowing into a device for further diffusion of media into the gel.

5.4.3 Testing Particle Concentration

Before running an experiment, the chip was left 2 hours under vacuum to degas. To load the chip, there must never be a high surface tension within the device, as this will damage the posts. Therefore, the chip was primed first with ethanol, then with DI water, before adding the hydrogel. To test cellular motion within the device for comparison with COMSOL modeling results, 15 um red labeled polystyrene beads (Invitrogen) in DI water were flown in through the cell/DEP buffer inlet. 15 μm blue beads (Invitrogen) in DI water were mixed 1:1 with Glycosil (ESI-BIO) and flown in through the hydrogel inlet. Blue beads were used as a way to trace the motion of the hydrogel in the device, even though they cannot go through the pores. Each mixture was loaded into syringe pumps. First, buffer was flown in

at $1\mu l$/min until the chip was loaded with beads. The buffer feed speed was then increased to 2 $\mu l/min$ until there was sufficient effluent at the outlets. This effluent was collected and the volume was measured. A hemocytometer was used to count the number of red/blue beads in the output.

5.4.4 Testing Buffer Siphoning

To test the mixing of different subpopulations in the chip, DI water was run into the channel DEP buffer/cell inlet, and 1x PBS mixed with the prepared glycosil was run into the hydrogel inlet. The chip was primed with ethanol, then DI water. The buffer solutions were loaded into 1ml syringes, attached to syringe pumps (Harvard), and connected to the chip. A flow rate of 2 $\mu l/min$ was used through each of the inlets. Short pieces of empty tubing (PTFE 22 gauge) were attached to the outlets and buffer ran out into these. When the tubes were about 2/3 full, they were removed from the chip and the fluid was unloaded into a microcentrifuge tube. This outlet fluid was mixed to make a 12.5% outlet solution in DI water. The conductivity of these solutions was measured with a conductivity meter (Horiba).

5.5 Results

Figure 5.4 shows the result of particle flow through the chip. The flow was stopped to image the distribution of particles in the chip. 15 μm blue beads were used in the inlet with hydrogel to help visualize flow, and $15\mu m$ red beads were input in the other inlet. The beads for the most part did not pass the semi-permeable wall but flowed out the device. Some particles stuck in the grate of the device, but it may be possible to alleviate this by

optimizing flow rate to enhance inertial effect of the beads.

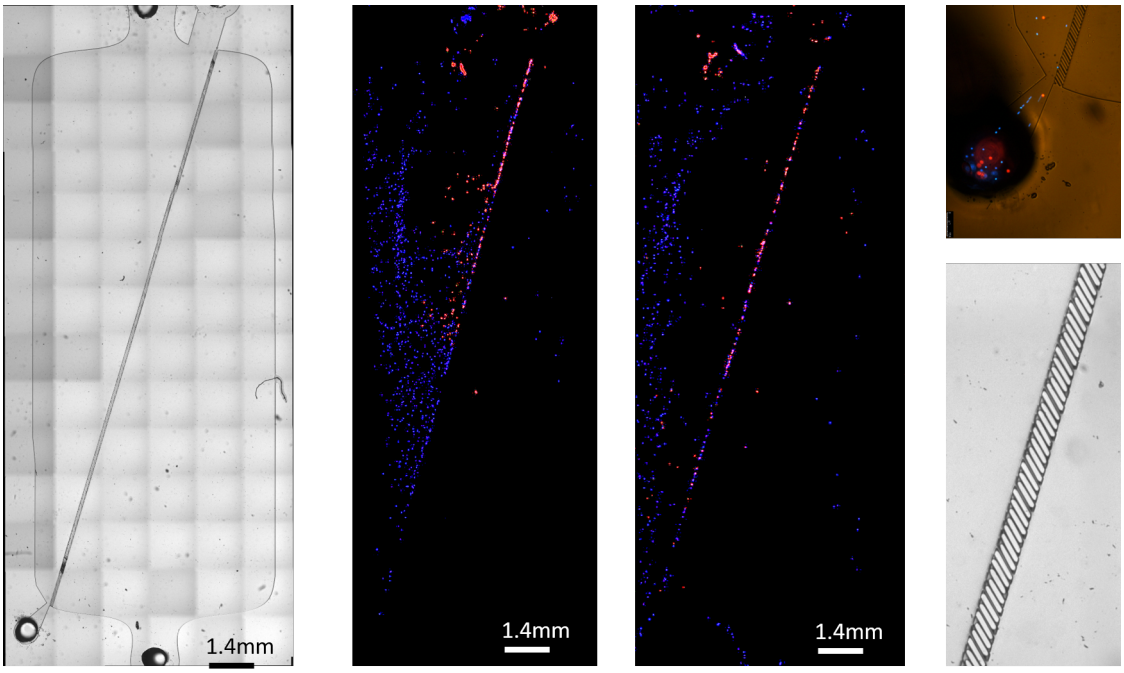

Figure 5.4: From left to right: Concentrator image showing punch holes (dotted lines), gap spaced wall, inlets and outlets. Brightfield image of chip made in PDMS. Fluorescent beads in the chip when flow at $1\mu l$/min was paused. Fluorescent beads in the chip when flow at $2\mu l$/min was paused. Combined brightfield/fluorescent image of outlet with beads flowing into it. Brightfield image of post structure.

At the output of the device, beads were collected and counted using a hemocytometer. 8 μl of fluid came out each outlet indicating relatively equal fluid output. Counts from each outlet are shown in Table 5.1.

Table 5.1: Output of chips in particle tracing experiment.

	Red Beads	Blue Beads	Output Volume at 2 $\mu l/min$
Outlet 1	53	282	8 μl
Outlet 2	0	4	8 μl

In the conductivity experiments, conductivity was measured in the output solutions (a mixture of 1:1 glycosil: PBS and DI water flown into the chip) mixed with 12.5% DI water.

A mapping of these conductivity values to what would be the percent mixing are shown in Figure 5.5.

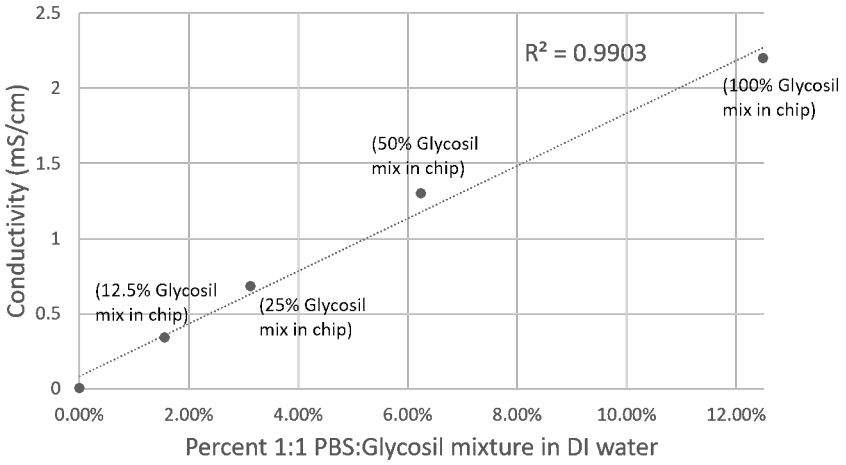

Figure 5.5: Conductivity curve for 1:1 glycosil:PBS mix in DI water. As experimental outputs were in small volume, they were mixed with DI water at a ratio of 12.5% to produce larger volumes for conductivity reading. The numbers in parentheses represent the percent of glycosil mix that would correspond with the above conductivity mapping. As the other solution in the chip was DI water, the percent DI water in a chip output solution can also be calculated using this graph.

Using this linear regression, the following equation was developed to correlate percent mixing in the chip with measured conductivity of the 12.5% solution:

$$Fraction\ glycosil\ mix\ in\ chip\ output = (Conductivity\ [mS/cm] - 0.0852)/2.186 \quad (5.2)$$

The conductivity of each of the outlets is shown in Table 5.2. The conductivity of DI water is 4 $\mu S/cm$, whereas the conductivity of the 1:1 Glycosil-PBS mixture is 16.8 mS/cm.

Some variability exists in the output populations, as would be expected, with some degree of flow instability in the chip. This could be improved through flow rate optimization to improve inertial flow.

Table 5.2: Mixing percentage for output buffers

12.5% Output Mixture in DI water	Outlet 1	Outlet 2
Trial 1: Chip 1	1.46 mS/cm (63% glycosil mix)	0.33 mS/cm (11% glycosil mix)
Trial 2: Chip 1	1.71 mS/cm (74% glycosil mix)	0.46 mS/cm (17% glycosil mix)
Trial 3: Chip 2	1.72mS/cm (75% glycosil mix)	0.68 mS/cm (27% glycosil mix)
Trial 4: Chip 2	2.2 mS/cm (97% glycosil mix)	1.24 mS/cm (53% glycosil mix)

5.6 Discussion

This device could be used in the future as part of an integrated system for personalized tumor diagnostics, in which each subpopulation in a patient's biopsy is separated by their dielectric signature. Following separation, these subpopulations can be embedded in hydrogel to assess proliferation capacity, aggressiveness, and sensitivity to a panel of chemotherapeutics. This can allow for a more combinatorial approach for chemotherapy selection, where information on cell aggressiveness, growth rate, and response to chemotherapies can be assessed simultaneously. Hyaluronic acid hydrogels have begun to be characterized as an in vivo material [112], and could provide a unique cellular environment compared to collagen.

In the future, we will also continue using this chip to gather data on the correlation between specific trapping frequencies and regular phenotypic information. We have observed in previous experiments that lower trapping frequency within a cancerous cell type tends to correlate with metastatic capacity, which we hypothesize is due to changes in the structure of the cell membrane before migration. These changes can be observed in the number and form of pseudopodia and in the dysregulation of cell morphology[113] Current DEP theory does

not account for such structural and morphological changes[99], and with a large database of this information, as well as information on treatment resistance and malignancy, we hope to solve the problem of identifying which cellular properties correlate with specific bioelectrical phenotypes and frequency-dependent states.

5.7 Conclusions

This work showcases the initial designs and testing for an integrated cell characterization system that in the future may allow separation of cells by bioelectrical phenotype and provide a platform for integrated study of their morphology, growth, and response to biochemical triggers. We hope that this can be used to revolutionize chemotherapy selection, as we hypothesize that in tumor cells, the migratory ability of the cells determines probability of trapping at a certain frequency. We hope that a combinatorial approach to chemotherapy selection using this method will improve outcomes.

Chapter 6

Conclusions

This work has showcased a unique application of dielectrophoretic technology in the form of using contactless dielectrophoresis to separate highly similar cells. Late stage mouse ovarian surface epithelial (MOSE) cells were enriched from early stage MOSE cells by using new cell-size-post chips, and optimizing parameter variation in flow rate, voltage and applied frequency. This allowed separation of highly similar cells from the same cell line with different degrees of malignancy.

A computer algorithm was developed to speed up the processing of data sets from contactless dielectrophoresis. Rather than analyzing batches off-chip, a video of cells flowing through the chip can be taken and analyzed for trapped vs. moving cells. This allows for rapid cell characterization: in one experiment, analysis can be performed on a cell population at many voltages, frequencies, and flow rates.

In order to use contactless dielectrophoresis as a method of cell separation for tumor subpopulations, the biophysical parameters that cause separation will need to continue to be validated, and an on-chip analysis method for the downstream populations needs to be developed. We envision both of these to be facilitated by the use of a downstream concentrator that moves cells from DEP buffer into uncured hydrogel, followed by a serpentine where the subpopulations can cure in hydrogel and be multiplexed with an array of chemotherapeutic

drugs. This, in conjunction with an algorithm to take these data and analyze the subpopulations' relative fitness could be developed into a tool for oncologists to use, if further development is continued.

The development and testing of the concentrator was provided in Chapter 5. The downstream serpentine and computer algorithm are in the process of development. Designs for these are given in the upcoming sections. Further work on these downstream system components combined with characterization of many subpopulations as a validation step, could lead to this device becoming of high clinical utility for optimizing treatment regimens.

One particular benefit of this technique over other single-cell or other tumor characterization methods is that by separating cells by frequency, one gains knowledge about those cells' biophysical properties in addition to their response to treatment, growth rate, and invasiveness. This provides an additional parameter that can be tuned and understood with further study.

6.1 Serpentine Development

Downstream of the concentrator presented in Chapter 5, we are developing a serpentine channel separated from a panel of chemotherapies or small diffusible molecules, separated by a membrane with 0.3 μm pores. An image of this is shown in Figure 6.1. Once cells are flown into the serpentine and the gel is cured, chemotherapies can be diffused across the membrane with media to test each subpopulation against an array of therapies. Initial work on this has focused on changing the bonding parameters to ensure a seal between the PDMS and the membrane, changing serpentine channel sizes to minimize the pressure differential across the chip while maintaining separate populations in the device. Testing

of this device design will continue. Alternative techniques could include microfluidic valve systems to multiplex cell batches into separate wells [114, 115, 116], or mechanically moving output tubing into a 96 well plate rather than relying on fluidic methods.

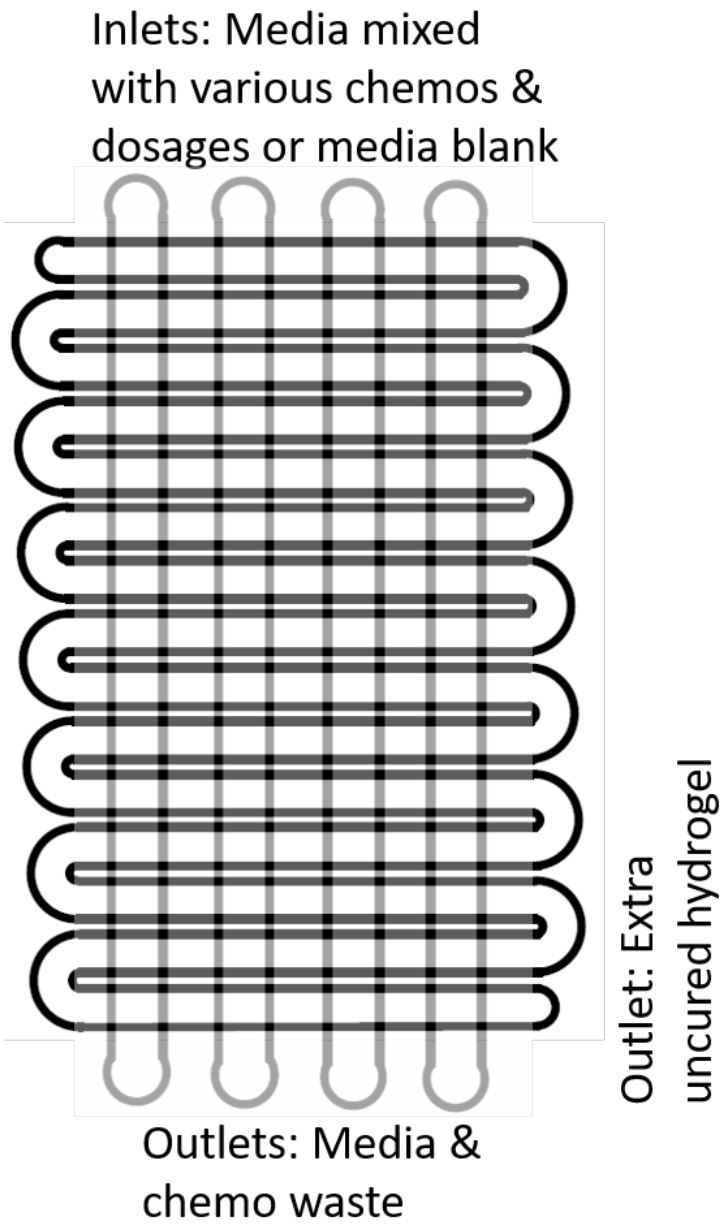

Figure 6.1: Serpentine culture chamber for cell subpopulations.

6.2 Chemotherapy Efficiency Model using output data from cDEP and downstream serpentine

Many sophisticated mathematical models for tumor growth have been developed over the years [117, 118, 119, 120, 121, 122, 123, 124, 125, 126]. However, there is often a disconnect between model development and the translation of this information back into the clinic. We hypothesize that by using data obtained off the dielectrophoresis microdevice such as subpopulation morphology, aggressiveness, and response to treatment, we can develop a simple mathematical system that can be optimized to predict chemotherapy outcomes based on data obtained off chip and a model of cell-cell interactions and response to treatment. An example model system that could use data obtained using the chip for all parameters is shown below.

In this model, all numbers are normalized to show general trends that could be shown using the device, but these models do not reflect actual data. These represent a simplified model that could be elaborated for use.

We first develop a set of differential equations for the change in number of cells of subpopulation i in a theoretical tumor:

$$\frac{dP_i}{dt} = r_i P_i(1 - \Sigma P_i) - \epsilon_i P_i X \tag{6.1}$$

For example, in a theoretical tumor with only two subpopulations (one can also imagine a tumor in which all subpopulations are divided into two groups with more or less similar properties), the populations would be P_1 and P_2 and the set of differential equations would be:

$$\frac{dP_1}{dt} = r_1 P_1(1 - P_1 - P_2 - P_3) - \epsilon_1 P_1 X \tag{6.2}$$

$$\frac{dP_2}{dt} = r_2 P_2(1 - P_1 - P_2 - P_3) - \epsilon_2 P_2 X \tag{6.3}$$

$$\frac{dP_3}{dt} = r_3 P_3(1 - P_1 - P_2 - P_3) - \epsilon_3 P_3 X \tag{6.4}$$

Here, ϵ_i is the chemotherapy kill rate for population i, P_i is the number of cells in population i, r_i is the birth rate minus the natural death rate for population i (so net growth over time in absence of chemotherapy) and X is the drug concentration as a piecewise function in time, to account for both dosage and timing.

Due to the piecewise nature of X, this equation becomes very difficult to study from a theoretical point of view, and would require the use of impulse differential equations, a topic covered by Robert Smith? in his dissertation [127]. Fortunately, the use of numerical methods for resolving time-dependent differential equations has become much easier in recent years with the development of MATLAB.

For example, for the initial case scenario (no spatial dependence or evolution in time), one can plot a tumor with 3 phenotypically unique subpopulations. One chemotherapy is applied at a finite dosing period, and the three cell populations respond differently. The parameters are normalized to be unitless. For this model, the normalized parameters are:

	Cell Type 1	Cell Type 2	Cell Type 3
Growth Rate	0.2	0.1	0.05
Treatment Effectiveness	0.1	0.04	0.02

Using the MATLAB codes provided, this can be written for an arbitrary number of cell subpopulations. Using this system, we could potentially predict many different treatment outcomes. Randomizing this model allows one to take into account stochastic variability in growth, a first-order approximation for spatial dependence. We intend to expand this model

to account for cellular evolution and take data from our device.

In addition, the growth model can be modeled as Gompertzian growth, a more accurate representation of tumor growth which takes into account fractal-like boundaries rather than as a logistic curve. [102, 128]

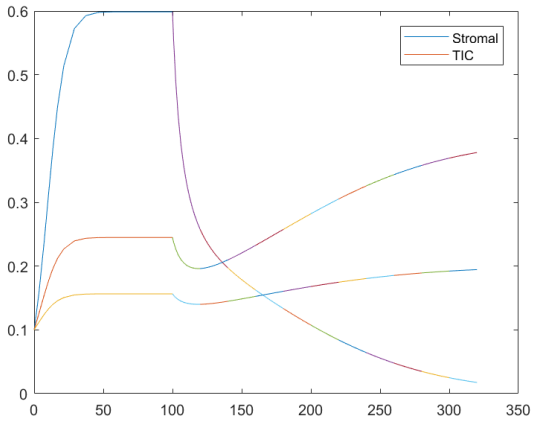

Figure 6.2: Theoretical model of a system of 3 subpopulations undergoing continuous treatment after an initial growth period, with normalized parameters.

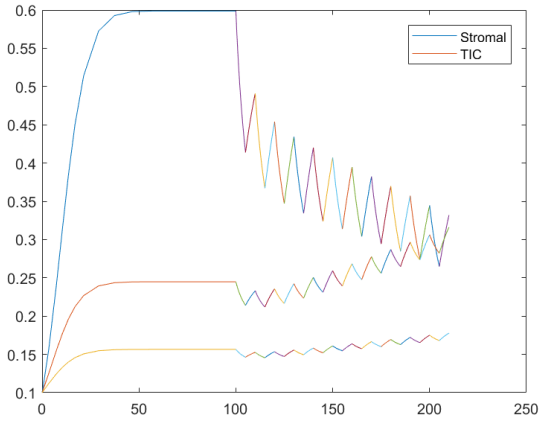

Figure 6.3: Theoretical model of a system of 3 subpopulations undergoing periodic treatment (i=10) after an initial growth period, with normalized parameters.

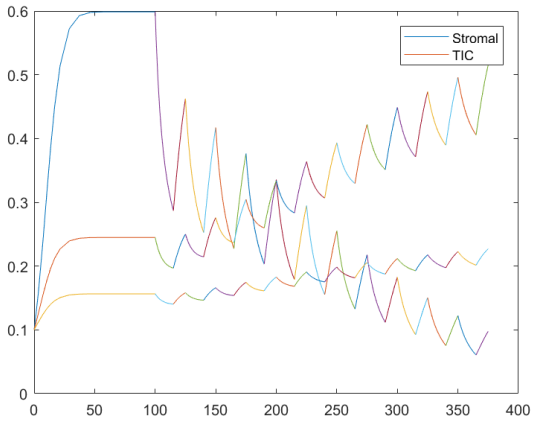

Figure 6.4: Theoretical model of a system of 3 subpopulations undergoing continuous treatment (i=25) after an initial growth period, with normalized parameters.

This model as it is has several limitations. One is that each subpopulation in the model is static in time, whereas we expect new subpopulations to emerge at each division step in a real tumor. Several improvements to this model could also be made, by allowing it to solve for an arbitrary number of cell types, create self generating new cell types as a form of evolution, and by improving the stochasticity of the model to account for spatial interaction between cells and the microenvironment.

6.3 Future Perspectives

In the future, we hope that the combination of contactless dielectrophoresis for cell separation with downstream analysis will provide a powerful tool that can be used to biophysically type cell subpopulations and correlate response to chemotherapy with cell aggressiveness to optimize chemotherapy selection to prevent resistance and recurrence. This will require validation of the technique with many cell types, and we hope that this device development can help with both validation and the final development of a tool to perform this typing in

an integrated manner.

Bibliography

[1] Piyush B Gupta, Christine M Fillmore, Guozhi Jiang, Sagi D Shapira, Kai Tao, Charlotte Kuperwasser, and Eric S Lander. Stochastic state transitions give rise to phenotypic equilibrium in populations of cancer cells. *Cell*, 146(4):633–44, aug 2011.

[2] Samuel D. Rutledge, Temple A. Douglas, Joshua M. Nicholson, Maria Vila-Casadesús, Courtney L. Kantzler, Darawalee Wangsa, Monika Barroso-Vilares, Shiv D. Kale, Elsa Logarinho, and Daniela Cimini. Selective advantage of trisomic human cells cultured in non-standard conditions. *Scientific Reports*, 6(February):22828, 2016.

[3] John J Kim and Ian F Tannock. Repopulation of cancer cells during therapy: an important cause of treatment failure. *Nature reviews. Cancer*, 5(7):516–25, jul 2005.

[4] Bin-Bing S Zhou, Haiying Zhang, Marc Damelin, Kenneth G Geles, Justin C Grindley, and Peter B Dirks. Tumour-initiating cells: challenges and opportunities for anticancer drug discovery. *Nature reviews. Drug discovery*, 8(10):806–23, oct 2009.

[5] John M L Ebos, Christina R Lee, William Cruz-Munoz, Georg a Bjarnason, James G Christensen, and Robert S Kerbel. Accelerated metastasis after short-term treatment with a potent inhibitor of tumor angiogenesis. *Cancer cell*, 15(3):232–9, mar 2009.

[6] Hiroaki Kitano. Tumour tactics. *Nature*, 426:125, 2003.

[7] Samuel D Rutledge and Daniela Cimini. Consequences of aneuploidy in sickness and in health. *Current Opinion in Cell Biology*, 40:41–46, 2016.

[8] Isaiah J Fidler. Critical determinants of metastasis. *Seminars in cancer biology*, 12(2):89–96, apr 2002.

[9] Temple Anne Douglas, Jaka Cemazar, Nikita Balani, Daniel C Sweeney, Eva M Schmelz, and Rafael V Davalos. A feasibility study for enrichment of highly aggressive cancer subpopulations by their biophysical properties via dielectrophoresis. *Electrophoresis*, 38:1507–1514, 2017.

[10] Alireza Salmanzadeh, Elizabeth S Elvington, Paul C Roberts, Eva M Schmelz, and Rafael V Davalos. Sphingolipid metabolites modulate dielectric characteristics of cells in a mouse ovarian cancer progression model. *Integrative biology : quantitative biosciences from nano to macro*, 5(6):843–52, jun 2013.

[11] Amy L Creekmore, William T Silkworth, Daniela Cimini, Roderick V Jensen, Paul C Roberts, and Eva M Schmelz. Changes in gene expression and cellular architecture in an ovarian cancer progression model. *PloS one*, 6(3):e17676, jan 2011.

[12] Jaka Čemažar, Temple A. Douglas, Eva M. Schmelz, and Rafael V. Davalos. Enhanced contactless dielectrophoresis enrichment and isolation platform via cell-scale microstructures. *Biomicrofluidics*, 10(1):014109, 2016.

[13] Herbert Pohl. *Dielectrophoresis: The Behavior of Neutral Matter in Nonuniform Electric Fields (Cambridge Monographs on Physics)*. 1978.

[14] Shabnam A. Faraghat, Kai F. Hoettges, Max K. Steinbach, Daan R. van der Veen, William J. Brackenbury, Erin A. Henslee, Fatima H. Labeed, and Michael P. Hughes. High-throughput, low-loss, low-cost, and label-free cell separation using electrophysiology-activated cell enrichment. *Proceedings of the National Academy of Sciences*, 114(18):4591–4596, 2017.

[15] W A Bonner, H R Hulett, R G Sweet, and L A Herzenberg. Fluorescence Activated Cell Sorting Microfluidic-chip platform for cell sorting Fluorescence Activated Cell Sorting *. *AIP Review of Scientific Instruments*, 43(3):404–409, 1972.

[16] Giulia Bertolini, Luca Roz, Paola Perego, Monica Tortoreto, Enrico Fontanella, Laura Gatti, Graziella Pratesi, Alessandra Fabbri, Francesca Andriani, Stella Tinelli, Elena Roz, Roberto Caserini, Salvatore Lo Vullo, Tiziana Camerini, Luigi Mariani, Domenico Delia, Elisa Calabrò, Ugo Pastorino, and Gabriella Sozzi. Highly tumorigenic lung cancer CD133+ cells display stem-like features and are spared by cisplatin treatment. *PNAS*, 106(38):16281–16286, 2009.

[17] Ping Hu, Wenhua Zhang, Hongbo Xin, and Glenn Deng. Single Cell Isolation and Analysis. *Frontiers in Cell and Developmental Biology*, 4(October):1–12, 2016.

[18] Gerald Burgstaller, Bettina Oehrle, Ina Koch, Michael Lindner, and Oliver Eickelberg. Multiplex Profiling of Cellular Invasion in 3D Cell Culture Models. *PLoS ONE*, 8(5):1–9, 2013.

[19] Hyun-Ho Greco Song, Kyung Min Park, and Sharon Gerecht. Hydrogels to Model 3D in vitro Microenvironment of Tumor Vascularization. *Adv Drug Deliv Rev*, 15(0):19–29, 2014.

[20] Yubao Huang, Luqing Tong, Li Yi, Chen Zhang, Long Hai, Tao Li, Shengping Yu, Wei Wang, Zhennan Tao, Haiwen Ma, Peidong Liu, Yang Xie, and Xuejun Yang. Three-dimensional hydrogel is suitable for targeted investigation of amoeboid migration of glioma cells. *Molecular Medicine Reports*, 17(1):250–256, 2018.

[21] Xuanqi Zhang, Lingjun Li, and Chunxiong Luo. Gel integration for microfluidic applications. *Lab Chip*, 16(10):1757–1776, 2016.

[22] Ronald Pethig, Anoop Menachery, Steve Pells, and Paul De Sousa. Dielectrophoresis : A Review of Applications for Stem Cell Research. *Journal of BIomedicine and Biotechnology*, 2010.

[23] Ronald Pethig. Dielectrophoresis: An assessment of its potential to aid the research and practice of drug discovery and delivery. *Advanced Drug Delivery Reviews*, 65(11-12):1589–1599, 2013.

[24] Paul V. Jones, Sarah J R Staton, and Mark a. Hayes. Blood cell capture in a sawtooth dielectrophoretic microchannel. *Analytical and Bioanalytical Chemistry*, 401(7):2103–2111, 2011.

[25] Peter RC Gascoyne and Jody Vykoukal. Particle separation by dielectrophoresis. *Electrophoresis*, 23(13):1973–1983, 2002.

[26] Alireza Salmanzadeh, Lina Romero, Hadi Shafiee, Roberto C Gallo-villanueva, Mark A Stremler, Scott D Cramer, and Rafael V Davalos. Isolation of prostate tumor initiating cells (TICs) through their dielectrophoretic signature. *Lab on a Chip*, 12:182–189, 2012.

[27] R Guirguis, I Margulies, G Taraboletti, E Schiffmann, and L Liotta. Cytokine-induced pseudopodial protrusion is coupled to tumour cell migration. *Nature*, 329(6136):261–263, 1987.

[28] Peter R C Gascoyne and Sangjo Shim. Isolation of circulating tumor cells by dielectrophoresis. *Cancers*, 6(1):545–579, 2014.

[29] Bahige G. Abdallah, Tzu Chiao Chao, Christopher Kupitz, Petra Fromme, and Alexandra Ros. Dielectrophoretic sorting of membrane protein nanocrystals. *ACS Nano*, 7(10):9129–9137, 2013.

[30] Hadi Shafiee, Michael B Sano, Erin a Henslee, John L Caldwell, and Rafael V Davalos. Selective isolation of live/dead cells using contactless dielectrophoresis (cDEP). *Lab on a chip*, 10(4):438–445, 2010.

[31] Alireza Salmanzadeh and Rafael V. Davalos. Isolation of Rare Cells through their Dielectrophoretic Signature. *Journal of Membrane Science & Technology*, 3(1):1–4, 2013.

[32] Rodrigo Martinez-Duarte, Fernanda Camacho-Alanis, Philippe Renaud, and Alexandra Ros. Dielectrophoresis of lambda-DNA using 3D carbon electrodes. *Electrophoresis*, 34(7):1113–1122, 2013.

[33] Hector Moncada-Hernandez, Eliot Nagler, and Adrienne R. Minerick. Theoretical and experimental examination of particle-particle interaction effects on induced dipole moments and dielectrophoretic responses of multiple particle chains. *Electrophoresis*, 35(12-13):1803–1813, 2014.

[34] Q. Hu, R. P. Joshi, and A. Beskok. Model study of electroporation effects on the dielectrophoretic response of spheroidal cells. *Journal of Applied Physics*, 106(2), 2009.

[35] Yan Wang, Fei Du, Georg R Pesch, Jan Köser, Michael Baune, and Jorg Thöming. Microparticle trajectories in a high-throughput channel for contact-free fractionation by dielectrophoresis. *Chemical Engineering Science*, (July), 2016.

[36] Y Huang, X B Wang, F F Becker, and P R Gascoyne. Introducing dielectrophoresis as a new force field for field-flow fractionation. *Biophysical journal*, 73(August):1118–1129, 1997.

[37] Xujing Wang, Frederick F. Becker, and Peter R.C. Gascoyne. Membrane dielectric

changes indicate induced apoptosis in HL-60 cells more sensitively than surface phosphatidylserine expression or DNA fragmentation. *Biochimica et Biophysica Acta - Biomembranes*, 1564(2):412–420, 2002.

[38] Hadi Shafiee, John L. Caldwell, Michael B. Sano, and Rafael V. Davalos. Contactless dielectrophoresis: A new technique for cell manipulation. *Biomedical Microdevices*, 11(5):997–1006, 2009.

[39] Nicholas Mavrogiannis, Mitchell Desmond, and Zachary R. Gagnon. Fluidic dielectrophoresis: The polarization and displacement of electrical liquid interfaces. *Electrophoresis*, pages n/a–n/a, 2015.

[40] Zachary R. Gagnon. Cellular dielectrophoresis: Applications to the characterization, manipulation, separation and patterning of cells. *Electrophoresis*, 32(18):2466–2487, 2011.

[41] R Pethig and D B Kell. The passive electrical properties of biological systems: their significance in physiology, biophysics and biotechnology. *Physics in medicine and biology*, 32(8):933–970, 1987.

[42] Ka Lok Chan, Peter R C Gascoyne, Frederick F. Becker, and Ronald Pethig. Electrorotation of liposomes: Verification of dielectric multi-shell model for cells. *Biochimica et Biophysica Acta - Lipids and Lipid Metabolism*, 1349(2):182–196, 1997.

[43] Jaka Cemazar, Damijan Miklavcic, and Tadej Kotnik. Microfluidic devices for manipulation, modification and characterization of biological cells in electric fields–a review. *Informacije MIDEM: Journal of Microelectronics, electronic components and materials*, 43(3):143–161, 2013.

[44] H Rezaei Nejad, Ovee Z Chowdhury, Matthew D Buat, and Mina Hoorfar. Characterization of the geometry of negative dielectrophoresis traps for particle immobilization in digital microfluidic platforms. *Lab on a chip*, 13(9):1823–30, 2013.

[45] Srinivasu Valagerahally Puttaswamy, Shilpa Sivashankar, Rong Jhe Chen, Chung Kuang Chin, Hwan You Chang, and Cheng Hsien Liu. Enhanced cell viability and cell adhesion using low conductivity medium for negative dielectrophoretic cell patterning. *Biotechnology Journal*, 5(10):1005–1015, 2010.

[46] Kaela M. Leonard and Adrienne R. Minerick. Explorations of ABO-Rh antigen expressions on erythrocyte dielectrophoresis: Changes in cross-over frequency. *Electrophoresis*, 32(18):2512–2522, 2011.

[47] Michael B. Sano, Alireza Salmanzadeh, and Rafael V. Davalos. Multilayer contactless dielectrophoresis: Theoretical considerations. *Electrophoresis*, 33(13):1938–1946, 2012.

[48] T B Jones. *Electromechanics of particles*. Cambridge University Press, Cambridge ;, digitally edition, 2005.

[49] Blanca H. Lapizco-Encinas, Sandra Ozuna-Chacón, and Marco Rito-Palomares. Protein manipulation with insulator-based dielectrophoresis and direct current electric fields. *Journal of Chromatography A*, 1206(1):45–51, oct 2008.

[50] Ronald Pethig. Review—Where Is Dielectrophoresis (DEP) Going? *Journal of The Electrochemical Society*, 164(5):B3049–B3055, 2017.

[51] M. A. Saucedo-Espinosa and B. H. Lapizco-Encinas. Design of insulator-based dielectrophoretic devices: Effect of insulator posts characteristics. *Journal of Chromatography A*, 1422:325–333, 2015.

[52] Fernanda Camacho-Alanis, Lin Gan, and Alexandra Ros. Transitioning streaming to trapping in DC insulator-based dielectrophoresis for biomolecules. *Sensors and Actuators B: Chemical*, 173:668–675, 2012.

[53] Zi-ming Zhao, Bixiao Zhao, Yalai Bai, Atila Iamarino, Stephen G Gaffney, Joseph Schlessinger, Richard P Lifton, David L Rim, and Jeffrey P Townsend. Early and multiple origins of metastatic lineages within primary tumors. *PNAS*, 113(8):2140–2145, 2016.

[54] Dirk Drasdo and Stefan Höhme. A single-cell-based model of tumor growth in vitro: monolayers and spheroids. *Physical biology*, 2(3):133–47, sep 2005.

[55] Marco Gerlinger, Andrew J Rowan, Stuart Horswell, James Larkin, David Endesfelder, Eva Gronroos, Pierre Martinez, Nicholas Matthews, Aengus Stewart, Patrick Tarpey, Ignacio Varela, Benjamin Phillimore, Sharmin Begum, Neil Q McDonald, Adam Butler, David Jones, Keiran Raine, Calli Latimer, Claudio R Santos, Mahrokh Nohadani, Aron C Eklund, Bradley Spencer-Dene, Graham Clark, Lisa Pickering, Gordon Stamp, Martin Gore, Zoltan Szallasi, Julian Downward, P Andrew Futreal, and Charles Swanton. Intratumoral Heterogeneity and Branched Evolution Revealed by Multiregion Sequencing. *New England Journal of Medicine*, 366(10):883–892, 2012.

[56] Sally M Dewhurst, Nicholas McGranahan, Rebecca a Burrell, Andrew J Rowan, Eva Grönroos, David Endesfelder, Tejal Joshi, Dmitri Mouradov, Peter Gibbs, Robyn L Ward, Nicholas J Hawkins, Zoltan Szallasi, Oliver M Sieber, and Charles Swanton. Tolerance of whole-genome doubling propagates chromosomal instability and accelerates cancer genome evolution. *Cancer discovery*, 4(2):175–185, feb 2014.

[57] Dominik Wodarz. Somatic Evolution of Cells and the Development of Cancer. *Biological Theory*, 1(2):119–122, 2006.

[58] Ivana Bozic, Benjamin Allen, and Martin a. Nowak. Dynamics of targeted cancer therapy. *Trends in Molecular Medicine*, 18(6):311–316, 2012.

[59] Qiucen Zhang and Robert H. Austin. Physics of Cancer: The Impact of Heterogeneity. *Annual Review of Condensed Matter Physics*, 3(1):363–382, mar 2012.

[60] Navid Kashaninejad, Mohammad Reza Nikmaneshi, Hajar Moghadas, Amir Kiyoumarsi Oskouei, Milad Rismanian, Maryam Barisam, Mohammad Said Saidi, and Bahar Firoozabadi. Organ-Tumor-on-a-Chip for Chemosensitivity Assay : A Critical Review. *micromachines*, 7(130), 2016.

[61] L Galluzzi, L Senovilla, I Vitale, J Michels, I Martins, O Kepp, M Castedo, and G Kroemer. Molecular mechanisms of cisplatin resistance. *Oncogene*, 31(15):1869–83, apr 2012.

[62] Robert A Gatenby, Ariosto S Silva, Robert J Gillies, and B Roy Frieden. Mathematical Oncology: Adaptive Therapy. *Cancer Res*, 69(11):4894–4903, 2009.

[63] Zachary R. Gagnon. Cellular dielectrophoresis: Applications to the characterization, manipulation, separation and patterning of cells. *Electrophoresis*, 32(18):2466–2487, 2011.

[64] Mario A. Saucedo-Espinosa, Alexandra Lalonde, Aytug Gencoglu, Maria F. Romero-Creel, Jay R. Dolas, and Blanca H. Lapizco-Encinas. Dielectrophoretic manipulation of particle mixtures employing asymmetric insulating posts. *Electrophoresis*, 37(2):282–290, 2016.

[65] Blanca H Lapizco-Encinas, Blake a Simmons, Eric B Cummings, and Yolanda Fintschenko. Insulator-based dielectrophoresis for the selective concentration and separation of live bacteria in water. *Electrophoresis*, 25(10-11):1695–1704, 2004.

[66] Chia-Fu Chou, Jonas O Tegenfeldt, Olgica Bakajin, Shirley S Chan, Edward C Cox, Nicholas Darnton, Thomas Duke, and Robert H Austin. Electrodeless Dielectrophoresis of Single- and Double-Stranded DNA. *Biophysical Journal*, 83(October):2170–2179, 2002.

[67] Eric B Cummings and Anup K Singh. Dielectrophoresis in Microchips Containing Arrays of Insulating Posts : Theoretical and Experimental Results. *Anal. Chem.*, 75(18):4724–4731, 2003.

[68] Mario Cabodi, Yi-Fan Chen, Stephen W P Turner, Harold G Craighead, and Robert H Austin. Continuous separation of biomolecules by the laterally asymmetric diffusion array with out-of-plane sample injection. *Electrophoresis*, 23:3496–3503, 2002.

[69] Brian J Kirby. *Micro- and nanoscale fluid mechanics : transport in microfluidic devices*. Cambridge University Press, New York.

[70] Courtney a Cohen, Amanda a Shea, C Lynn Heffron, Eva M Schmelz, and Paul C Roberts. Intra-abdominal fat depots represent distinct immunomodulatory microenvironments: a murine model. *PloS one*, 8(6):e66477, jan 2013.

[71] Courtney A Cohen, Amanda A Shea, C Lynn Heffron, Eva M Schmelz, and Paul C Roberts. The Parity-Associated Microenvironmental Niche in the Omental Fat Band Is Refractory to Ovarian Cancer Metastasis. *Cancer Prev Res*, 6(11), 2013.

[72] Ronald Pethig. Review—Where Is Dielectrophoresis (DEP) Going? *Journal of The Electrochemical Society*, 164(5):B3049–B3055, 2017.

[73] Thea D. Tlsty and Lisa M. Coussens. Tumor Stroma and Regulation of Cancer Development. *Annual Review of Pathology: Mechanisms of Disease*, 1(1):119–150, 2006.

[74] Douglas Hanahan and Lisa M Coussens. Accessories to the crime: functions of cells recruited to the tumor microenvironment. *Cancer cell*, 21(3):309–22, mar 2012.

[75] Douglas Hanahan and Robert a Weinberg. Hallmarks of cancer: the next generation. *Cell*, 144(5):646–74, mar 2011.

[76] Shweta Aras and M. Raza Zaidi. TAMeless traitors: Macrophages in cancer progression and metastasis. *British Journal of Cancer*, 117(11):1583–1591, 2017.

[77] E. Y. Lin and J. W. Pollard. Role of infiltrated leucocytes in tumour growth and spread. *British Journal of Cancer*, 90(11):2053–2058, 2004.

[78] Df Quail and Ja Joyce. Microenvironmental regulation of tumor progression and metastasis. *Nature medicine*, 19(11):1423–1437, 2013.

[79] Mark Spaw, Shrikant Anant, and Sufi Mary Thomas. Stromal contributions to the carcinogenic process. *Molecular Carcinogenesis*, 56(4):1199–1213, 2017.

[80] J. Nilsson, M. Evander, B. Hammarström, and T. Laurell. Review of cell and particle trapping in microfluidic systems. *Analytica Chimica Acta*, 649(2):141–157, 2009.

[81] Donald Wlodkowic, Shannon Faley, Michele Zagnoni, John P Wikswo, and Jonathan M Cooper. Microfluidic Single Cell Array Cytometry for the Analysis of Tumour Apoptosis. *Anal. Chem.*, 81(13):5517–5523, 2009.

[82] Jérôme Mutterer and Wayne Rasband. ImageJ Macro Language Programmer's Reference Guide v1.46d. pages 1–45, 2012.

[83] Plugins, https://imagej.nih.gov/ij/plugins/index.html .

[84] Mehmet Sezgin and Bulent Sankur. Survey over image thresholding techniques and quantitative performance evaluation. *Journal of Electronic Imaging*, 13(1):146–165, 2004.

[85] Liang-Kai Huang and Mao-Jiun J. Wang. Image Thresholding by Minimizing the Measures of Fuzziness. *Pattern Recognition*, 28(1):41–51, 1995.

[86] Judith M S Prewitt and Mortimer L. Mendelsohn. The Analysis of Cell Images. *Annals of the New York Academy of Sciences*, 128(3):1035–1053, 1966.

[87] TW Ridler and S Calvard. Picture Thresholding Using an Interative Selection Method. *IEEE Transactions on Systems, Man, and Cybernetics*, SMC-8(8):630–632, 1978.

[88] C. H. Li and C. K. Lee. Minimum cross entropy thresholding. *Pattern Recognition*, 26(4):617–625, 1993.

[89] Thierry Pun. A new method for grey-level picture thresholding using the entropy of the histogram. *Signal Processing*, 2(3):223–237, jul 1980.

[90] C.A. Glasbey. An Analysis of Histogram-Based Thresholding Algorithms. *CVGIP: Graphical Models and Image Processing*, 55(6):532–537, nov 1993.

[91] J. Kittler and J. Illingworth. Minimum error thresholding. *Pattern Recognition*, 19(1):41–47, jan 1986.

[92] Otsu. A Threshold Selection Method from Gray-Level Histograms. *IEEE Transactions on Systems, Man, and Cybernetics*, 9:62–66, 2018.

[93] Jui-Cheng Yen, Fu-Juay Chang, and Shyang Chang. A new criterion for automatic multilevel thresholding. *IEEE Transactions on Image Processing*, 4(3):370–378, 1995.

[94] GW Zack, WE Rogers, and SA Latt. Automatic Measurement of Sister Chromatid Exchange Frequency. *Journal of Histochemistry and Cytochemistry*, 25(7):741–753, 1977.

[95] A.G. Shanbhag. Utilization of Information Measure as a Means of Image Thresholding. *CVGIP: Graphical Models and Image Processing*, 56(5):414–419, sep 1994.

[96] J.N. Kapur, P.K. Sahoo, and A.K.C. Wong. A new method for gray-level picture thresholding using the entropy of the histogram. *Computer Vision, Graphics, and Image Processing*, 29(3):273–285, mar 1985.

[97] Luc Vincent and Pierre Soille. Watersheds in Digital Spaces: An Efficient Algorithm Based on Immersion Simulations, 1991.

[98] N G Green and H Morgan. Separation of submicrometre particles using a combination of dielectrophoretic and electrohydrodynamic forces. *Journal of Physics D: Applied Physics*, 31(7):L25–L30, 1999.

[99] Hossein Nili and Nicolas G. Green. Higher-order dielectrophoresis of nonspherical particles. *Physical Review E - Statistical, Nonlinear, and Soft Matter Physics*, 89(6):1–11, 2014.

[100] H. Nili, T. Sun, and N. G. Green. Higher order dielectrophoretic force characterisation of non-spherical particles. *Journal of Physics: Conference Series*, 301(1):1–5, 2011.

[101] Hywel Morgan and Nicolas G. Green. Dielectrophoretic manipulation of rod-shaped viral particles. *Journal of Electrostatics*, 42(3):279–293, 1997.

[102] Mel Greaves and Carlo C Maley. Clonal evolution in cancer. *Nature*, 481(7381):306–13, jan 2012.

[103] Peter Duesberg, Daniele Mandrioli, Amanda McCormack, and Joshua M. Nicholson. Is carcinogenesis a form of speciation? *Cell Cycle*, 10(13):2100–2114, 2011.

[104] Tracy a Denison and You Han Bae. Tumor heterogeneity and its implication for drug delivery. *Journal of controlled release : official journal of the Controlled Release Society*, 164(2):187–91, 2012.

[105] Andrea Weiss, Xianting Ding, Judy R van Beijnum, Ieong Wong, Tse J Wong, Robert H Berndsen, Olivier Dormond, Marchien Dallinga, Li Shen, Reinier O Schlingemann, Roberto Pili, Chih-Ming Ho, Paul J Dyson, Hubert van den Bergh, Arjan W Griffioen, and Patrycja Nowak-Sliwinska. Rapid optimization of drug combinations for the optimal angiostatic treatment of cancer. *Angiogenesis*, pages 233–244, 2015.

[106] Amy Wu. *Emergence of chemotherapy resistance in cancer : microenvironments , genomics , and game theory approaches*. PhD thesis, 2015.

[107] Mohit Kumar Jolly, Satyendra C. Tripathi, Dongya Jia, Steven M. Mooney, Muge Celiktas, Samir M. Hanash, Sendurai A. Mani, Kenneth J. Pienta, Eshel Ben-Jacob, and Herbert Levine. Stability of the hybrid epithelial/mesenchymal phenotype. *Oncotarget*, 7(19):27067–27084, 2016.

[108] Valentine Comaills, Lilian Kabeche, Robert Morris, Lee Zou, Daniel A Haber, Shyamala Maheswaran Correspondence, Ré Mi Buisson, Min Yu, Marissa Wells Madden, Joseph A Licausi, Myriam Boukhali, Ken Tajima, Shiwei Pan, Nicola Aceto, Srinjoy Sil, Yu Zheng, Tilak Sundaresan, Toshifumi Yae, Nicole Vincent Jordan, David T Miyamoto, David T Ting, Sridhar Ramaswamy, Wilhelm Haas, and Shyamala Maheswaran. Genomic Instability Is Induced by Persistent Proliferation of Cells Undergoing Epithelial-to- Mesenchymal Transition Genomic Instability Is Induced by Per-

sistent Proliferation of Cells Undergoing Epithelial-to-Mesenchymal Transition. *Cell Reports*, 17(6):2632–2647, 2016.

[109] Maurice N. Collins and Colin Birkinshaw. Physical properties of crosslinked hyaluronic acid hydrogels. *Journal of Materials Science: Materials in Medicine*, 19(11):3335–3343, 2008.

[110] Monica A Serban, Anna Scott, and Glenn D Prestwich. Use of Hyaluronan-Derived Hydrogels for Three-Dimensional Cell Culture and Tumor Xenografts. *Curr Protoc Cell Biol*, September, 2008.

[111] ESI Bio. Glycosil Factsheet. 2014.

[112] Jl Young, J Tuler, R Braden, P Schüp-Magoffin, J Schaefer, K Kretchmer, Kl Christman, and Aj Engler. In vivo response to dynamic hyaluronic acid hydrogels. *Acta biomaterialia*, 9(7):7151–7157, 2014.

[113] Lance A Liotta, Raouf Guirguis, and Mary Stracke. Review Article: Biology of Melanoma Invasion and Metastasis. *Pigment Cell Research*, 1:5–15, 1987.

[114] Dong Woo Lee, Il Doh, Yoonji Kim, and Young-Ho Cho. Advanced combinational microfluidic multiplexer using multiple levels of control pressures. *Lab Chip*, 13:3658–3662, 2013.

[115] Xiangpeng Li, Jessica C. Brooks, Juan Hu, Katarena I. Ford, and Christopher J. Easley. 3d-templated, fully automated microfluidic input/output multiplexer for endocrine tissue culture and secretion sampling. *Lab Chip*, 17:341–349, 2017.

[116] M Kursad Araz, Augusto M Tentori, and Amy E Herr. Microfluidic Multiplexing in Bioanalyses. *Journal of Laboratory Automation*, 18(5):350–366, 2013.

[117] N. Beerenwinkel, R. F. Schwarz, M. Gerstung, and F. Markowetz. Cancer Evolution: Mathematical Models and Computational Inference. *Systematic Biology*, 64(1):e1–e25, 2015.

[118] Steven A Frank. Somatic evolutionary genomics: mutations during development cause highly variable genetic mosaicism with risk of cancer and neurodegeneration. *Proceedings of the National Academy of Sciences of the United States of America*, 107 Suppl:1725–1730, 2010.

[119] Navid Ghorashian, Sertan Kutal Gökçe, Sam Xun Guo, William Neil Everett, and Adela Ben-Yakar. An Automated Microfluidic Multiplexer for Fast Delivery of C . elegans Populations from Multiwells. *PLOS one*, 8(9):e74480, 2013.

[120] Andrew P Feinberg and Rafael A Irizarry. Evolution in health and medicine Sackler colloquium: Stochastic epigenetic variation as a driving force of development, evolutionary adaptation, and disease. *Proceedings of the National Academy of Sciences of the United States of America*, 107 Suppl:1757–1764, 2010.

[121] Rebecca A Burrell, Nicholas McGranahan, Jiri Bartek, and Charles Swanton. The causes and consequences of genetic heterogeneity in cancer evolution. *Nature*, 501(7467):338–45, 2013.

[122] Ivana Bozic and Martin A Nowak. Unwanted Evolution. *Science*, 342, 2013.

[123] Louis Vermeulen, Edward Morrissey, Maartje Van Der Heijden, Anna M. Nicholson, Andrea Sottoriva, Simon Buczacki, Richard Kemp, Simon Tavaré, and Douglas J. Winton. Defining Stem Cell Dynamics in Models of Intestinal Tumor Initiation. *Science*, 342(6161):995–998, 2013.

[124] Dominik Wodarz. Somatic Evolution of Cells and the Development of Cancer. *Biological Theory*, 1(2):119–122, 2006.

[125] Ivana Bozic, Benjamin Allen, and Martin a. Nowak. Dynamics of targeted cancer therapy. *Trends in Molecular Medicine*, 18(6):311–316, 2012.

[126] Trachette L Jackson and Helen M Byrne. A mathematical model to study the effects of drug resistance and vasculature on the response of solid tumors to chemotherapy. *Mathematical Biosciences*, 164:17–38, 2000.

[127] Robert Smith. IMPULSIVE DIFFERENTIAL EQUATIONS WITH APPLICATIONS TO SELF-CYCLING FERMENTATION. (October), 2001.

[128] ARA Anderson and MAJ Chaplain. Continuous and Discrete Mathematical Models of Tumor-induced Angiogenesis. *Bulletin of Mathematical Biology*, 60:857–900, 1998.

Appendices

Appendix A

ImageJ Macro Code

```
        filepath = getString("Complete Filename with Path", "");
run("Image Sequence...", "open=[filepath] sort use");
pathname = File.getParent(filepath);
filename = File.getName(filepath);

Dialog.create("Image Properties");
Dialog.addCheckbox("Does image stack contain multiple colors?", true);
Dialog.addChoice("Threshold Method:", newArray("Default", "Huang", "Intermodes", "IsoDat
Dialog.show();

color = Dialog.getCheckbox();
threshold_method = Dialog.getChoice();

if(color)
{
run("Split Channels");

selectWindow(filename+" (green)");
run("Make Binary", "method="+threshold_method+" background=Default calculate");
```

```
run("Watershed", "stack");
selectWindow(filename+" (red)");
run("Make Binary", "method="+threshold_method+" background=Default calculate");
run("Watershed", "stack");
selectWindow(filename+" (blue)");
run("Make Binary", "method="+threshold_method+" background=Default calculate");
run("Watershed", "stack");

Dialog.create("Slide Comparison");
Dialog.addString("Number of slides to compare in set?" , 5);
Dialog.show();
number=Dialog.getString();


selectWindow(filename+" (green)");
run("Z Project...", "start=1 stop="+number+" projection=Median");


selectWindow(filename+" (green)");
for (i=1; i<=nSlices-number; i++)
{
nstart=i+1;
nstop=i+number;
run("Z Project...", "start="+nstart+ " stop="+nstop+" projection=Median");
selectWindow("MED_"+filename+" (green)");
run("Add Slice");
```

```
selectWindow("MED_"+filename+" (green)-1");
run("Copy");
selectWindow("MED_"+filename+" (green)");
run("Paste");
selectWindow("MED_"+filename+" (green)-1");
close();
selectWindow(filename+" (green)");
}



selectWindow(filename+" (red)");
run("Z Project...", "start=1 stop="+number+" projection=Median");

selectWindow(filename+" (red)");
for (i=1; i<=nSlices-number; i++)
{
nstart=i+1;
nstop=i+number;
run("Z Project...", "start="+nstart+ " stop="+nstop+" projection=Median");
selectWindow("MED_"+filename+" (red)");
run("Add Slice");
selectWindow("MED_"+filename+" (red)-1");
run("Copy");
selectWindow("MED_"+filename+" (red)");
run("Paste");
```

```
selectWindow("MED_"+filename+" (red)-1");
close();
selectWindow(filename+" (red)");

}

selectWindow(filename+" (blue)");
run("Z Project...", "start=1 stop="+number+" projection=Median");

selectWindow(filename+" (blue)");
for (i=1; i<=nSlices-number; i++)
{
nstart=i+1;
nstop=i+number;
run("Z Project...", "start="+nstart+ " stop="+nstop+" projection=Median");
selectWindow("MED_"+filename+" (blue)");
run("Add Slice");
selectWindow("MED_"+filename+" (blue)-1");
run("Copy");
selectWindow("MED_"+filename+" (blue)");
run("Paste");
selectWindow("MED_"+filename+" (blue)-1");
close();
selectWindow(filename+" (blue)");
}
```

```
selectWindow("MED_"+filename+" (red)");
saveAs("Tiff", filepath+"MED (red)");
selectWindow("MED_"+filename+" (green)");
saveAs("Tiff", filepath+"MED (green)");
selectWindow(filename+" (red)");
saveAs("Tiff", filepath+" (red)");
selectWindow(filename+" (green)");
saveAs("Tiff", filepath+" (green)");
selectWindow("MED_"+filename+" (blue)");
saveAs("Tiff", filepath+"MED (blue)");
selectWindow(filename+" (blue)");
saveAs("Tiff", filepath+" (blue)");

Dialog.create("Analyze Particles");
Dialog.addString("Minimum particle size (pixels)?" , 10);
Dialog.addString("Maximum particle size (pixels)?", "Infinity");
Dialog.addString("Particle circularity minimum?", 0.10);
Dialog.addString("Particle circularity maximum?", 1.00);
Dialog.show();
min_size=Dialog.getString();
max_size=Dialog.getString();
min_circ=Dialog.getString();
max_circ=Dialog.getString();

selectWindow(filename+"MED (red).tif");
setAutoThreshold("Default");
```

```
//run("Threshold...");
setThreshold(129, 255);
setOption("BlackBackground", false);
run("Convert to Mask", "method=Default background=Light");
run("Analyze Particles...", "size="+min_size+"-"+max_size+" circularity="+min_circ+"-"+m
selectWindow("Summary of "+filename+"MED (red).tif");
saveAs("Text", filepath+"Summary of MED (red).xls");


selectWindow(filename+"MED (green).tif");
setAutoThreshold("Default");
//run("Threshold...");
setThreshold(129, 255);
setOption("BlackBackground", false);
run("Convert to Mask", "method=Default background=Light");
run("Analyze Particles...", "size="+min_size+"-"+max_size+" circularity="+min_circ+"-"+m
selectWindow("Summary of "+filename+"MED (green).tif");
saveAs("Text", filepath+"Summary of MED (green).xls");


selectWindow(filename+"MED (blue).tif");
setAutoThreshold("Default");
//run("Threshold...");
setThreshold(129, 255);
setOption("BlackBackground", false);
run("Convert to Mask", "method=Default background=Light");
```

```
run("Analyze Particles...", "size="+min_size+"-"+max_size+" circularity="+min_circ+"-"+m
selectWindow("Summary of "+filename+"MED (blue).tif");
saveAs("Text", filepath+"Summary of MED (blue).xls");


selectWindow(filename+" (red).tif");
run("Analyze Particles...", "size="+min_size+"-"+max_size+" circularity="+min_circ+"-"+m
selectWindow("Summary of "+filename+" (red).tif");
saveAs("Text", filepath+"Summary of (red).xls");


selectWindow(filename+" (green).tif");
run("Analyze Particles...", "size="+min_size+"-"+max_size+" circularity="+min_circ+"-"+m
selectWindow("Summary of "+filename+" (green).tif");
saveAs("Text", filepath+"Summary of (green).xls");


selectWindow(filename+" (blue).tif");
run("Analyze Particles...", "size="+min_size+"-"+max_size+" circularity="+min_circ+"-"+m
selectWindow("Summary of "+filename+" (blue).tif");
saveAs("Text", filepath+"Summary of (blue).xls");


}
```

```
else{

selectWindow(filename);
run("Duplicate...", "title="+filename+"-A duplicate");
run("Make Binary", "method="+threshold_method+" background=Default calculate");
run("Watershed", "stack");

selectWindow(filename);
close();

Dialog.create("Slide Comparison");
Dialog.addString("Number of slides to compare in set?" , 5);
Dialog.show();
number=Dialog.getString();



selectWindow(filename+"-A");
run("Z Project...", "start=1 stop="+number+" projection=Median");



selectWindow(filename+"-A");
for (i=1; i<=nSlices-number; i++)
{
nstart=i+1;
nstop=i+number;
```

```
run("Z Project...", "start="+nstart+ " stop="+nstop+" projection=Median");
selectWindow("MED_"+filename+"-A");
run("Add Slice");
selectWindow("MED_"+filename+"-A-1");
run("Copy");
selectWindow("MED_"+filename+"-A");
run("Paste");
selectWindow("MED_"+filename+"-A-1");
close();
selectWindow(filename+"-A");
}



selectWindow("MED_"+filename+"-A");
saveAs("Tiff", filepath+"-A MED");
selectWindow(filename+"-A");
saveAs("Tiff", filepath+"-A");

Dialog.create("Analyze Particles");
Dialog.addString("Minimum particle size (pixels)?" , 10);
Dialog.addString("Maximum particle size (pixels)?", "Infinity");
Dialog.addString("Particle circularity minimum?", 0.10);
Dialog.addString("Particle circularity maximum?", 1.00);
Dialog.show();
min_size=Dialog.getString();
```

```
max_size=Dialog.getString();
min_circ=Dialog.getString();
max_circ=Dialog.getString();

selectWindow(filename+"-A MED.tif");
setAutoThreshold("Default");
//run("Threshold...");
setThreshold(129, 255);
setOption("BlackBackground", false);
run("Convert to Mask", "method=Default background=Light");
run("Analyze Particles...", "size="+min_size+"-"+max_size+" circularity="+min_circ+"-"+m
selectWindow("Summary of "+filename+"-A MED.tif");
saveAs("Text", filepath+"-A Summary of MED.xls");


selectWindow(filename+"-A.tif");
run("Analyze Particles...", "size="+min_size+"-"+max_size+" circularity="+min_circ+"-"+m
selectWindow("Summary of "+filename+"-A.tif");
saveAs("Text", filepath+"-A Summary.xls");


}
```

Appendix B

ImageJ User Guide

B.1 Program Flow Chart

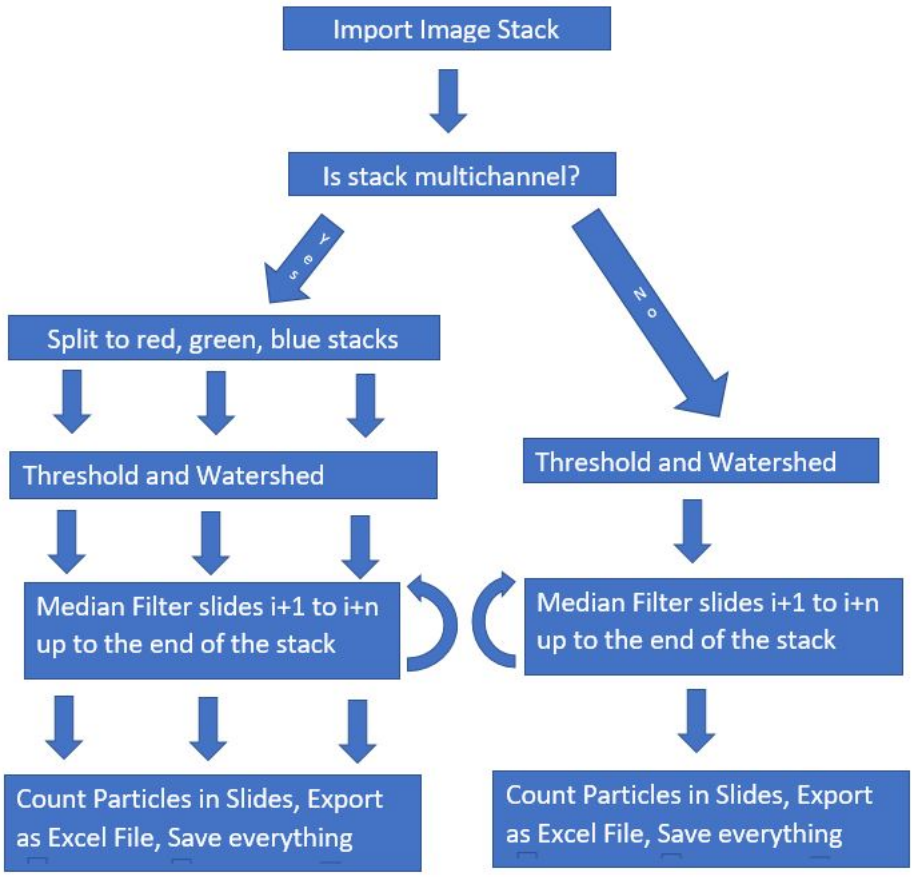

Figure B.1: Flow chart of program function.

B.2 How to Use Macro

- Save the macro somewhere in your computer. In ImageJ, go to FileOpen and open the macro.

- In the macro window, you can either click “Ctrl –R” or go to MacrosRun Macro.

- The macro will ask for the complete filename of the file you want to analyze with path. All images to be sent to a stack need to be in the same folder. Right click on the name of the folder in the directory containing your image stack and click “Copy Address”, then paste this into the filename box. For example, the address input in this case would be:

```
"C:\Users\Temple Anne Douglas\Documents\imagej macro docs\TestCase"
```

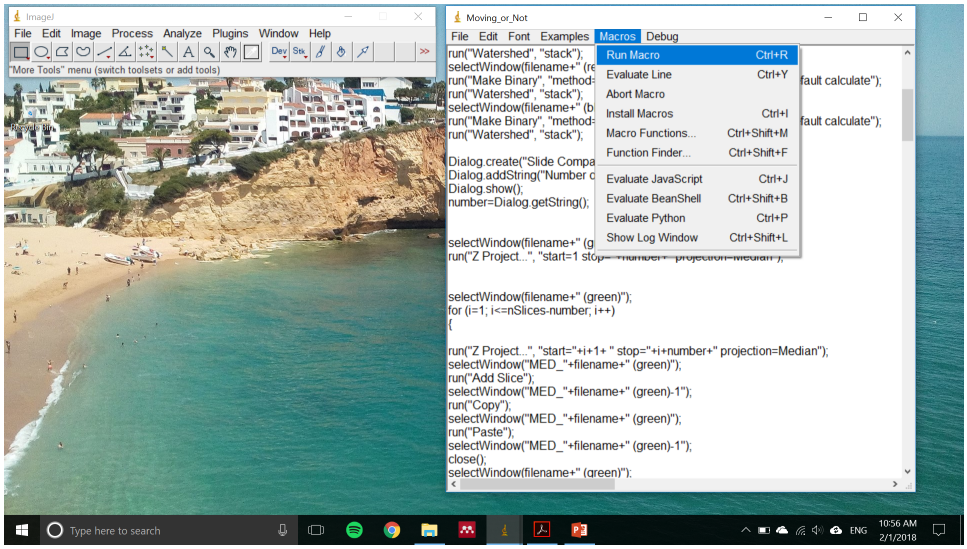

Figure B.2: Macro run command.

- Uncheck the box if you only want to analyze the file in a single color, and the file is not multi-channel. If the file has multiple colors, leave this box checked.

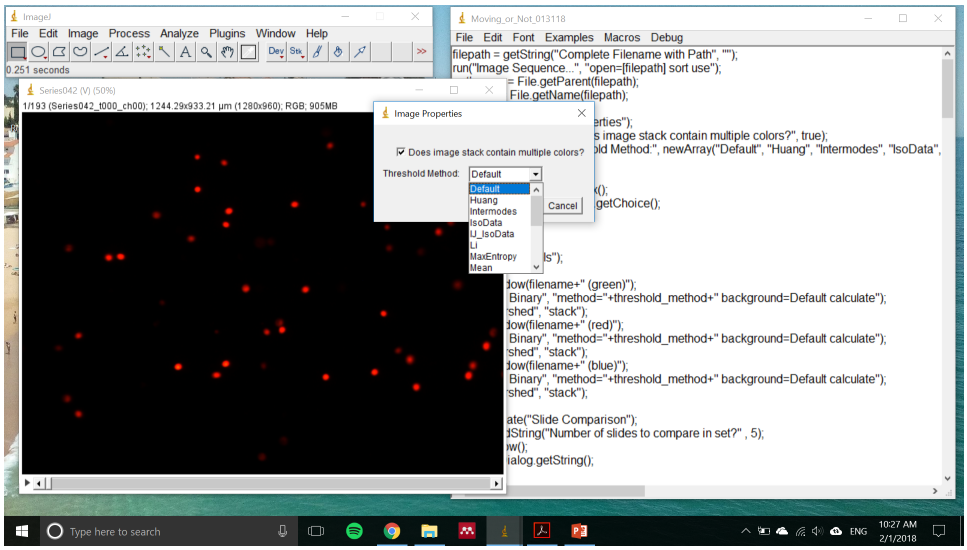

Figure B.3: Threshold method dialog box.

- Choose a threshold method for the stack. This needs to be done by trial and error. Before starting the macro, you can use the threshold command in Image–>Adjust–>Threshold to see different methods.

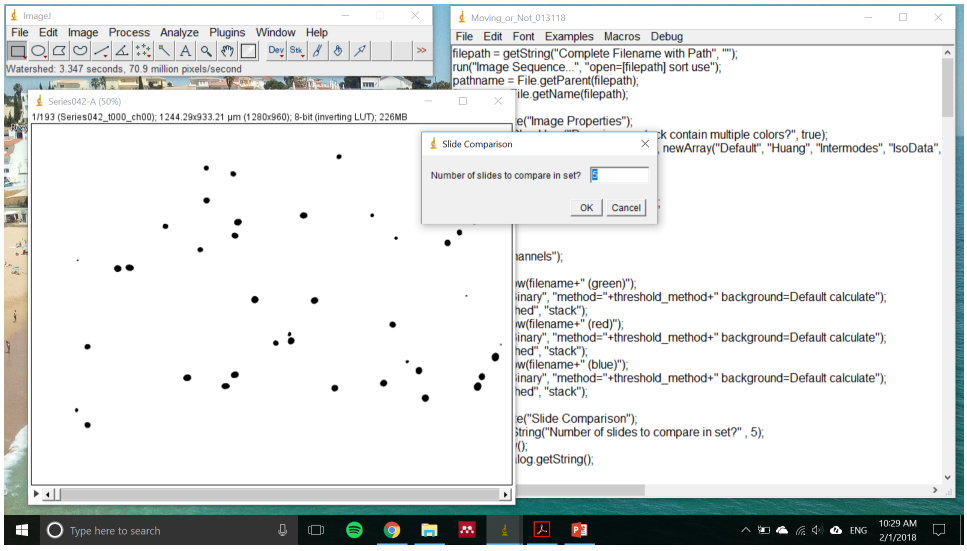

Figure B.4: Median processing dialog box.

- Once the stack has been thresholded, the macro will ask for the number of slides you want to compare. Depending on the speed of items moving and the frame rate of

imaging, this number will need to be optimized. If there is too much noise in the processed image (see figure), raise the number of slides for comparison. If cells or parts of the cell are missing, lower this number. This step takes time. If the stack contains many images, a small subset can be optimized before applying these values to the full stack.

- This process uses the standard analyze particles to count cells and cell radii in each video. The parameters here may need to be modified if the original image stack contained non-cell objects, or if the cells have high eccentricity. At the end of this process, there will be 12 videos for a color image stack, and 4 for a single channel stack: For the red, green, and blue channels, or for the single black and white channel, there will be a video of all cells flowing, a video of stationary cells, a video of counted total cells and a video of counted stationary cells. There will also be a corresponding excel formatted output with data for each of the counted cells. To validate that the parameters for analysis are correct, compare the counted cell videos (containing numbers and masks) with the outputs from the median processing, to ensure that all cells were counted and debris was not counted.

B.3 Examples of Noise from Undersampling

If median number of images chosen is too small, undersampling effects like those seen in Figure B.6 are visible.

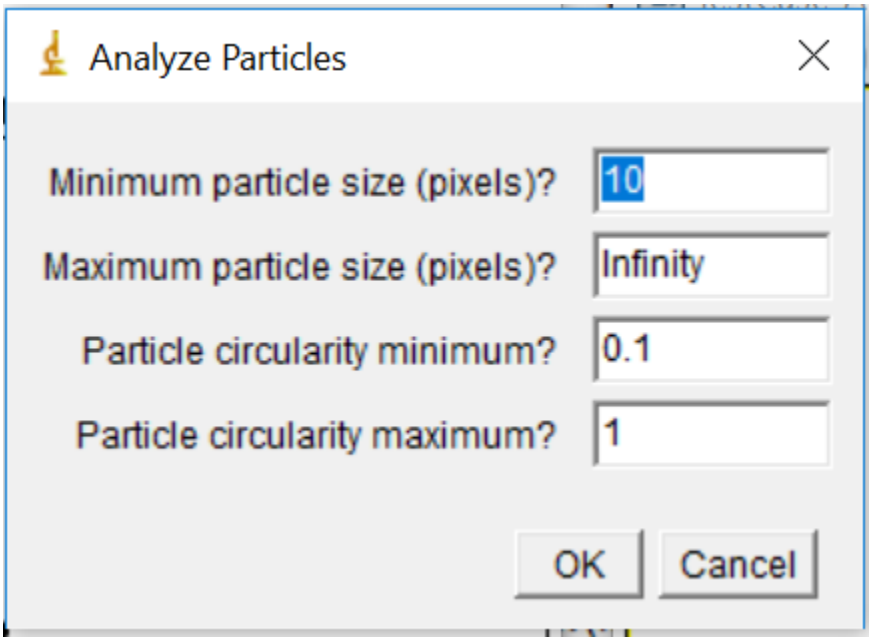

Figure B.5: Analyze particles dialog box.

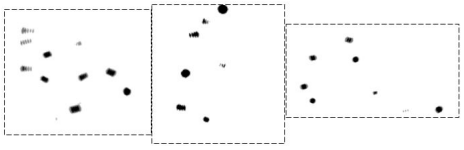

Figure B.6

Opens dialog box to get image stack pathname, imports images.

```
filepath = getString("Complete Filename with Path",
"");
run("Image Sequence...", "open=[filepath] sort
use");
pathname = File.getParent(filepath);
filename = File.getName(filepath);
```

Opens dialog box to ask if the image is multicolor or single color, and asks for the preferred standard image thresholding method.

```
Dialog.create("Image Properties");
Dialog.addCheckbox("Does image stack contain
multiple colors?", true);
Dialog.addChoice("Threshold Method:",
newArray("Default", "Huang", "Intermodes",
"IsoData", "IJ_IsoData", "Li", "MaxEntropy",
"Mean", "MinError", "Minimum", "Moments", "Otsu",
"Percentile", "RenyiEntropy", "Shanbhag",
"Triangle", "Yen"));
Dialog.show();

color = Dialog.getCheckbox();
threshold_method = Dialog.getChoice();
```

If statement: here until "else" is image processing for multicolor images.

Splits channels into red, green, blue.

Thresholds images and watersheds them to separate clumps of cells.

```
if(color)
{
run("Split Channels");

selectWindow(filename+" (green)");
run("Make Binary", "method="+threshold_method+"
background=Default calculate");
run("Watershed", "stack");
selectWindow(filename+" (red)");
run("Make Binary", "method="+threshold_method+"
background=Default calculate");
run("Watershed", "stack");
selectWindow(filename+" (blue)");
run("Make Binary", "method="+threshold_method+"
background=Default calculate");
run("Watershed", "stack");
```

Opens dialog to ask how many consecutive slides to compare.

```
Dialog.create("Slide Comparison");
Dialog.addString("Number of slides to compare in
set?" , 5);
Dialog.show();
number=Dialog.getString();
```

Beginning of median processing. Uses Z-project command to do a median processing, comparing consecutive images.

```
selectWindow(filename+" (green)");
run("Z Project...", "start=1 stop="+number+"
projection=Median");


selectWindow(filename+" (green)");
for (i=1; i<=nSlices-number; i++)
{
nstart=i+1;
```

Figure B.7

A for loop sequentially cycles through the image stack, comparing a set of slides (the number depends on the response in previous dialog box.)

The median processed images (containing stationary cells only) are written to a new file labeled "MED".

This then repeats for each color stack.

```
nstop=i+number;
run("Z Project...", "start="+nstart+ "
stop="+nstop+" projection=Median");
selectWindow("MED_"+filename+" (green)");
run("Add Slice");
selectWindow("MED_"+filename+" (green)-1");
run("Copy");
selectWindow("MED_"+filename+" (green)");
run("Paste");
selectWindow("MED_"+filename+" (green)-1");
close();
selectWindow(filename+" (green)");
}



selectWindow(filename+" (red)");
run("Z Project...", "start=1 stop="+number+"
projection=Median");

selectWindow(filename+" (red)");
for (i=1; i<=nSlices-number; i++)
{
nstart=i+1;
nstop=i+number;
run("Z Project...", "start="+nstart+ "
stop="+nstop+" projection=Median");
selectWindow("MED_"+filename+" (red)");
run("Add Slice");
selectWindow("MED_"+filename+" (red)-1");
run("Copy");
selectWindow("MED_"+filename+" (red)");
run("Paste");
selectWindow("MED_"+filename+" (red)-1");
close();
selectWindow(filename+" (red)");

}

selectWindow(filename+" (blue)");
run("Z Project...", "start=1 stop="+number+"
projection=Median");

selectWindow(filename+" (blue)");
for (i=1; i<=nSlices-number; i++)
{
nstart=i+1;
nstop=i+number;
run("Z Project...", "start="+nstart+ "
stop="+nstop+" projection=Median");
selectWindow("MED_"+filename+" (blue)");
run("Add Slice");
selectWindow("MED_"+filename+" (blue)-1");
run("Copy");
```

Figure B.8

Z-processing continued.	`selectWindow("MED_"+filename+" (blue)");`
	`run("Paste");`
	`selectWindow("MED_"+filename+" (blue)-1");`
	`close();`
	`selectWindow(filename+" (blue)");`
	`}`

Saves new image stacks.	`selectWindow("MED_"+filename+" (red)");`
	`saveAs("Tiff", filepath+"MED (red)");`
	`selectWindow("MED_"+filename+" (green)");`
	`saveAs("Tiff", filepath+"MED (green)");`
	`selectWindow(filename+" (red)");`
	`saveAs("Tiff", filepath+" (red)");`
	`selectWindow(filename+" (green)");`
	`saveAs("Tiff", filepath+" (green)");`
	`selectWindow("MED_"+filename+" (blue)");`
	`saveAs("Tiff", filepath+"MED (blue)");`
	`selectWindow(filename+" (blue)");`
	`saveAs("Tiff", filepath+" (blue)");`

Dialog opens for user to input values for the "Analyze Particles" command.	`Dialog.create("Analyze Particles");`
	`Dialog.addString("Minimum particle size (pixels)?"`
	`, 10);`
	`Dialog.addString("Maximum particle size (pixels)?",`
	`"Infinity");`
	`Dialog.addString("Particle circularity minimum?",`
	`0.10);`
	`Dialog.addString("Particle circularity maximum?",`
	`1.00);`
	`Dialog.show();`
	`min_size=Dialog.getString();`
	`max_size=Dialog.getString();`
	`min_circ=Dialog.getString();`
	`max_circ=Dialog.getString();`

Thresholds images again, counts cells, and outputs a video with counted, numbered cells. Outputs an excel formatted list of cell counts per slide.	`selectWindow(filename+"MED (red).tif");`
	`setAutoThreshold("Default");`
	`//run("Threshold...");`
	`setThreshold(129, 255);`
	`setOption("BlackBackground", false);`
	`run("Convert to Mask", "method=Default`
	`background=Light");`
	`run("Analyze Particles...", "size="+min_size+"-`
	`"+max_size+" circularity="+min_circ+"-"+max_circ+"`
	`show=Outlines clear summarize stack");`
	`selectWindow("Summary of "+filename+"MED`
	`(red).tif");`
	`saveAs("Text", filepath+"Summary of MED`
	`(red).xls");`
	
	`selectWindow(filename+"MED (green).tif");`
	`setAutoThreshold("Default");`
	`//run("Threshold...");`

Figure B.9

Analyzing cells, continued.

```
setThreshold(129, 255);
setOption("BlackBackground", false);
run("Convert to Mask", "method=Default
background=Light");
run("Analyze Particles...", "size="+min_size+"-
"+max_size+" circularity="+min_circ+"-"+max_circ+"
show=Outlines clear summarize stack");
selectWindow("Summary of "+filename+"MED
(green).tif");
saveAs("Text", filepath+"Summary of MED
(green).xls");


selectWindow(filename+"MED (blue).tif");
setAutoThreshold("Default");
//run("Threshold...");
setThreshold(129, 255);
setOption("BlackBackground", false);
run("Convert to Mask", "method=Default
background=Light");
run("Analyze Particles...", "size="+min_size+"-
"+max_size+" circularity="+min_circ+"-"+max_circ+"
show=Outlines clear summarize stack");
selectWindow("Summary of "+filename+"MED
(blue).tif");
saveAs("Text", filepath+"Summary of MED
(blue).xls");


selectWindow(filename+" (red).tif");
run("Analyze Particles...", "size="+min_size+"-
"+max_size+" circularity="+min_circ+"-"+max_circ+"
show=Outlines clear summarize stack");
selectWindow("Summary of "+filename+" (red).tif");
saveAs("Text", filepath+"Summary of (red).xls");


selectWindow(filename+" (green).tif");
run("Analyze Particles...", "size="+min_size+"-
"+max_size+" circularity="+min_circ+"-"+max_circ+"
show=Outlines clear summarize stack");
selectWindow("Summary of "+filename+"
(green).tif");
saveAs("Text", filepath+"Summary of (green).xls");



selectWindow(filename+" (blue).tif");
run("Analyze Particles...", "size="+min_size+"-
"+max_size+" circularity="+min_circ+"-"+max_circ+"
show=Outlines clear summarize stack");
selectWindow("Summary of "+filename+" (blue).tif");
saveAs("Text", filepath+"Summary of (blue).xls");
```

Figure B.10

Repeating the same process for a single-color image stack.

```
}

else{

selectWindow(filename);
run("Duplicate...", "title="+filename+"-A
duplicate");
run("Make Binary", "method="+threshold_method+"
background=Default calculate");
run("Watershed", "stack");

selectWindow(filename);
close();

Dialog.create("Slide Comparison");
Dialog.addString("Number of slides to compare in
set?" , 5);
Dialog.show();
number=Dialog.getString();


selectWindow(filename+"-A");
run("Z Project...", "start=1 stop="+number+"
projection=Median");


selectWindow(filename+"-A");
for (i=1; i<=nSlices-number; i++)
{
nstart=i+1;
nstop=i+number;
run("Z Project...", "start="+nstart+ "
stop="+nstop+" projection=Median");
selectWindow("MED_"+filename+"-A");
run("Add Slice");
selectWindow("MED_"+filename+"-A-1");
run("Copy");
selectWindow("MED_"+filename+"-A");
run("Paste");
selectWindow("MED_"+filename+"-A-1");
close();
selectWindow(filename+"-A");
}



selectWindow("MED_"+filename+"-A");
saveAs("Tiff", filepath+"-A MED");
selectWindow(filename+"-A");
saveAs("Tiff", filepath+"-A");

Dialog.create("Analyze Particles");
```

Figure B.11: Particle analysis dialog box.

Repeating the same process for a single-color image stack.

```
Dialog.addString("Minimum particle size (pixels)?"
, 10);
Dialog.addString("Maximum particle size (pixels)?",
"Infinity");
Dialog.addString("Particle circularity minimum?",
0.10);
Dialog.addString("Particle circularity maximum?",
1.00);
Dialog.show();
min_size=Dialog.getString();
max_size=Dialog.getString();
min_circ=Dialog.getString();
max_circ=Dialog.getString();

selectWindow(filename+"-A MED.tif");
setAutoThreshold("Default");
//run("Threshold...");
setThreshold(129, 255);
setOption("BlackBackground", false);
run("Convert to Mask", "method=Default
background=Light");
run("Analyze Particles...", "size="+min_size+"-
"+max_size+" circularity="+min_circ+"-"+max_circ+"
show=Outlines clear summarize stack");
selectWindow("Summary of "+filename+"-A MED.tif");
saveAs("Text", filepath+"-A Summary of MED.xls");


selectWindow(filename+"-A.tif");
run("Analyze Particles...", "size="+min_size+"-
"+max_size+" circularity="+min_circ+"-"+max_circ+"
show=Outlines clear summarize stack");
selectWindow("Summary of "+filename+"-A.tif");
saveAs("Text", filepath+"-A Summary.xls");


}
```

Figure B.12: Undersampling of median processed images.

B.4 Macro Code with Sections Explained

B.5 Example Outputs

Cell Flow Rate: 1.25 μl/min Video Frame Rate: 30 fps, with 1/5 sampled Input parameters: Multicolor, Otsu Thresholding, 21 slide comparison For Cell Analysis: 10-Infinity pixel cell size, 01-1 cell circularity parameters

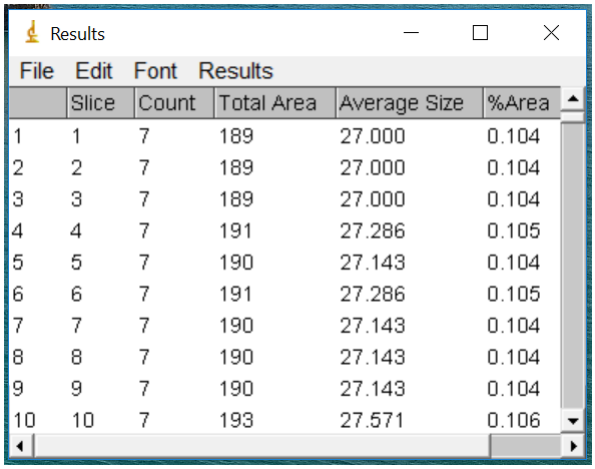

	Slice	Count	Total Area	Average Size	%Area
1	1	7	189	27.000	0.104
2	2	7	189	27.000	0.104
3	3	7	189	27.000	0.104
4	4	7	191	27.286	0.105
5	5	7	190	27.143	0.104
6	6	7	191	27.286	0.105
7	7	7	190	27.143	0.104
8	8	7	190	27.143	0.104
9	9	7	190	27.143	0.104
10	10	7	193	27.571	0.106

Figure B.13: A results list as shown is exported for each of the videos. For each slide it lists the number of cells, the total area taken up by cells, and the average size of the cells.

Screen shots representing videos for each category: see attached files for full video.

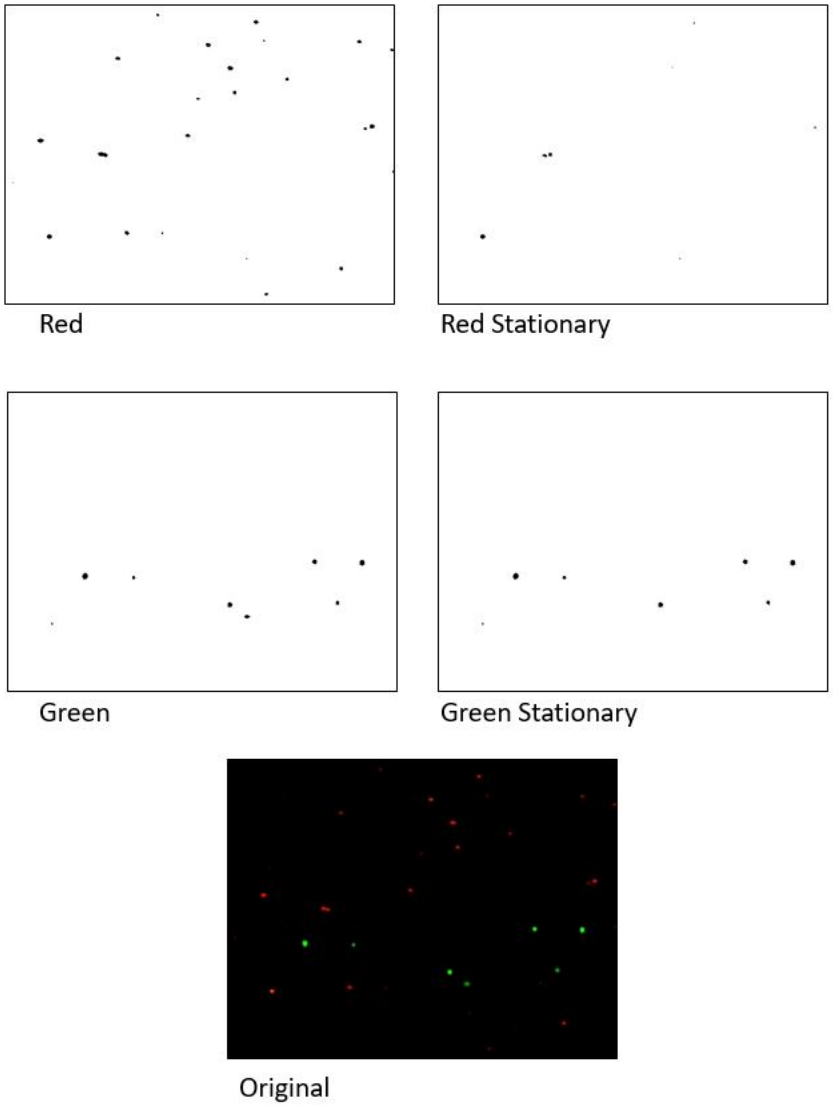

Figure B.14

Appendix C

Matlab Codes for Baseline model for tumor resistance and recurrence

C.1 Deterministic main–2 cell types

```
clear;
clc;

global r1 r2 P1 P2

figure(1)
r1 = .2;
r2 = .1;
P1_treatment = 0.2;
P2_treatment = 0.1;

P1 = 0;
P2 = 0;

[t,x] = ode23(@chemo_ode, [0 100],[0.1;0.1]);
```

```
plot(t,x)
hold on

for i=0:10

P1 = P1_treatment;
P2 = P2_treatment;
a=x(length(x),1);
b=x(length(x),2);

[t,x] = ode23(@chemo_ode, [100+25*i 115+25*i],[a,b]);
plot(t,x)

P1 = 0;
P2 = 0;
a=x(length(x),1);
b=x(length(x),2);

[t,x] = ode23(@chemo_ode, [115+25*i,125+25*i],[a,b]);
plot(t,x)
end

legend('Stromal', 'TIC')

figure(2)
```

```
P1 = 0;
P2 = 0;

[t,x] = ode23(@chemo_ode, [0 100],[0.1;0.1]);
plot(t,x)
hold on

for i=0:10

P1 = P1_treatment;
P2 = P2_treatment;
a=x(length(x),1);
b=x(length(x),2);

[t,x] = ode23(@chemo_ode, [100+10*i 105+10*i],[a,b]);
plot(t,x)

P1 = 0;
P2 = 0;
a=x(length(x),1);
b=x(length(x),2);

[t,x] = ode23(@chemo_ode, [105+10*i,110+10*i],[a,b]);
plot(t,x)
end
```

```
legend('Stromal', 'TIC')

figure(3)



P1 = 0;
P2 = 0;

[t,x] = ode23(@chemo_ode, [0 100],[0.1;0.1]);
plot(t,x)
hold on

for i=0:10

P1 = P1_treatment;
P2 = P2_treatment;
a=x(length(x),1);
b=x(length(x),2);

[t,x] = ode23(@chemo_ode, [100+20*i 120+20*i],[a,b]);
plot(t,x)

end

legend('Stromal', 'TIC')
```

C.2 Deterministic main–3 cell types

```
clear;
clc;

global r1 r2 r3 P1 P2 P3

figure(1)
r1 = .2;
r2 = .1;
r3 = 0.05;
P1_treatment = 0.1;
P2_treatment = 0.04;
P3_treatment = 0.02;

P1 = 0;
P2 = 0;
P3 = 0;

[t,x] = ode23(@chemo_ode_3, [0 100],[0.1;0.1;0.1]);
plot(t,x)
hold on

for i=0:10

P1 = P1_treatment;
```

```
P2 = P2_treatment;

P3 = P3_treatment;

a=x(length(x),1);

b=x(length(x),2);

c=x(length(x),3);


[t,x] = ode23(@chemo_ode_3, [100+25*i 115+25*i],[a,b,c]);

plot(t,x)


P1 = 0;

P2 = 0;

P3 = 0;

a=x(length(x),1);

b=x(length(x),2);

c=x(length(x),3);



[t,x] = ode23(@chemo_ode_3, [115+25*i,125+25*i],[a,b,c]);

plot(t,x)

end


legend('Stromal', 'TIC')


figure(2)


P1 = 0;
```

```
P2 = 0;

P3 = 0;


[t,x] = ode23(@chemo_ode_3, [0 100],[0.1;0.1;0.1]);

plot(t,x)

hold on


for i=0:10


P1 = P1_treatment;

P2 = P2_treatment;

P3 = P3_treatment;

a=x(length(x),1);

b=x(length(x),2);

c=x(length(x),3);



[t,x] = ode23(@chemo_ode_3, [100+10*i 105+10*i],[a,b,c]);

plot(t,x)


P1 = 0;

P2 = 0;

P3 = 0;

a=x(length(x),1);

b=x(length(x),2);

c=x(length(x),3);
```

```
[t,x] = ode23(@chemo_ode_3, [105+10*i,110+10*i],[a,b,c]);
plot(t,x)
end

legend('Stromal', 'TIC')

figure(3)



P1 = 0;
P2 = 0;
P3 = 0;

[t,x] = ode23(@chemo_ode_3, [0 100],[0.1;0.1;0.1]);
plot(t,x)
hold on

for i=0:10

P1 = P1_treatment;
P2 = P2_treatment;
P3 = P3_treatment;
a=x(length(x),1);
b=x(length(x),2);
```

```
c=x(length(x),3);



[t,x] = ode23(@chemo_ode_3, [100+20*i 120+20*i],[a,b,c]);
plot(t,x)

end

legend('Stromal', 'TIC')
```

C.3 Stochastic Main–2 cell types

```
clear;
clc;

global r1 r2 P1 P2
for k=1:10
figure(1)
r1 = .2;
r2 = .1;
P1_treatment = 0.1;
P2_treatment = 0.1;

P1 = 0;
```

```
P2 = 0;

[t,x] = ode23(@chemo_ode, [0 100],[0.1;0.1]);
plot(t,x)
hold on

for i=0:10

P1 = P1_treatment*rand();
P2 = P2_treatment*rand();
a=x(length(x),1);
b=x(length(x),2);

[t,x] = ode23(@chemo_ode, [100+25*i 115+25*i],[a,b]);
plot(t,x)

P1 = 0;
P2 = 0;
a=x(length(x),1);
b=x(length(x),2);

[t,x] = ode23(@chemo_ode, [115+25*i,125+25*i],[a,b]);
plot(t,x)
end

legend('Stromal', 'TIC')
```

```
figure(2)

P1 = 0;
P2 = 0;

[t,x] = ode23(@chemo_ode, [0 100],[0.1;0.1]);
plot(t,x)
hold on

for i=0:10

P1 = P1_treatment*rand();
P2 = P2_treatment*rand();
a=x(length(x),1);
b=x(length(x),2);

[t,x] = ode23(@chemo_ode, [100+10*i 105+10*i],[a,b]);
plot(t,x)

P1 = 0;
P2 = 0;
a=x(length(x),1);
b=x(length(x),2);

[t,x] = ode23(@chemo_ode, [105+10*i,110+10*i],[a,b]);
```

```
plot(t,x)
end

legend('Stromal', 'TIC')

figure(3)



P1 = 0;
P2 = 0;

[t,x] = ode23(@chemo_ode, [0 100],[0.1;0.1]);
plot(t,x)
hold on

for i=0:10

P1 = P1_treatment*rand();
P2 = P2_treatment*rand();
a=x(length(x),1);
b=x(length(x),2);

[t,x] = ode23(@chemo_ode, [100+20*i 120+20*i],[a,b]);
plot(t,x)

end
```

```
legend('Stromal', 'TIC')

end
```

C.4 Chemotherapy ODE for a 2-state deterministic or stochastic system with no evolution or spatial dependence

Filename: $chemo_ode.m$

```
function dx = chemo_ode(t,x)

global r1 r2 P1 P2;

dx = zeros(2,1);
dx(1) = r1*x(1)*(1-x(1)-x(2))-P1*x(1);
dx(2) = r2*x(2)*(1-x(1)-x(2))-P2*x(2);
```

C.5 Chemotherapy ODE for a 3-state deterministic or stochastic system with no evolution or spatial dependence

Filename: $chemo_ode_3.m$

```
function dx = chemo_ode_3(t,x)


global r1 r2 r3 P1 P2 P3


dx = zeros(3,1);
dx(1) = r1*x(1)*(1-x(1)-x(2)-x(3))-P1*x(1);
dx(2) = r2*x(2)*(1-x(1)-x(2)-x(3))-P2*x(2);
dx(3) = r3*x(3)*(1-x(1)-x(2)-x(3))-P3*x(3);
```